5-4-2021

The Role of Plasma Membrane ATPase Pumps in the Regulation of Rhythmic Activity in Electrically Excitable Cells

Parker J. Ellingson
Georgia State University

The Role of Plasma Membrane ATPase Pumps in the Regulation of Rhythmic Activity in Electrically Excitable Cells

by

Parker J. Ellingson

Under the Direction of Gennady Cymbalyuk, PhD, and Ronald Calabrese, PhD

A Dissertation Submitted in Partial Fulfillment of the Requirements for the Degree of

Doctor of Philosophy

in the College of Arts and Sciences

Georgia State University

2021

ABSTRACT

Membrane bound ion pumps have long been studied in a housekeeping role, and it is well known that they play a major part in creating the ionic gradients which determine the electrical excitability in a cell. Recent work has begun to highlight other, more direct roles for ion pumps in rhythm generation and information processing. As many pumps obtain energy for active ion transport from adenosine triphosphate (ATP) hydrolysis, they can exchange ions in an electrically asymmetric manner, generating an outward current, which along with ion channel currents, drives the membrane potential of the cell. Membrane potential is a major determining characteristic for how information is transferred between neurons, and so in persistently active excitable cells, pumps can provide a considerable contribution to neuron dynamics. Specialized networks of neurons and non-neural cells which drive rhythmic behaviors such as breathing and locomotion, must robustly produce useful patterns for the animal under dynamic behavioral goals in a highly variable environment. Here we will focus on two well-studied classes of ATPase pumps (the plasma membrane calcium ATPase pump (PMCA) and the sodium-potassium ATPase pump (Na^+/K^+ pump)) and investigate the role of these pumps in two rhythm generating biological subsystems with a combination of modeling and experimental approaches. In a model of a leech heartbeat central pattern generator, we demonstrate how the neuromodulator myomodulin can regulate the temporal properties of rhythm generation through effects on the hyperpolarization-activated current and the Na^+/K^+ pump current, and discuss the benefits of modulators which target multiple currents. With this model, we also show how synaptic inhibition can support a functional pattern when pump current is downregulated. Then, in a model of interstitial cells of Cajal (ICC) in the muscular syncytium of the intestinal walls, we demonstrate that due to the importance of complex intracellular calcium oscillations in the

generation of ICC rhythms, the PMCA pump can play a major role in regulating the temporal properties of rhythm generation. We discuss rhythm generation mechanisms in both systems and predict parameter domains of multistability which correspond to both functional and pathological states of rhythm generation.

INDEX WORDS: Central pattern generator, Oscillators, Dynamical systems, Neuromodulation, Multistability, Gastrointestinal motility, Heartbeat, Computational neuroscience, Invertebrate, Vertebrate, Electrophysiology

The Role of Plasma Membrane ATPase Pumps in the Regulation of Rhythmic Activity in Electrically Excitable Cells

by

Parker Ellingson

Committee Chair: Gennady Cymbalyuk

Committee: Ronald Calabrese

Vadym Apalkov

Vladimir Bondarenko

Chun Jiang

Electronic Version Approved:

Office of Graduate Services

College of Arts and Sciences

Georgia State University

May 2021

DEDICATION

This dissertation is dedicated to my family and friends. They have all contributed to my academic journey, but several people merit special mention. Mom and Dad, who taught me to shoot for the stars and helped an 8-year-old bookworm with his homemade dinosaur encyclopedia. Grandad, who introduced me to the world of engineering and inspired me with the adventure and love he has created in his life. My cousin Walter, who taught me chess and challenged me to never stop learning about the world and its people. Finally, my wife Hend, my starlight who has been there at every step holding me up and keeping me focused on the future.

ACKNOWLEDGEMENTS

I would like to acknowledge and thank many people who have supported me and contributed to this effort. My advisor, Gennady Cymbalyuk, whose patience and guidance helped me achieve what I have. Ronald Calabrese for his invaluable advice as I formulated papers. The members of my committee, who take time from their schedules to evaluate and hone my project. The members of the Cymbalyuk lab, both past and present, who have been colleagues, sounding boards, advisors, and friends - especially Jessica Parker, Will Barnett, Taylor Kahl, Alex Vargas, Ricardo Erazo-Toscano, Akira Sakurai, and collaborators Natalia Maksymchuk and Sergiy Korogod. Bryce Chung for his guidance and friendship when I was a fresh graduate student. Don Edwards, who helped me begin to bridge the gap between thinking as an engineer and thinking as a scientist. Ryan Sleeth for helping me manage our computational resources. The GSU Neuroscience faculty members who instructed and mentored me, especially Dan Cox and Chuck Derby, who helped guide me through the process in their roles as directors of graduate studies in the Neuroscience Institute. Emily Hardy and Liz Weaver for their amazing support of Neuroscience programs at GSU. The Neuroscience Graduate Student Association at GSU, which provides both social and professional support. Finally, Michael Black, Manfred Schmidt, and Joe Normandin who taught me how to teach. An immense thank you to everyone who has supported my academic efforts.

TABLE OF CONTENTS

LIST OF TABLES

LIST OF FIGURES

LIST OF ABBREVIATIONS

Abbreviation	Definition
CPG	Central Pattern Generator
HN	Leech Heart Interneuron
HCO	Half Center Oscillator
ATP	Adenosine triphosphate
PMCA	Plasma membrane calcium ATPase
ICC	Interstitial cells of Cajal
ER	Endoplasmic Reticulum
PU	Pacemaker Unit (here referring to ICCs)

1 INTRODUCTION

There are a number of critical functions performed by animals which rely on the production and maintenance of rhythmic patterns. Breathing, locomotion, digestion, and circulation all require robust rhythm generation and regulation to ensure the survival of an organism. Networks of rhythm generating neurons known as central pattern generators (CPGs) drive these functions. In a chaotic, highly variable environment like the one we inhabit, behavioral goals are constantly in flux, and the neurons of a CPG must maintain or modify their functions accordingly. This can be accomplished through feedback from sensory systems or central modulation of the CPG circuits.

However, processes which modulate or coregulate membrane currents can push electrically excitable cells near the limits of the dynamical characteristics which allow them to produce functional activity. Modulation must be carefully managed (Harris-Warrick & Johnson 2010). Even small changes to the biophysical properties of a cell can result in dynamical states such as silence or multistability (Malashchenko et al. 2011, Barnett et al. 2013, Ellingson et al. 2019). Multistability is a phenomenon in which a dynamical system is capable of producing distinctly different patterns given the same parameters due the presence of multiple attractors, and it has been identified in a variety of neuronal systems (Marin et al. 2013, Barnes et al. 1997, Newman & Butera 2010). While some multistable regimes are functional, others lurk below the surface in the dynamics and represent pathological states if they are realized.

To study the effects of modulation, we can represent neurons and neural networks as dynamical systems and use these biophysical models to simulate neural behavior under varying conditions. Biophysical models are approached reductively, in that one must have an understanding of the physical principles of the smaller pieces of the physical system first. These pieces can then be

incorporated into a set of differential equations, and the entire model can be studied as a dynamical system. Models are ultimately hypotheses about the way a system works. We combine elements of our basic understanding and test whether that understanding is capable of capturing complex behaviors observed in real systems with many interacting subsytems. Models can serve as a check on hypotheses about the functioning of smaller components and also predict the effects of perturbations to a real system.

In the modeling of electrically excitable cells such as neurons, the physical subsystems of interest typically include ion channels and metabolic process. Ion channels are transmembrane proteins which can open or close to allow or facilitate the exchange of ions across the membrane directly depending on factors such as membrane potential or chemical ligand binding. Common ion channels in neurons include those permeable to Na^+, K^+, Ca^{2+} or Cl^-, with all playing a role in the generation of action potentials. Single channel recordings suggest that ion channel opening and closing is a stochastic process, so in whole cell biophysical models, channel activation states are often modeled with Boltzmann or Hill functions. Another important class of transmembrane proteins are the ATPase ion pumps. Rather than being activated by chemical ligands or membrane voltage, these pumps utilize the energy from ATP hydrolysis to actively transport ions across the membrane.

In this dissertation I will present modeling and experimental work performed in two different bioelectrical pattern generating systems, and highlight roles played by two types of ATPase pumps in generating, maintaining, and regulating those patterns.

1.1 ATPase Pumps

Ion pumps have long been studied in a housekeeping role, and it is well known that they play a major part in regulating the ionic gradients which determine the electrical excitability in a

cell. By pumping ions against their electrochemical gradient, these pumps stabilize the resting membrane potential and regulate cell volume through osmolarity. Recent work has begun to highlight other, more direct roles for ion pumps. As these pumps obtain energy for active transport from ATP, they can exchange ions in an electrically asymmetric manner, generating a membrane current, which along with ion channel currents, drives the membrane potential of the cell. Membrane potential is a major determining characteristic which determines how information is transferred between neurons, and so in sensitive excitable cells, pumps can be major contributors to neuron dynamics. Even for pumps where ion transport is electrically equitable, the change they create in ionic gradients can have effects on the driving force of currents carrying those ions, the reversal potential, or metabolic functions. Here we will focus on two well-studied classes of membrane bound ATPase pumps: the plasma membrane calcium ATPase pump (PMCA) and the sodium-potassium ATPase pump (Na^+/K^+ pump). The PMCA pump is a protein which utilizes energy from the hydrolysis of ATP to move calcium ions from the cytosol across the cell membrane into the extracellular space. It works slowly, but has a high binding affinity for calcium, making it well suited for a slow but consistent extrusion of intraceulluar calcium, even at low concentrations. The Na^+/K^+ pump is a crucial piece of many cellular systems. It utilizes the energy from ATP to move K^+ into the cell while moving Na^+ out of the cell at a ratio of two K^+ ions to three Na^+ ions. This helps to stabilize a cell's resting membrane potential, regulate cell volume through osmolarity, and serves a particularly important role in neurons by "winding up" the ionic gradients for explosive Na^+ entry during an action potential. The housekeeping roles for these pumps have been well established, but some studies emphasize that these pumps can also be modulated and even play a role in information processing (Tobin & Calabrese 2005, Forrest 2014).

1.2 Interstitial Cells of Cajal in the Mammalian Small Intestinal Syncytium

In the mammalian intestine, motor patterns are paced by a network of interstitial cells of Cajal (ICCs) which are electrically coupled one another and to the smooth muscle cell in a large excitable syncytium. First described by Santiago Ramon y Cajal, they are the source of the electrical slow waves which propagate through the intestinal wall and drive smooth muscle contraction. Two types of interstitial cells of Cajal are recognized in the small intestine: the myenteric (ICC-MY) and deep muscle plexus (ICC-DMP). Both have been shown to undergo internal calcium oscillations, but those in ICC-DMP occurs at a lower frequency and ICC-DMP are incapable of producing slow wave activity independently (Sanders *et al.* 2006). Studies in the 1980s detailed that the source of electrical slow waves was a plane within the intestinal walls, and that removal of cells from this area completely eliminated slow waves (Sanders *et al.* 2006). Double electrode recordings confirmed by optical experiments with fluorescent calcium dyes showed that the smooth muscle coupled to the interstitial cells of Cajal displayed slow waves later than the interstitial cell itself (Kito *et al.* 2003, Hennig *et al.* 2004). Later it was shown that neutralizing receptor tyrosine kinase Kit resulted in gastric emptying disorders, and loss-of-function mutations in the dominant white spotting (*W*) locus upon which Kit is encoded resulted in a failure to develop interstitial cells of Cajal and also completely eliminated slow waves. *W* mutant mice also displayed irregularities in synchronization and coordination of motor activity in the small intestine (Der-Silaphet *et al.* 1998).

It is important to understand the specific mechanisms by which these pacemaking cells produce their patterns, and most in the field agree that intracellular calcium oscillations in microdomains of interstitial cells of Cajal are the pacing events, and that calcium activated currents are then responsible for whole cell depolarization. The current understanding for the

basis of the pacemaking potential is internal calcium oscillations between the Endoplasmic Reticulum (ER) and microdomains of cytosol between the cell membrane and the ER. There is some debate over the mechanisms of the pacemaker current. It is known that inositol 1,4,5-triphosphate receptors (and the ongoing presence of IP3) is required for slow wave generation (Ward *et al.* 2003). Similarly, it has been shown that ryanodine receptors play a role along with IP3Rs in an initial release of calcium from ER stores into the cytosolic microdomain (Aoyama *et al.* 2004). A stochastic release of calcium through these channels activates a spontaneous inward current. The source of this current has been debated, but recently it has also been shown that anoctamin 1 (Ano1) calcium activated chloride channels are necessary for the generation of slow waves (Malysz *et al.* 2017), making it a likely candidate for the microdomain pacemaker potential. T-Type calcium channels were shown to be involved in the upstroke of the slow wave. It seems likely that the Ano 1 channels are initiating the slow wave, and that T-type calcium channels are activating as a response to the local depolarization. The resultant influx of calcium coordinates the activation of Ano1 and T-Type calcium channels in other microdomains, creating a summed effect which underpins the electrical slow wave. The Sodium-Potassium-Chloride Cotransporter (Na+-K+-Cl- Cotransporter or NKCC) has been shown to be necessary for maintaining normal slow wave activity, suggesting that it is the primary mechanism by which the chloride gradient is recovered (Zhu *et al.* 2016). The fact that intracellular calcium plays such a large role in the generation of the rhythm is a suggestion that calcium pumps and exchangers may play a critical role in the actual rhythm generation. Using a well-established model of ICC pace-making (Corrias & Buist 2008) we investigate the role of the PMCA pump in rhythm generation.

1.3 The Leech Heartbeat Central Pattern Generator

In the leech species *Hirudo verbena (spp)*, the two tubular leech hearts are controlled by a central pattern generator neural subsystem, which is driven by mutually inhibitory pairs of heart interneurons (HN cells) in the 3rd and 4th segmental ganglia of the nerve cord. HN cells are capable of producing a pattern of alternating bursting activity which is then organized into patterns for controlling the heartbeat by the rest of the CPG. Even when isolated from the rest of the intersegmental CPG, HNs robustly produce their alternating activity. This structure of two cells which mutually inhibit one another is a ubiquitous network structure call a half-center oscillator (HCO). HN cells are large, and readily identifiable in experiments, and the electrical activity and circuitry of this CPG is well studied. There is a solid base of knowledge on the excitatory properties of ion channels present in the cells and the production and measuring of the alternating bursting rhythm they produce (Calabrese et al. 1995, Wenning et al. 2018). Here we investigate the effects of the neuropeptide myomodulin on the rhythm by building a model of the HN cell and applying insights from earlier experiments with myomodulin to demonstrate the mechanism of action. We compare predictions from the model to new experiments with myomodulin and find good agreement.

1.4 Approach

In this dissertation we investigate the roles that the PMCA and Na^+/K^+ pumps play in rhythm generation in excitable cells. First, we present a dynamical model of leech heart interneurons. This style of model has been under development for nearly 30 years, and has been instrumental in discovering insights into the functioning of the leech heartbeat CPG, and led to insights into the mechanics of bursting in CPGs (Nadim et al. 1996, Hill et al. 2001, Olypher et al. 2006, Kueh et al. 2016). We then use this model to investigate a mechanism of

neuromodulation involving the Na^+/K^+ pump by the endogenous neuropeptide myomodulin by varying biophysical parameters identified in a previous study (Tobin & Calabrese 2005). We use an experimental approach to investigate the dose-response of HN HCOs to myomodulin and discuss the implications of the mechanism of modulation. We then look for the presence of coexistent regimes in the parameter space associated with myomodulin in both single cell models and HCO models of HN cells and discuss the protective nature of the HCO structure in this system. Finally, we use a well established dynamical model of mammalian ICCs to investigate a role that the PMCA pump could play in regulating rhythm generation by varying the maximal flux during model simulations. We discuss how the complex calcium concentration oscillations in intracellular compartments required to generate the electrical activity of the cells enhance the role of the calcium pump, and search for regions of multistability near the canonical set of parameters which could represent dysfunctional regimes of activity.

2 THE HN MODEL

This section presents the biophysical model of pacemaking leech heart interneurons in the 3rd and 4th segmental ganglia which was developed to investigate the effects of myomodulin and the interplay between the pump and other sodium carrying currents.

2.1 Model

For this investigation, we optimized a single-compartment Hodgkin-Huxley style (Hodgkin & Huxley 1952) model of a single leech heart interneuron and a half-center oscillator from *Kueh et al.* (2016). The HCO is comprised of two identical neurons mutually inhibiting each other, as is schematically shown in Figure 3.1. Simulated HN cells contained a Na^+/K^+ pump current (I_{Pump}) governed by intracellular sodium concentration $[Na^+]_i$, a leak current (I_{Leak}), and eight voltage-gated currents: fast Na^+ (I_{NaF}), persistent Na^+ (I_P), fast low-voltage activated Ca^{2+} (I_{CaF}), low-voltage activated slowly inactivating Ca^{2+} (I_{CaS}), hyperpolarization-activated (h-) current (I_h), slowly inactivating delayed-rectifier K^+ (I_{K1}), persistent K^+ (I_{K2}) and fast A-type K^+ currents (I_{KA}). The leak current and h-current each have two components: one carrying Na^+, $I_{Leak,Na}$ and $I_{h,Na}$, and one carrying K^+ , $I_{Leak,K}$ *and* $I_{h,K}$. This allowed us to track $[Na]_i$ fluxes per current and to use $[Na]_I$ in the computation of Na^+ reversal potential. The current conservation equation governing membrane potential in the HCO model was:

$$C_m \frac{dV}{dt} = -\big(I_{NaF} + I_P + I_{Leak,Na} + I_{h,Na} + I_{CaF} + I_{CaS} + I_{K1} + I_{K2} + I_{KA} + I_{Leak,K} + I_{h,K} + I_{Pump} + I_{syn}\big) \quad \textit{Eq. 1}$$

where individual currents were computed in a conductance-based manner:

$$I_x = \bar{g}_x {m_x}^{a_x} {h_x}^{b_x} (V - E_x) \quad \textit{Eq. 2}$$

$$\frac{dm_x}{dt} = \frac{m_{x_\infty}(V) - m}{\tau_{m_x}(V)} \quad \textit{Eq. 3}$$

$$\frac{dh_x}{dt} = \frac{h_{x_\infty}(V) - h}{\tau_{h_x}(V)} \quad \textit{Eq. 4}$$

where $\bar{g}_x$ is the maximal conductance of x -current, $x \in \{NaF, P, CaF, CaS, h, K1, K2, KA\}$, and E_x is its reversal potential. The state variables ${m_x}^{a_x}$ and ${h_x}^{b_x}$ are the current's activation and inactivation voltage-gating variables, respectively, $m_{x_\infty}(V)$ and $h_{x_\infty}(V)$ are its steady state functions of the membrane potential V, and $\tau_{m_x}(V)$ and $\tau_{h_x}(V)$ are its time constant functions. Current parameters and equations for time constants and steady state activation and inactivation functions are available in Tables 2.2, 2.3, and 2.4.

Leak current and h-current (which are carried by both Na^+ and K^+) were separated into Na^+ and K^+ components so that Na^+ components could be used in the dynamic calculation of intracellular Na^+ concentration:

$$I_{h,Na} = \frac{3}{7}\bar{g}_h {m_h}^2 \, (V - E_{Na}) \quad \textit{Eq. 5}$$

$$I_{h,K} = \frac{4}{7}\bar{g}_h {m_h}^2 \, (V - E_K) \quad \textit{Eq. 6}$$

$$I_{Leak,Na} = g_{Leak,Na} \, (V - E_{Na}) \quad \textit{Eq. 7}$$

$$I_{Leak,K} = g_{Leak,K}(V - E_K) \quad \textit{Eq. 8}$$

Components of the leak conductance were determined in terms of the conventional equivalent leak conductance and leak reversal potential, referred to as reference values, into two separate specific Na^+ and K^+ leak currents so that:

$$I_{Leak} = g_{Leak}\left(V - E_{Leak,Ref}\right) = I_{Leak,Na} + I_{Leak,K} \quad \textit{Eq. 9}$$

The resulting partial conductances are:

$$\bar{g}_{Leak,Na} = g_{Leak}\frac{E_{Leak,Ref} - E_K}{E_{Na,Ref} - E_K} \quad \textit{Eq. 10}$$

$$\bar{g}_{Leak,K} = g_{Leak}\frac{E_{Leak,Ref} - E_{Na,Ref}}{E_K - E_{Na,Ref}} \quad \textit{Eq. 11}$$

The $E_{Na,Ref}$ was fixed at 0.045V, and these partial conductances were fixed prior to simulation and were kept the same for the whole study.

Intracellular Na^+ concentration $[Na^+]_i$ is computed dynamically as a function of the Na^+ fluxes generated by two Na^+ currents, Na^+ components of leak and h-current, and the Na^+/K^+ pump:

$$\frac{d[Na]_i}{dt} = -\frac{I_{NaF} + I_P + I_{h,Na} + I_{Leak,Na} + 3I_{Pump}}{v\,F} \quad \textit{Eq. 12}$$

$[Na^+]_i$ also determines the Na^+ reversal potential:

$$E_{Na} = \frac{RT}{F}\ln\left(\frac{[Na]_o}{[Na]_i}\right) \quad \textit{Eq. 13}$$

Above, F is Faraday's constant, R is the gas constant, T is the temperature in Kelvin, v is the volume of the intracellular Na^+ compartment, and $[Na]_o$ is the extracellular Na^+ concentration.

Pump current is governed by the intracellular Na^+ concentration $[Na]_i$:

$$I_{Pump} = \frac{I_{PumpMax}}{1 + exp\left(\frac{[Na]_{ih} - [Na]_i}{[Na]_{is}}\right)} \quad \textit{Eq. 14}$$

where $[Na]_{ih}$ is $[Na]_i$ of half activation of the pump and $[Na]_{is}$ is the pump sensitivity to $[Na]_i$.

Synaptic chloride currents have spike dependent and graded components:

$$I_{syn} = I_{SynS} + I_{SynG} \quad \textit{Eq. 15}$$

$$I_{SynS} = \bar{g}_{SynS} Y_{Pre} M_{Pre} \left(V - E_{Syn}\right) \quad \textit{Eq. 16}$$

$$I_{SynG} = \bar{g}_{SynG} \frac{{P_{Pre}}^3}{C + {P_{Pre}}^3} \left(V - E_{Syn}\right) \quad \textit{Eq. 17}$$

where $C = 10^{-32}$ C^3 and $E_{Syn} = -0.0625\ V$.

Spike-dependent synapse activation was computed as:

$$\frac{dY}{dt} = \frac{X - Y}{0.011} \quad \textit{Eq. 18}$$

$$\frac{dX}{dt} = \frac{X_\infty(V) - X}{0.002} \quad \textit{Eq. 19}$$

$$\frac{dM}{dt} = \frac{M_\infty(V) - M}{0.2} \quad \textit{Eq. 20}$$

$$X_\infty(V) = \frac{1}{1 + \exp\left(-1000(V + 0.01)\right)} \quad \textit{Eq. 21}$$

$$M_{\infty}(V) = 0.1 + \frac{0.9}{1 + \exp(-1000(V + 0.04))} \quad \textit{Eq. 22}$$

Graded synaptic activation was computed using a proxy of presynaptic Ca^{2+} concentration in the following manner:

$$\frac{dP}{dt} = I_{Ca} - BP \quad \textit{Eq. 23}$$

where B is a Ca^{2+} buffering rate constant ($B = 10\ s^{-1}$), and I_{Ca} is computed as follows:

$$I_{Ca} = \max(0, -I_{CaF} - I_{CaS} - A) \quad \textit{Eq. 24}$$

$$\frac{dA}{dt} = \frac{A_{\infty}(V) - A}{0.2} \quad \textit{Eq. 25}$$

$$A_{\infty}(V) = \frac{10^{-10}}{1 + exp\big(-100(V + 0.02)\big)} \quad \textit{Eq. 26}$$

Single cell models utilized the same equations, but without I_{Syn} or synaptic activation variables X, Y, M, P, or A. Model parameters and activation equations are available in (S1).

Differential equations describing the model dynamics were integrated using the Embedded Runge-Kutta Prince-Dormand (8,9) method from the GNU Scientific Library version 2.6 (https://www.gnu.org/software/gsl/). The absolute tolerance was set to 10^{-9}, the relative tolerance was set to 10^{-10}, and maximal time step used was 10^{-3} seconds. Models were implemented in C and compiled with the GNU Compiler Collection version 7.5.0 (https://gcc.gnu.org/). The system was simulated for 1600, and the last 300 seconds were used in analysis to confine the focus to the steady state.

Table 2.1. Table of Standard Initial Conditions

Table of initial conditions for the 40-dimensional HN HCO model. During a sweep, each time a new $\bar{g}_h$ value was tested, initial conditions were set as below. Synaptic state variables here are associated with the synaptic activation of one cell, which then influences the synaptic current of the other cell.

Initial Conditions

	State variable	Value
HN(R)	V (R)	-0.0439010843326 V
	m_{CaF} (R)	0.832170050413
	$_{hCaF}$ (R)	0.11381461314
	m_{CaS} (R)	0.702467473405
	h_{CaS} (R)	0.0989876197983
	m_{K1} (R)	0.0314799867472
	h_{K1} (R)	0.813835318456
	m_{K2} (R)	0.139801573601
	m_{KA} (R)	0.458312610323
	h_{KA} (R)	0.0595503659331
	m_h (R)	0.209165343138
	m_{NaP} (R)	0.575560640304
	m_{Na} (R)	0.0964705869558
	h_{Na} (R)	0.99926484696
	$[Na]_I$ (R)	0.0144131004575 M
	P (R)	3.50188415805e-28
	A (R)	2.14427767443e-12
	X (R)	2.99560987191e-21
	Y (R)	9.20014577621e-05
	M (R)	0.274748227718
HN(L)	V (L)	-0.0579704036577 V
	m_{CaF} (L)	0.00371569674585
	$_{hCaF}$ (L)	0.913128722596
	m_{CaS} (L)	0.0160816041811
	h_{CaS} (L)	0.372599649498
	m_{K1} (L)	0.00499726624515
	h_{K1} (L)	0.966843208674
	m_{K2} (L)	0.0329782686355
	m_{KA} (L)	0.138649501286
	h_{KA} (L)	0.314591116607
	m_h (L)	0.691473916028
	m_{NaP} (L)	0.219699253189
	m_{Na} (L)	0.0127982024647
	h_{Na} (L)	0.999999170748
	$[Na]_I$ (L)	0.0140476677491 M
	P (L)	2.29525269429e-11
	A (L)	1.21395086902e-11
	X (L)	6.16601453418e-37
	Y (L)	5.71268466328e-37
	M (L)	0.1000000127

Table 2.2. Model Cell Constants and Parameters

Table of cell constants and current parameters conductance $\bar{g}_x$(nS), activation exponential a_x, inactivation exponential b_x, and reversal potential E_x (V). (*) values are for control conditions.

Cell Constants				
C_m	0.5 nF			
vol	0.0034 nL			
T	289.46 K			
$[Na]_o$	0.115 M			
Current Parameters				
Current	$\bar{g}_x$(nS)	a_x	b_x	E_x (V)
I_h	1.6*	2	0	
I_{NaP}	10.5	1	0	Ena
I_{Na}	200	3	1	Ena
I_{CaF}	5	2	1	0.135
I_{CaS}	3.2	2	1	0.135
K_1	100	2	1	-0.07
K_2	40	2	0	-0.07
K_A	80	2	1	-0.07
I_{SynS}	150	-	-	-0.0625
I_{SynG}	30	-	-	-0.0625

Table 2.3. Model Cell Parameters for Special Currents

Table of parameters for special currents I_{Leak} and I_{Pump}. (*) values are for control conditions.

Special Current Parameters			
	$\bar{g}_{Leak}$ (nS)	$E_{Na,Ref}$ (V)	$E_{Leak,Ref}$ (V)
I_{Leak}	9	0.045	-0.06
	$I_{PumpMax}$(nA)	$[Na]_{is}$ (M)	$[Na]_{ih}$ (M)
I_{Pump}	0.429*	0.0004	0.018

Table 2.4. Steady State Activations and Time Constant Equations

Table of equations used for calculating the steady state activation $m_{x_\infty}(V)$ and inactivation $h_{x_\infty}(V)$, and time constants of activation $\tau_{m_x}(V)\ (s)$and inactivation $\tau_{h_x}(V)\ (s)$.

Current Steady State Activation and Time Constant

Current	$m_{x_\infty}(V)$	$\tau_{m_x}(V)\ (s)$	$h_{x_\infty}(V)$	$\tau_{h_x}(V)\ (s)$
I_h	$\frac{1}{1+2e^{(180(V+0.045))}+e^{(500(V+0.045))}}$	$0.7+\frac{1.7}{1+e^{(-100(V+0.073))}}$	-	-
I_{NaP}	$\frac{1}{1+e^{(-120(V+0.039))}}$	$0.01+\frac{0.2}{e^{(400(V+0.057))}}$	-	-
I_{Na}	$\frac{1}{1+e^{(-150(V+0.029))}}$	0.0001	$\frac{1}{1+e^{(500(V+0.03))}}$	$0.004+\frac{0.006}{1+e^{(500(V+0.028))}}$
I_{CaF}	$\frac{1}{1+e^{(-600(V+0.0467))}}$	$0.011+\frac{0.024}{\cosh(-330(V+0.0467))}$	$\frac{1}{1+e^{(350(V+0.0555))}}$	$0.06+\frac{0.31}{1+e^{(270(V+0.055))}}$
I_{CaS}	$\frac{1}{1+e^{(-420(V+0.0472))}}$	$0.005+\frac{0.134}{1+e^{(-400(V+0.0487))}}$	$\frac{1}{1+e^{(360(V+0.055))}}$	$0.2+\frac{5.25}{1+e^{(-250(V+0.043))}}$
K_1	$\frac{1}{1+e^{(-143(V+0.021))}}$	$0.001+\frac{0.011}{1+e^{(150(V+0.016))}}$	$\frac{1}{1+e^{(111(V+0.028))}}$	$0.5+\frac{0.2}{1+e^{(-143(V+0.013))}}$
K_2	$\frac{1}{1+e^{(-83(V+0.022))}}$	$0.057+\frac{0.043}{1+e^{(200(V+0.035))}}$	-	-
K_A	$\frac{1}{1+e^{(-130(V+0.044))}}$	$0.005+\frac{0.011}{1+e^{(200(V+0.03))}}$	$\frac{1}{1+e^{(160(V+0.063))}}$	$0.026+\frac{0.0085}{1+e^{(-300(V+0.055))}}$

3 COMODULATION OF H- AND NA/K PUMP CURRENTS IN THE LEECH HEARTBEAT CENTRAL PATTERN GENERATOR

3.1 Abstract

Central pattern generators (CPGs), specialized oscillatory neuronal networks controlling rhythmic motor behaviors such as breathing and locomotion, must adjust their patterns of activity to a variable environment and changing behavioral goals. Neuromodulation adjusts these patterns by orchestrating changes in multiple ionic currents. In the medicinal leech, the endogenous neuromodulator myomodulin speeds up the heartbeat CPG by reducing the electrogenic Na^+/K^+ pump current and increasing h-current in pairs of mutually inhibitory leech heart interneurons (HNs)which form half-center oscillators (HN HCOs). Here we investigate whether the comodulation of two currents could have advantages over a single current in the control of functional bursting patterns of a CPG. We use a conductance-based biophysical model of an HN HCO to explain the experimental effects of myomodulin. We demonstrate that in the model, comodulation of the Na^+/K^+ pump current and h-current expands the range of functional bursting activity by avoiding transitions into nonfunctional regimes such as asymmetric bursting and plateau-containing seizure-like activity. We validate the model by finding parameters that reproduce temporal bursting characteristics matching experimental recordings from HN HCOs under control, three different myomodulin concentrations, and Cs^+ treated conditions. The matching cases are located along the border of an asymmetric regime away from the border with more dangerous seizure-like activity. We found a simple comodulation mechanism with an inverse relation between the pump and h-currents makes a good fit of the matching cases and comprises a general mechanism for the robust and flexible control of oscillatory neuronal networks.

3.2 Significance Statement

Rhythm generating neuronal circuits adjust their oscillatory patterns to accommodate a changing environment through neuromodulation. In different species, chemical messengers participating in such processes may target two or more membrane currents. In medicinal leeches, the neuromodulator myomodulin speeds up the heartbeat central pattern generator (CPG) by reducing Na^+/K^+ pump current and increasing h-current. In a computational model, we show that this comodulation expands the range of CPG's functional activity by navigating the circuit between dysfunctional regimes resulting in a much wider range of cycle period. This control would not be attainable by modulating only one current, emphasizing the synergy of combined effects. Given the prevalence of h-current and Na^+/K^+ pump current in neurons, similar comodulation mechanisms may exist across species.

3.3 Introduction

To achieve behavioral flexibility necessary for survival in a variable environment, neuronal circuits must produce, control, and scale functional activity over a broad range of underlying biophysical properties (Marder & Calabrese 1996, Calabrese 1998, Doi & Ramirez 2008, Marder 2012). Central pattern generators (CPGs) and other rhythmic neuronal circuits are continuously adjusted through neuromodulation, which is orchestrated by changes in multiple ionic currents including the electrogenic Na^+/K^+ pump (Marder & Calabrese 1996, Doi & Ramirez 2008, Grashow et al 2010, Harris-Warrick 2011, Marder 2012, Marder et al. 2014, Sharples & Whelan 2017). Yet we are only beginning to understand how the phenomenal robustness of neurons and networks is attained given the wide range of functional burst properties produced by modulation (Grashow et al. 2009, Tang et al. 2012, Marder et al. 2015, Dashevskiy & Cymbalyuk 2018, Parker et al. 2018). Because neuromodulators or cocktails of neuromodulators may have multiple

cellular targets, it is often difficult to determine the combined effects of modulation by sampling effects of single factor variation such as dose-response experiments. For example, some modulators like dopamine or serotonin commonly have opposing effects (Seamans et al. 2001, Teshiba et al. 2001, Sharples & Whelan 2017). Opposing effects may be distinguished by timescales and dose-dependence producing unique transient and steady-state effects (Spitzer et al. 2008, Harris-Warrick et al. 1998, Brezina 2003) and may enhance flexibility through state dependence or protect against overmodulation by incorporating negative feedback control mechanisms (Harris-Warrick & Johnson 2010). In contrast, effects of the endogenous neuromodulator myomodulin on the leech heartbeat CPG are caused by changes in two membrane currents with superficially similar effects; it decreases burst period by increasing h-current (I_h) and decreasing Na^+/K^+ pump current (I_{Pump}) (Tobin & Calabrese 2005). How modulators coordinate these effects on activity patterns is poorly understood. Evaluating the advantages offered by the comodulation of two currents with similar effects and the special role of I_{Pump} in modulation requires comprehensive accounting using accurate biophysical modeling.

I_{Pump} is a unique modulation target (Bertorello & Aperia 1990, Bertorello et al. 1990, Catarsi & Brunelli 1991, Scuri et al. 2007, Hazelwood et al. 2008, Zhang & Sillar 2012, Zhang et al. 2012, Zhang et al. 2013, Zhang et al. 2015). While maintaining the proper gradients of Na^+ and K^+ concentrations across the membrane, it produces an outward current with activation kinetics which do not depend on the membrane potential but instead are governed by the internal Na^+ concentration ($[Na^+]_i$). Thus, I_{Pump} can play an important role in the bursting activity (Li et al. 1996, Frohlich et al. 2006, Arganda et al. 2007, Pulver & Griffith 2010, Barreto & Cressman 2011, Krishnan & Bazhenov 2011, Yu et al. 2012, Jasinski et al. 2013). I_{Pump} naturally interacts

with I_h: it is most active during depolarized phase due to raised $[Na^+]_i$ and remains active during the hyperpolarized phase, where I_{Pump} is opposed by I_h (Forrest et al. 2012, Zhang et al. 2017).

The interaction of I_{Pump} and I_h plays a prominent role in the leech heartbeat CPG. This CPG encompasses two half-center oscillators (HN HCOs): pairs of mutually inhibitory HN interneurons producing alternating bursting activity. I_{Pump} and I_h interactions were revealed using the H^+/Na^+ antiporter monensin, which stimulates I_{Pump} by increasing $[Na^+]_i$ (Kueh et al. 2016). In the presence of I_h, application of monensin dramatically decreases the burst duration (BD) and interburst interval (IBI). If I_h is blocked, then monensin decreases BD but lengthens IBI. This experiment demonstrates how each phase of bursting, BD and IBI, is independently affected by I_{Pump} depending on its interaction with I_h. The speedup of the HN HCO burst period by myomodulin (Tobin & Calabrese 2005) by increasing I_h and decreasing I_{Pump} in HNs, suggests coordinated participation of I_{Pump} and I_h and demonstrates their importance as a joint modulatory target controlling burst characteristics.

Here we investigated how comodulation of I_{Pump} and I_h contributes to flexible control of functional bursting activity.

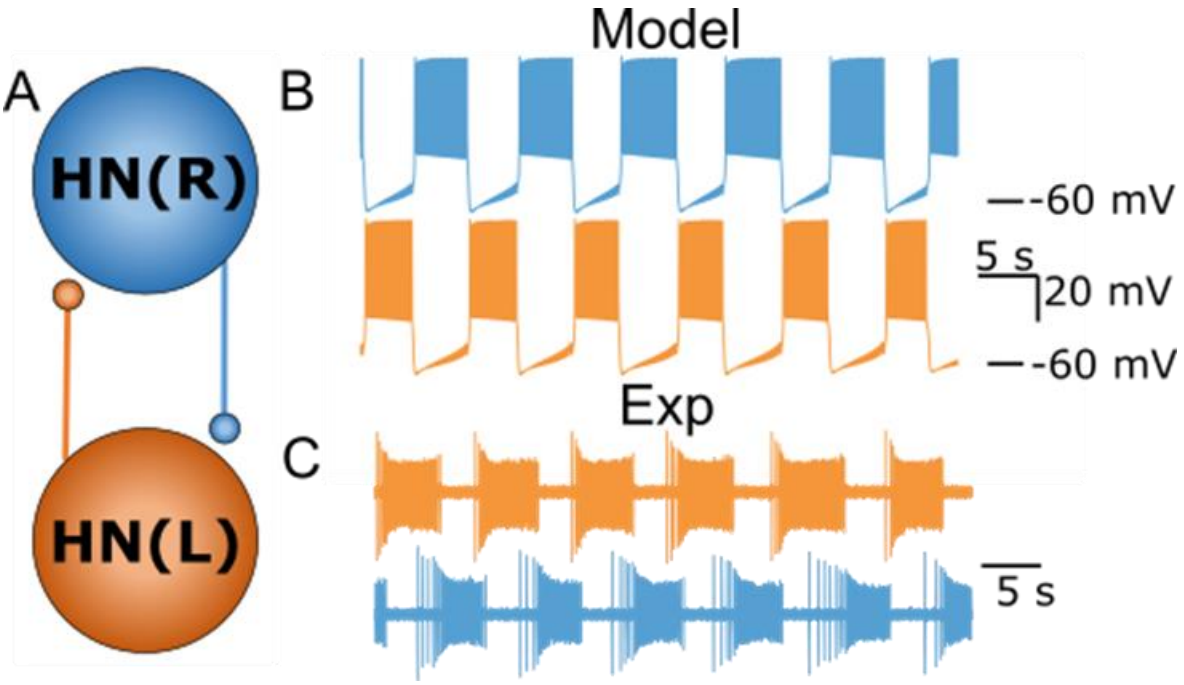

Figure 3.1. HN HCO Model Schematic and Activity
Leech heartbeat Half-Center Oscillator (HN HCO) produces bursting activity alternating between two heart interneurons (HNs). (A) Schematic representation of the Half-Center Oscillator which is comprised of two neurons located on the left and right sides of a ganglion. Two neurons (large circles) have mutually inhibitory synaptic connections (small circles). Model neurons and synaptic connections are identical. Neurons exhibit bursting activity of membrane potentials (B) which reproduces temporal properties of an extracellular recording of the living heartbeat HCO under control conditions (C).

3.4 Methods

3.4.1 Parameter Sweeps

We characterized and mapped activity regimes of the model under variation of two parameters, the maximal h-current conductance ($\bar{g}_h$) and the maximal Na^+/K^+ pump current ($I_{PumpMax}$). For this, we fix $\bar{g}_h$ to a certain value in the range starting with 0 nS, and sweep $I_{PumpMax}$ values, starting from 0.5 nA and decreasing it by a step value of 0.001 nA each next simulation until a value of 0.3 nA was reached. Initial conditions for each simulation for a given $\bar{g}_h$ along decreasing $I_{PumpMax}$ were taken from the end of the previous simulation at the previous value of $I_{PumpMax}$. Then we incremented $\bar{g}_h$ by a step value of 0.2 nS and fixed $\bar{g}_h$ for the next sweep of $I_{PumpMax}$. For each new value of $\bar{g}_h$, a standard set of initial conditions was used (Table

2.1). This procedure was repeated until all parameter values with the aforementioned step sizes were taken for [0 10] nS and [0.3 0.5] nA ranges for $\bar{g}_h$ and $I_{PumpMax}$, respectively. At each parameter pair, the system was simulated for 1600 seconds. The first 1300 seconds containing the transient part of the trace were removed, and only the last 300 seconds were used in the analysis to characterize the steady state activity.

3.4.2 Analysis of Temporal Characteristics of Model Activity Regimes

Analysis of the activity of the model HCO was conducted using custom scripts developed in the MATLAB software (The MathWorks, Inc.). In our parameter sweeps, we observed a variety of different types of activity, which we generally classified as one type of functional activity (functional bursting), or two types of dysfunctional activities: asymmetric bursting, and a plateau-containing activity. We defined functional bursting as symmetrical activity in which cells alternate in generating bursts of spikes; during the burst, cell's membrane potential would rise above -45 mV, and continuously spike until its membrane potential dropped below -45 mV. Asymmetric bursting activity was defined as a similar activity, but with alternating bursts in which bursts of one cell were noticeably longer than those of the other cell. Finally, plateau-containing activity was characterized by the appearance of plateau events in the HCO's activity. We defined plateau-containing activity as an oscillatory activity in which at least one cell in the HCO exhibited at least one depolarized interval in which the cell's membrane potential would rise above -45 mV but spiking within such interval failed. At some parameter domains, plateau activity could be periodic and consist purely of alternating plateau events, while at other domains, activity could be a mixture of plateau events with conventional bursts.

For automated detection and analysis of the three activity regimes defined above, we specify two terms. The depolarized phase of activity of a neuron is the time interval in which

membrane potential rose above -45 mV and remained there for at least 0.5 seconds. Correspondingly, the hyperpolarized phase of the activity was the interval in which membrane potential was below -45 mV. The duration of these phases provides a measure of the envelope of bursting in functional and asymmetrical regimes and also allows us to uniformly measure the temporal characteristics of plateau events using the same method of analysis.

We define a burst event as a continuous spiking interval during a depolarized phase of activity. Spike times were identified as moments of time at which the peaks in the voltage trace were above a threshold of -30 mV. Spike times were then used to distinguish bursts from plateaus. Spikes which had no predecessor or occurred at least 0.4 seconds after their predecessor were marked as the beginning of a spike-train. Then, the end of the spike-train was determined by spikes which had no successive spikes for at least 0.4 seconds. If multiple spike-trains were detected within a single depolarized phase or if the end of the depolarized phase did not have a preceding spike within 0.4 seconds, that depolarized phase would be tagged as a plateau event. A depolarized phase, which contained a single uninterrupted spike-train from the beginning to the end of the depolarized interval, was then tagged as a burst event. In depolarized phases which were classified as bursts, burst duration was computed as the time between first and last spike detected, burst period was computed as the time between the first spike in a burst and the first spike in the next burst, and interburst interval was computed as the time between the last spike in a burst and the first spike in the next burst. In cases where the depolarized phase was defined as a burst, the depolarized phase duration was nearly identical (± one interspike interval) to burst duration, making this a good metric for describing the temporal pattern of either bursts or plateaus.

We define a measure of asymmetry between the depolarized phases of each side (HN(R) and HN(L)) of the HCO using the following expression:

$$Asymm = \frac{2\left|\overline{UD}_{HN,R} - \overline{UD}_{HN,L}\right|}{\overline{UD}_{HN,R} + \overline{UD}_{HN,L}} \quad \textit{Eq. 27}$$

where $\overline{UD}_{HN,R}$ and $\overline{UD}_{HN,L}$ are the mean depolarized phase durations of model cells HN(R) and HN(L), respectively. Asymmetric bursting regimes were defined as those bursting regimes which did not exhibit any plateau events and for which the asymmetry measure was higher than 0.2. This threshold measure is represented by a case in which the burst duration of one model neuron is at least 55% of the period and the burst duration of the other model neuron is at most 45% of the period. Correspondingly, a bursting regime which did not contain any plateau events, had an asymmetry measure less than 0.2, and had cycle period within the current and previous experimental ranges (Tobin & Calabrese 2005, Kueh et al. 2016, Wenning et al. 2018) were labeled as functional.

In summary, using the above definitions of the burst and plateau events, regimes of electrical activity were labeled as either (1) functional, (2) asymmetric, or (3) plateau-containing. Plateau-containing regimes were defined as those in which at least one of the depolarized phases was identified as a plateau event as described above. Asymmetric bursting regimes were defined as those bursting regimes which did not exhibit any plateau events and for which the asymmetry measure was higher than 0.2. This threshold measure is represented by a case in which the burst duration of one model neuron is at 55% of the period and the burst duration of the other model neuron is 45% of the period. The asymmetry measure computed for the entire parameter domain is included in Figure 3.3C. Correspondingly, a bursting regime, which did not contain any plateau events and had an asymmetry measure less than 0.2, were labeled as functional.

3.4.3 Dimensions of the Area Supporting Functional Bursting

We investigated the functional regime along each of the $\bar{g}_h$ and $I_{PumpMax}$ axes. The *n* x *m* (51x201) sweep of parameter space was divided into continuous 1 x *m* and 1 x *n* slices in which each slice represents the variation of either $\bar{g}_h$ or $I_{PumpMax}$ while the other is held constant. At each slice, the boundaries of the functional regime were identified, and their difference was calculated as the local range. Then, for each axis, the maximal possible parameter range retaining functional activity was determined. Burst durations, burst periods, and interburst intervals at and within these boundaries were also investigated, and their maximal possible ranges were determined. These maximal ranges were then compared to the maximal range achievable through comodulation, where the axis of comodulation was an inverse function fitted to all parameter pairs in the functional regime (see Curve Fitting).

3.4.4 Experimental Design and Statistical Analysis

We conducted two sets of experiments, each with a within-subjects (repeated-measures) design, whereby we would determine the dose-dependent effects of myomodulin with and without 2 mM Cs^+ (h-current blocker) applied. Each set of experiments was conducted with 5 medicinal leeches, *Hirudo spp.,* using the electrophysiological protocol outlined below. For both experiments, we analyzed the mean burst period, coefficient of variation of burst period, and mean burst duration of the HN(3,4) neurons using one-way repeated-measures ANOVAs with treatment as the independent variable. Post-hoc pairwise comparisons were then conducted using Tukey's Honest Significant Difference test to determine which of the treatment conditions were significantly different from control or Cs^+ alone and whether there was a dose effect between treatments in each experiment. All burst statistics for experiments are reported with the grand

mean and standard error of the mean. A p-value < 0.05 was regarded as statistically significant for all statistical tests.

3.4.5 Electrophysiology

Experimental protocols were similar to those described in Kueh et al. (2016). After surgically isolating the mid-body ganglion 3 or 4 of the nerve cord of medicinal leeches, (n=5) and removing the perineurium, extracellular suction electrodes were used to record from left and right HN(3,4) neurons. After allowing the preparation to settle, control recordings were taken. Subsequently, three concentrations of myomodulin (1 μM, 10 μM, and 100 μM) were applied with a 10-minute wash-out between each application. Each application lasted between 5 and 10 minutes, and short recordings (containing 10-14 bursting cycles) were taken at each concentration once the preparation settled into a regular rhythm. We also performed a second set of experiments on a separate group of animals (n=5) in which Cs^+ (2mM) was used as an h-current blocker. The preferred vertebrate h-current blocker, ZD 7288, does not block leech h-current (multiple unpublished observations). In this set of experiments, ganglia were prepared in the same manner and the same protocol was used, but before the addition of each myomodulin dose, Cs^+ was applied for 5-10 minutes. When analyzing experimental data, burst period was computed as the time between median spikes of adjacent bursts, burst duration was computed as the time between the first and last spike of each burst, and interburst interval was computed as the time between the last spike of a burst and the first spike of the subsequent burst.

3.4.6 Mapping of Experimental Data

For each case from a set of experimental conditions {control, Cs^+, 1 μM myomodulin, 10 μM myomodulin, 100 μM myomodulin}, we determined the parameter pair from within the boundaries of the functional regime which best produced model activity matching the averages

of the burst period and the burst duration of the experimental case. For this, we introduced a simple measure of distance between the model and experimental bursting activity $Dist(\bar{g}_h, I_{PumpMax})$:

$$Dist(\bar{g}_h, I_{PumpMax}) = \sqrt[2]{\left(\overline{BP}_{HN} - \overline{BP}_{Exp}\right)^2 + \left(\overline{BD}_{HN,R} - \overline{BD}_{Exp}\right)^2} \quad \textit{Eq. 28}$$

where $\overline{BP}_{HN}$ *and* $\overline{BD}_{HN,R}$ are the average burst period of both cells and the average burst duration of the R cell in the HCO model at a given parameter set, respectively, and $\overline{BP}_{Exp}$ and $\overline{BD}_{Exp}$ are the corresponding average values from the experimental condition. We performed a search of model parameters that minimize $Dist(\bar{g}_h, I_{PumpMax})$ to be used as representatives of each experimental condition.

Once a parameter pair was selected for the Cs^+ condition, we restricted the choice of parameter pairs for the Cs^+ with myomodulin conditions {Cs^+ + 1 μM myomodulin, Cs^+ + 10 μM myomodulin, Cs^+ + 100 μM myomodulin} to the same value of $\bar{g}_h$ chosen for the Cs^+ only condition.

3.4.7 Curve Fitting

Curve fitting of $(\bar{g}_h, I_{PumpMax})$ parameter pairs was accomplished using the MATLAB fit() function from the Curve Fitting Toolbox. A custom inverse function prototype was defined using the fittype() function as:

$$I_{PumpMax}(\bar{g}_h) = c_1 + \frac{c_2}{(\bar{g}_h - c_3)} \quad \textit{Eq. 29}$$

Initial values for the constants [c_1, c_2, c_3] = [0.47, 0.2, -0.1].

3.5 Results

Myomodulin decreases the burst period in leech heartbeat HCOs by increasing h-current and reducing Na^+/K^+ pump current (Tobin & Calabrese 2005). Here, we investigated advantages that such comodulation might provide by considering a model of a leech heartbeat HCO (Figure 1). The living HN HCOs exhibits alternating, symmetric bursting with a period of 6-9 seconds. During bursting, the membrane potentials oscillate between -65 mV at the lowest point between bursts, -40 mV baseline potential during a burst, and up to 10 mV at the peaks of action potentials during the burst. I_h and persistent Na^+ current, I_P, drive the cell towards a certain membrane potential where the two low-threshold Ca^{2+} currents, I_{CaS} and I_{CaF}, activate and initiate a burst. Then, I_P and I_{CaS} support the burst. I_{Pump} is always outward, has no reversal potential, and $[Na]_i$ determines its magnitude. I_{Pump} and I_P interact throughout the burst and between bursts (Figure 3.2).

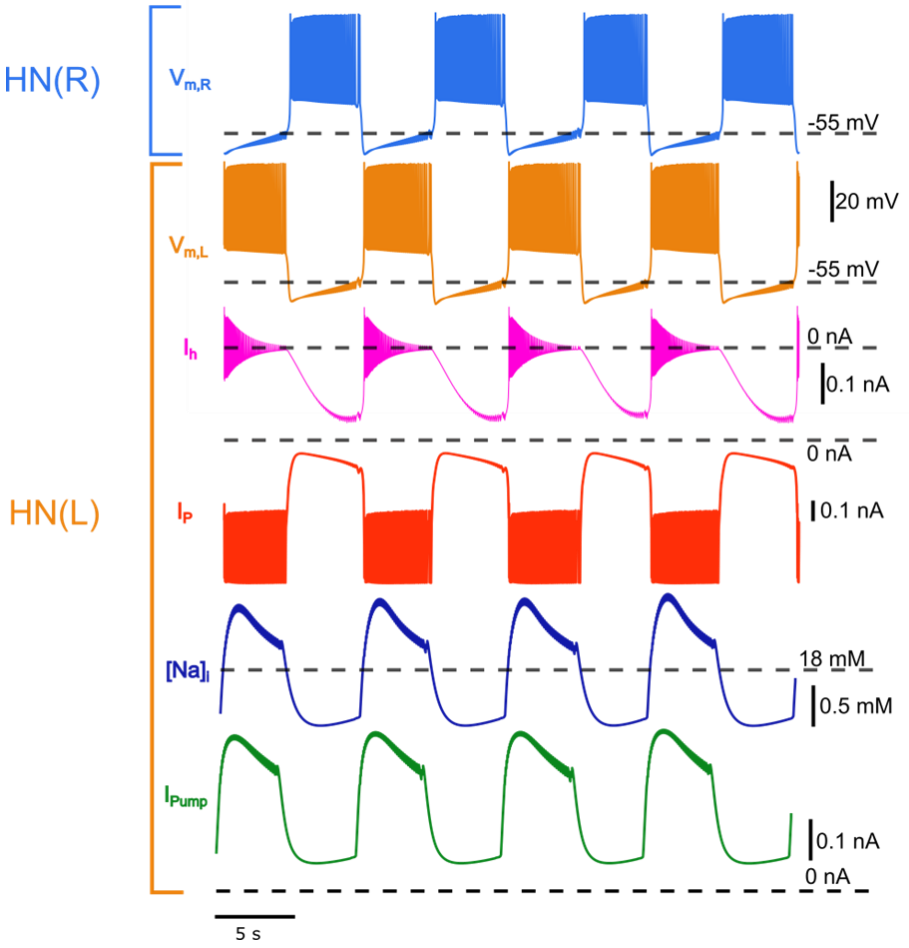

Figure 3.2 HN HCO Model Activity

Half-Center Oscillator model activity of HN(R) and HN(L) cells represented by membrane potentials, select currents, and intracellular sodium concentration. The cells burst in antiphase ($V_{m,R}$ and $V_{m,L}$) mutually inhibiting one another. Between bursts, h-current (I_h), which is activated by hyperpolarization, and persistent sodium current (I_P), which is deactivated but still notable, work together to promote the transition to the depolarized spiking phase of bursting. The pump current (I_{Pump}) contributes to hyperpolarization and is most active during bursts, where it opposes I_P. It is also quite active during the hyperpolarized phase of bursting where it opposes I_h and I_P. The bursts are sustained by activated I_P. I_P is a major contributor to intracellular sodium concentration ($[Na]_i$) during both phases of bursting. The pump current (I_{Pump}) rises quickly with $[Na]_i$ during the spiking phase of bursting and follows $[Na]_i$ between bursts.

3.5.1 Two-Parameter Map Reveals Several Regimes of Activity

To investigate the effects of comodulation of h- and pump currents, we explored model HCO activity in a large domain of two parameters, $\bar{g}_h$ and $I_{PumpMax}$ (Methods). A two-dimensional parameter sweep revealed a strong influence of these currents on the model activity (Figure 3.3). We found that average period of both cells generally decreased as $\bar{g}_h$ was increased (Figure 3.3A). Coefficient of variation of cycle period was generally low (Figure 3.3B), but at

low levels of $I_{PumpMax}$, there were some domains of higher variability. The entire tested parameter space supported oscillatory activity which had periods ranging between 5 and 12 seconds. However, not all observed activity regimes were functional. We classified them into three major categories: functional bursting, asymmetric bursting, and plateau-containing regimes (Materials and Methods) and mapped them along with color coded temporal characteristics.

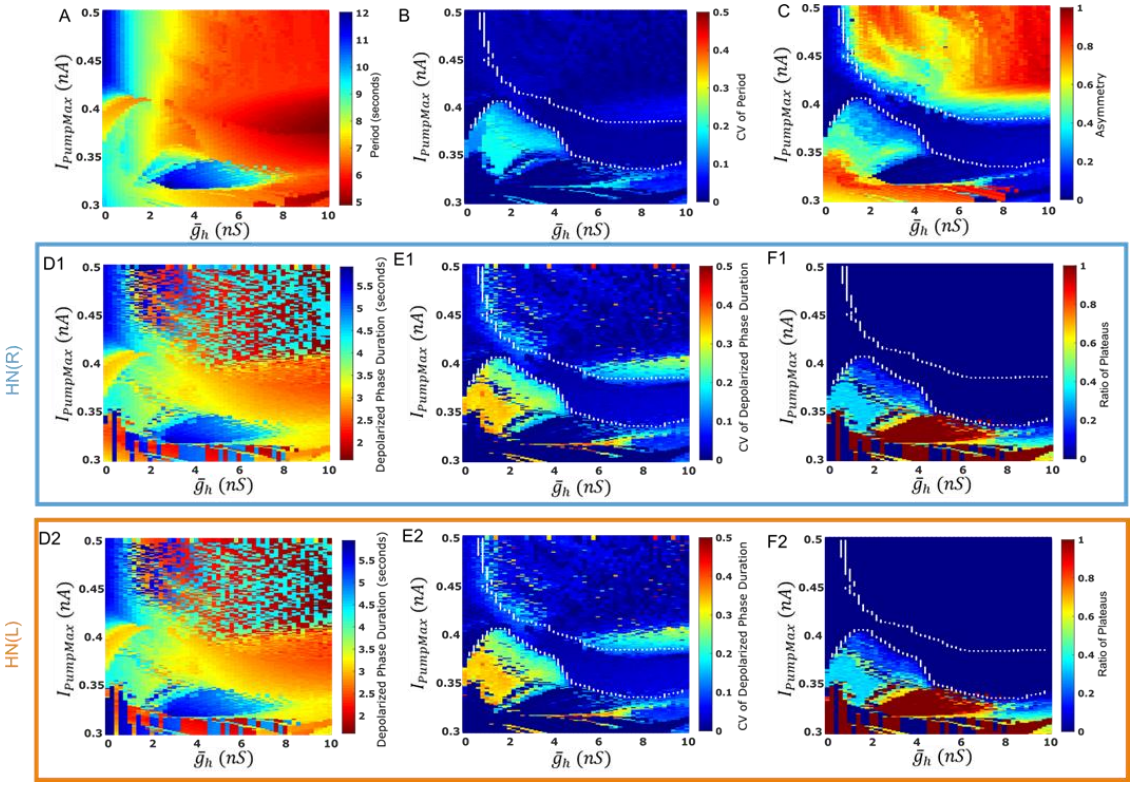

Figure 3.3 HN HCO Parameter Maps of Burst Characteristics

Two parameter maps of HCO model activity characteristics obtained under variation of parameters $\bar{g}_h$ and $I_{PumpMax}$. (A) Average period of both cells from the HCO model. HCO period ranges from 5 seconds to 12 seconds where warmer colors represent shorter periods. The general trend suggests that $\bar{g}_h$ is an effective parameter for controlling period of activity. (B) Coefficient of variation of cycle period, where warmer colors indicate higher variability. C) A measure of the asymmetry of depolarized phase durations between the two cells in HCO. More asymmetric activity is marked by warmer colors in this plot. Asymmetric activity appeared in conditions where $\bar{g}_h$ and $I_{PumpMax}$ were either both high or both low. (D) Average duration of the depolarized phase of HN(R) activity (D1) and HN(L) activity (D2). Warmer colors represent shorter depolarized phase durations. Distinct complementary "checkerboard" patterns appear in these maps for larger values of both $\bar{g}_h$ and $I_{PumpMax}$ indicating asymmetry and, thus, bistability. Coefficient of variation of depolarized phase duration in HN(R) model activity (E1) and HN(L) model activity (E2). (F) Ratio of depolarized phases in model cell HN(R) activity (F1) and HN(L) activity (F2) at a given parameter set which were classified as plateau-like rather than functional bursts. Warmer colors represent traces with more plateau-containing depolarized phases. In B, C, E and F, the white dashed lines indicate the borders of the functional regime.

Comparison of the depolarized phase duration of each cell in the model HCO revealed a "checkerboard" asymmetric pattern at higher values of $\bar{g}_h$ and $I_{PumpMax}$ (Figure 3.3D1 & 3.3D2). In this region, cycle period changes smoothly under variation of the parameters, but the steady state burst durations of the cells are notably different and their proportions in the period flip back and forth between longer and shorter from point to point on the map. Since in our model HCO, both neurons and their connections are identical, it follows that either cell could be the one with longer period. An asymmetric bursting regime with longer burst duration of one cell must be accompanied by another coexisting regime in which the other cell has a longer burst duration. The apparent randomness of the dominating side on the map, visualized as complementary checkerboards in depolarized phase duration, is likely a result of high sensitivity of the asymmetric regimes to the choice of the initial states of the neurons. We had attempted to trace regimes during a sweep; each time we tested a new pair of parameters we set the initial conditions to those of the last time point from the previous simulation. This last point belonged to the steady state bursting activity attained from the previous simulation, which is slightly different from the steady state which the HCO with the new parameter set will produce and thus the trace is slightly perturbed versus the old steady state bursting activity. This difference in initial states explains the presence of both steady-state asymmetric regimes in our data. On the map, (Figure 3.3C) asymmetry measures (Methods) ranged from 0 to 1.85, though 80% of evaluated cases throughout the entire map were less than 1. At higher values of $\bar{g}_h$ and $I_{PumpMax}$, asymmetry was pronounced. In order to operationally label regimes as asymmetric, we chose a conservative asymmetry threshold of 0.2; this represented the case in which the duration of the depolarized phase of one cell in the HCO was equal or larger than 55% of the period. In the model, the period was always equal to the sum of the two burst durations of both HCO neurons.

Although, we considered asymmetric regimes as dysfunctional, we suggest that under relatively low measures of asymmetry the bursting asymmetric regime would present only a mild risk for animal viability.

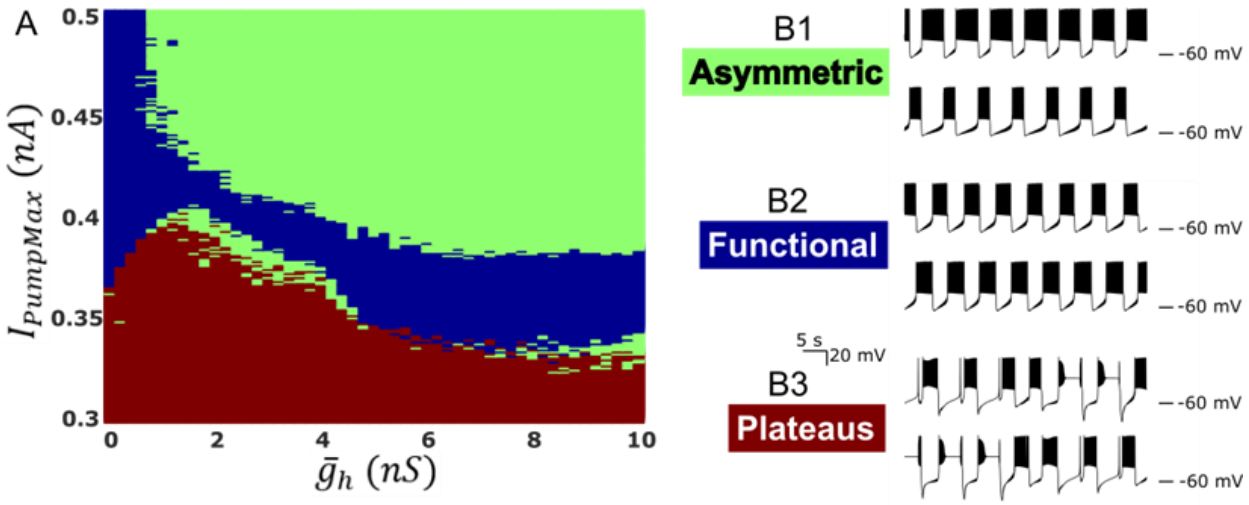

Figure 3.4 HN HCO Regimes of Activity
Functional and non-functional regimes mapped under variation of parameters $\bar{g}_h$ and $I_{PumpMax}$ (A) and representative examples of each regime (B). (A) The regimes have been categorized as asymmetric bursting (green), functional bursting (blue), or plateau-containing activity (red). (B) Examples of membrane potential traces representing the asymmetric regime (B1) at $\bar{g}_h = 3.6$ nS, $I_{PumpMaz} = 0.46$ nA, the functional regime (B2) at $\bar{g}_h = 3.6$ nS, $I_{PumpMaz} = 0.4$ nA, and the plateau-containing regime (B3) at $\bar{g}_h = 3.6$ nS, $I_{PumpMaz} = 0.36$ nA. This map unveils a functional pathway through parameter space.

Another dysfunctional activity regime was noted by inspection of the coefficient of variation of the cycle period of model activity, which detected an area of high period variability at low values of $I_{PumpMax}$. Further investigation of patterns in this area on the map revealed a large domain supporting complex activity consisting of plateau events, single spikes, and bursts. While the exact patterns varied widely, they all exhibited depolarized plateau events in one or both cells' activity. Plateaus in this system *in vivo* would be considered dysfunctional activities, so we characterized these regimes by the proportion of plateaus events among the depolarized phases of the pattern period (See Methods) (Figure 3.3F1 & 3.3F2). The major predictor of the presence of plateaus was low $I_{PumpMax}$, as no plateaus were identified in simulations in which $I_{PumpMax}$ was

above 0.41 nA (Figure 3.3F1 & 3.3F2). Regimes in which either cell exhibited any plateaus were considered dysfunctional and labeled as plateau-containing. Those regimes at low values of $I_{PumpMax}$ which were both asymmetric and contained plateaus, we generally marked as plateau-containing as this property represents a more serious pathological condition. These plateaus appear to be similar to seizure-like plateau activity induced by Co^{2+} or K^{+} blockers in leech neurons (Angstadt & Friesen 1991, Opdyke & Calabrese 1994).

Functional bursting was revealed within a domain of functional regimes on the two-parameter map (Figure 3.4A). Its borders are marked in white on Figures 3.3B, 3.3C, 3.3E, & 3.3F. It exhibited a range of periods from 4.9 seconds to 11.8 seconds. Representative voltage traces from these regimes are shown in Figure 3.4B.

3.5.2 Supporting Functional Bursting Activity through Comodulation

By applying a mask of the area labeled functional to the map of burst periods, we obtained our primary finding; comodulation of the two currents can expand the temporal burst characteristics while retaining the functional pattern. Starting from anywhere in this functional comodulation pathway, shaped like a turning stripe, it is clear that by variation of one parameter along either the $\bar{g}_h$ or the $I_{PumpMax}$ axes, burst period can only be adjusted in a small range before encountering a transition to a dysfunctional regime (Figure 3.4A). By modulating both pump and h-currents together, however, bursting cycle period of the HCO can be smoothly controlled over a wide range (Figure 3.5A).

We searched the functional area of the map and determined the largest viable parameter difference along the $\bar{g}_h$ or the $I_{PumpMax}$ axes. Then, we compared burst characteristics at those boundary parameter values to the maximal difference of parameter and burst characteristics projected along a fitted line of comodulation through the entire functional pathway (See

Methods). By searching along the $I_{PumpMax}$ axis, we found that the greatest continuous range of $\bar{g}_h$ values occurred at $I_{PumpMax}$ = 0.385 nA, where $\bar{g}_h$ could be modulated in the range [3.2, 10] nS to produce a range of burst periods between 7.1 seconds and 4.9 seconds, a difference of 2.2 seconds. The greatest achievable range in burst period by modulation of $\bar{g}_h$ alone through the functional region occurred at $I_{PumpMax}$ = 0.425 nA where $\bar{g}_h$ could be modulated in the range [0, 2.2] nS to produce a range of burst periods between 7.9 seconds and 11.0 seconds. So, by only modulating $\bar{g}_h$, a range of burst period of 3.1 seconds is achievable (Figure 3.5B). Searching along the $\bar{g}_h$ axis, we found that the greatest continuous range of $I_{PumpMax}$ values occurred at $\bar{g}_h$=0 nS, where $I_{PumpMax}$ could be modulated in the range [0.368, 0.500] nA. These two boundary values of $I_{PumpMax}$ produce burst periods of 8.2 seconds and 11.7 seconds respectively, a difference of 3.5 seconds. However, the greatest achievable range in burst periods within this parameter variation occurred at $\bar{g}_h$=0 nS between $I_{PumpMax}$ = 0.398 nA and $I_{PumpMax}$ = 0.444 nA where the burst periods were 7.0 seconds and 11.8 seconds, respectively (Figure 3.5C). So, by changing only $I_{PumpMax}$, a change in burst period of 4.8 seconds is achievable.

To infer a comodulation mechanism coordinating the changes of the pump and h-currents, we first hypothesized that comodulation would be most robust to perturbation if it traversed the center of the functional regime area, navigating away from the borders, and that the simplest comodulation mechanism would be the basic reciprocal relation of the two parameters. We fitted a simple curve representing reciprocal relations between $\bar{g}_h$ and $I_{PumpMax}$ to all points, *i.e.* parameter pairs, in the functional parameter area on the map (R^2=0.7):

$$I_{PumpMax}(\bar{g}_h) = 0.3 + \frac{0.85}{(\bar{g}_h + 5.7)} \qquad \textit{Eq. 30}$$

Maximal parameter distance along this curve was between points in parameter space ($\bar{g}_h$, $I_{PumpMax}$) = (0.0, 0.446) and ($\bar{g}_h$, $I_{PumpMax}$) = (10, 0.354). Between these two points in parameter space along the curve of comodulation, we found that burst period could be varied between 11.8 seconds and 5.6 seconds for a maximum achievable range of 6.2 seconds. This occurred between the parameter points ($\bar{g}_h$, $I_{PumpMax}$) = (0.0, 0.446) and ($\bar{g}_h$, $I_{PumpMax}$) = (9.8, 0.355). These results demonstrate that the burst period could be modified over a larger range under comodulation (6.2 seconds) than under single parameter variation (4.8 seconds). This mapping shows that comodulation is a viable mechanism for expanding the range of achievable temporal characteristics. Maximal distances between parameter pairs and maximal ranges in burst statistics for each search condition are provided in Table 3.1.

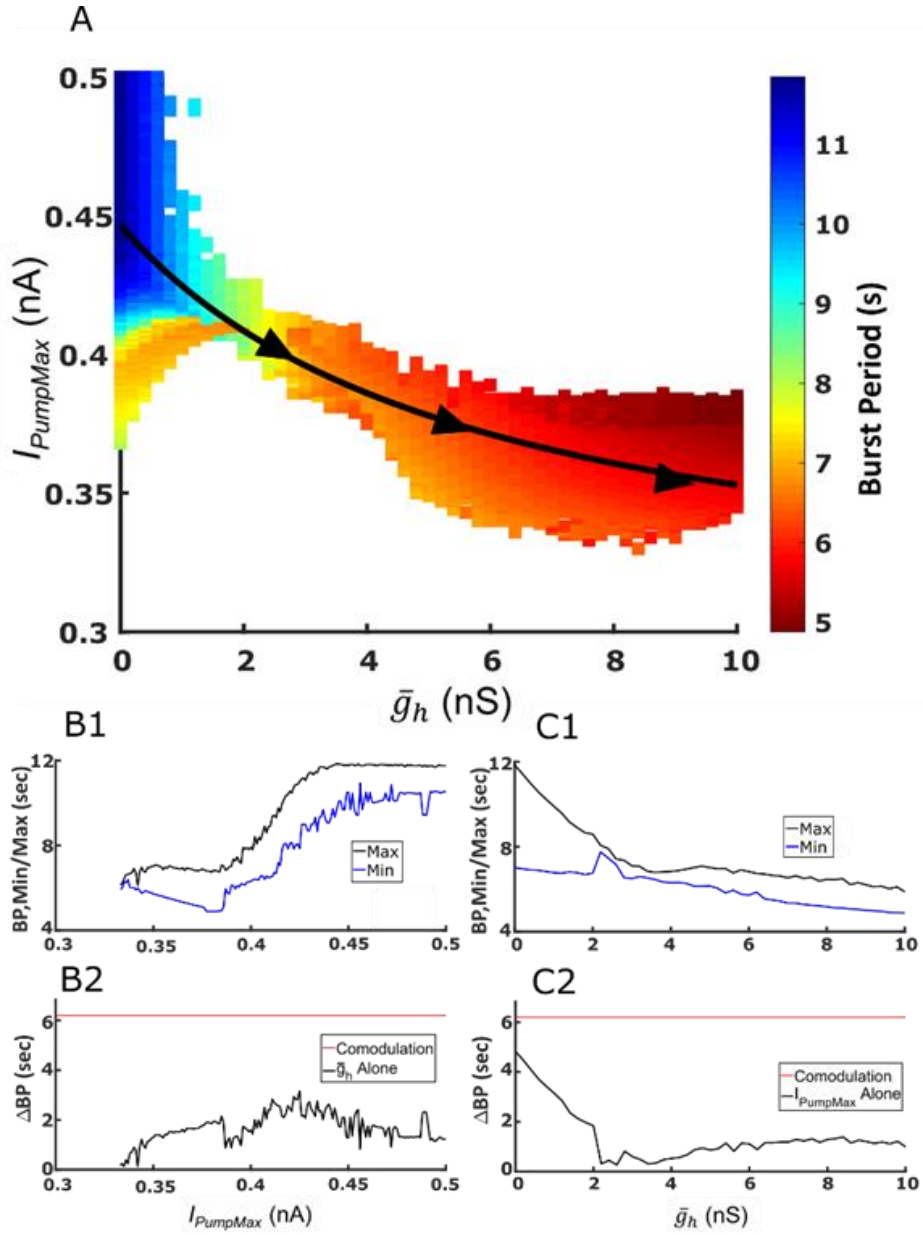

Figure 3.5 Comodulation Widens the Achievable Range of Periods

A color map of burst period within the area supporting the functional regime (A) demonstrates that comodulation of $\bar{g}_h$ *and* $I_{PumpMax}$ expands the range of functional bursting. Overlaid in black is a curve fit of all points in the functional parameter space. This curve represents a general path of smooth comodulation introduced by the application of myomodulin, and it has the form:

$$I_{PumpMax}(\bar{g}_h) = 0.3 + \frac{0.85}{(\bar{g}_h + 5.7)}$$

Arrows indicate the direction travelled by the HCO model through parameter space to represent increased modulation by myomodulin. (B1) Minimum (blue) and maximum (black) achievable period by modulating only $\bar{g}_h$ at all test values of $I_{PumpMax}$. (B2) Maximal possible change in burst period modulating only $\bar{g}_h$ (black) is less than the achievable change in burst period through comodulation (single value marked in red). (C1) Minimum (blue) and maximum (black) achievable period by modulating only $I_{PumpMax}$ at all test values of $\bar{g}_h$. (C2) Maximal possible change in burst period modulating only $I_{PumpMax}$ (black) is less than the achievable change in burst period through

comodulation (single value marked in red). Global maxima in possible shifts in parameter, burst period, and burst duration within the functional regime are included in Table 3.2.

3.5.3 Model Validation and Experimental Results

In concert, we performed extracellular recordings of pairs of HN(3) or HN(4) neurons -- treated equivalently as there have been no observed consistent differences in these HCOs (Kueh et al. 2016) – under control conditions and for three different doses of myomodulin (1 μM, 10 μM, 100 μM) (Figure 3.6A). Across experiments (n=5), myomodulin concentration accounted for the variance in burst period ($p<0.0001$) and burst duration ($p<0.0001$). The general trend supported our previous studies which had found that the addition of 1 μM myomodulin decreased burst period from 12.1 s ± 1.2 s to 6.8 s ± 1.0 s (Tobin & Calabrese 2005). These new experiments also showed that myomodulin affects the burst period in a dose-dependent manner (control: 9.0 s ± 0.7 s; myomodulin 1 μM: 6.4 s ± 0.3 s; myomodulin 10 μM: 5.6 s ± 0.3 s; myomodulin 100 μM: 4.2 s ± 0.1 s)(Figure 3.6A1). Significant differences in burst period and burst duration were found between control conditions and each myomodulin condition ('*' in Figure 3.6A1-2, $p<0.05$ for each), and between the 1 μM and 100 μM conditions ('#' in Figure 3.6A1-2, $p<0.05$). Higher doses of myomodulin caused a greater decrease in period.

A second set of experiments was performed with Cs^+ (2mM), an h-current blocker, to evaluate whether the model matches the action of myomodulin on the pump current alone. Extracellular recordings were performed on HN(3) or HN(4) neurons under control conditions, Cs^+ conditions, and the same three doses of myomodulin now with Cs^+ introduced prior to application of each dose of myomodulin (Figure 3.7A). Here, the period is also affected in a dose-dependent manner (control: 8.4 s ± 0.3 s; Cs^+: 9.6 s ± 0.6 s; myomodulin 1 μM + Cs^+: 7.8 s ± 0.5 s; myomodulin 10 μM + Cs^+: 6.6 s ± 0.3 s; myomodulin 100 μM + Cs^+: 4.4 s ± 0.2 s) (Figure 3.7A1). Across 5 experiments, we found that the variances in burst period and burst

duration were accounted for by treatment effects ($p<0.0001$ and $p<0.0001$ respectively). Significant differences in burst period and burst duration were found between the control condition and the myomodulin 10 μM + Cs^+ and myomodulin 100 μM + Cs^+ conditions ('*' in Figure 3.7A1-2, $p<0.05$ for each). All combined treatment conditions demonstrated significant differences in burst period and burst duration from the Cs^+ alone condition ('†' in Figure 3.7A1-2, $p<0.05$ for each). Burst period was significantly different between all combined treatment conditions ('#' in Figure 3.7A1, $p<0.05$ for each), but burst duration was only significant between myomodulin 10 μM + Cs^+ and myomodulin 100 μM + Cs^+ conditions ('#' in Figure 3.7A2, $p<0.05$ for each)

To verify our model, for each experimental condition, we identified a single "best fit" point within the functional area of the map (Figures 3.6B,3.7B) at which differences between model values of burst duration and burst period and corresponding experimental values were minimal (Eq. 27, Table 3.1). These selected points represent the neuromodulation induced by the different doses of myomodulin; experimental conditions with higher concentrations of myomodulin map to model parameter domains at higher $\bar{g}_h$ and lower $I_{PumpMax}$ (Figure 3.6B), consistent with the findings of Tobin & Calabrese (2005). The point of best fit between model and Cs^+ conditions occurred at $\bar{g}_h$= 1 nS and $I_{PumpMax}$ = 0.448 nA. This point is near the control conditions, but with a lower $\bar{g}_h$ value, which is consistent with the blocked h-current experimental condition. The remaining conditions with myomodulin and Cs^+ were then mapped to points in the functional area of the map with the same $\bar{g}_h$ values under the presumption that in this model $\bar{g}_h$= 1 nS represents an h-current blocked by Cs^+ (Figure 3.7B). There was good agreement between model and experiment for the Cs^+ with 1 μM myomodulin and Cs^+ with 10

μM myomodulin conditions, while the Cs^+ with 100 μM myomodulin was mapped to the same point in parameter space as the Cs^+ with 10 μM myomodulin.

In conclusion, model burst duration and burst period have good agreement for experimental values under all conditions except Cs^+ with 100 μM myomodulin. As the dose of myomodulin increases, burst period and burst duration decrease and correspond to higher $\bar{g}_h$ values and lower $I_{PumpMax}$ values on the map. Direct comparisons between model and experimental voltage traces for both sides of the HCO are provided in Figures 3.6C and 3.7C.

To test whether reciprocal relation of the two currents could describe experimental data, we then fit a comodulation curve over to the selected parameter value representations of experimental activity, and suggest that the reciprocal relationship may describe the comodulation of h-current and Na^+/K^+ pump current by myomodulin (R^2=*0.97*) (Figure 3.6B):

$$I_{PumpMax}(\bar{g}_h) = 0.36 + \frac{0.16}{(\bar{g}_h + 0.85)} \qquad \textit{Eq. 31}$$

This experimentally justified comodulation curve has an even greater range of achievable periods than the midline comodulation curve. Maximal parameter distance here occurred between the boundary points ($\bar{g}_h$, $I_{PumpMax}$) = (0.4, 0.491) and ($\bar{g}_h$, $I_{PumpMax}$) = (10, 0.38) where the burst period was 11.7 and 4.9 seconds, respectively. In this case, burst period could be changed by up 6.8 seconds, as compared to the midline comodulation curve which could achieve a 6.2 second range, the modulation of only $I_{PumpMax}$ which could achieve a 4.8 second range, and the modulation of $\bar{g}_h$alone which could achieve a 3.1 second range. Remarkably, this comodulation curve and the experimental points were not in the center of the functional regime, but close to the borders of the asymmetric regime. In retrospect, this made sense, as a perturbation resulting in mild asymmetry would not be nearly as catastrophic as a perturbation resulting in a depolarization block.

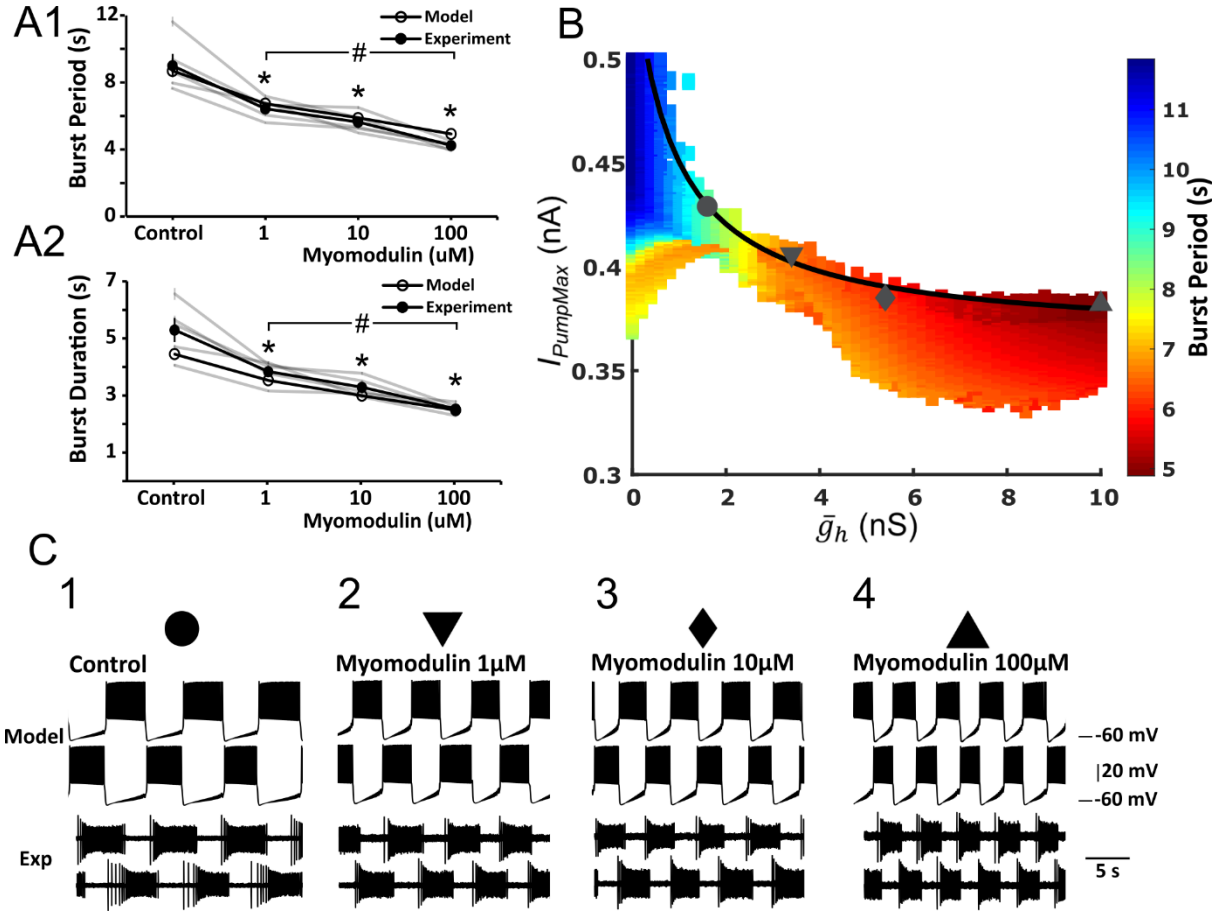

Figure 3.6 Model Reproduces Myomodulin Results

Mapping experimental results with myomodulin onto the model parameter plane suggest a specific comodulation curve. (A) Statistical comparisons of myomodulin dose-response of experimentally measured burst period and burst duration are provided. In addition, burst period and burst duration means of individual animals (n=5) are included in gray. Significant differences in sample means were found between control and all myomodulin conditions (* $p<0.05$) as well as between 1µM myomodulin and 100µM myomodulin (# $p<0.05$), suggesting a dose effect. Error bars on the experimental series represent the standard error of the mean. Model means for burst period and burst duration for best representative cases of each experimental condition are included for comparison. In experiments, asymmetry measures (Table 3.7), coefficient of variation of burst period (Table 3.9), and coefficient of variation of burst duration (Table 3.11) were low. Each experimental condition was mapped (B) to a single point on the diagram according to burst period and burst duration associated with a particular dose of myomodulin: control (circle), 1 µM myomodulin (inverted triangle), 10 µM myomodulin (diamond), 100 µM myomodulin (upright triangle). The relationship between $I_{PumpMax}$ and $\bar{g}_h$ is then fitted to the positions in parameter space chosen for control and myomodulin conditions producing the following curve:

$$I_{PumpMax}(\bar{g}_h) = 0.36 + \frac{0.16}{(\bar{g}_h + 0.85)}$$

Chosen parameter sets in the model match well with experimental data. (C) Model voltage traces are compared directly to extracellular recordings of bilateral HN cells from corresponding conditions.

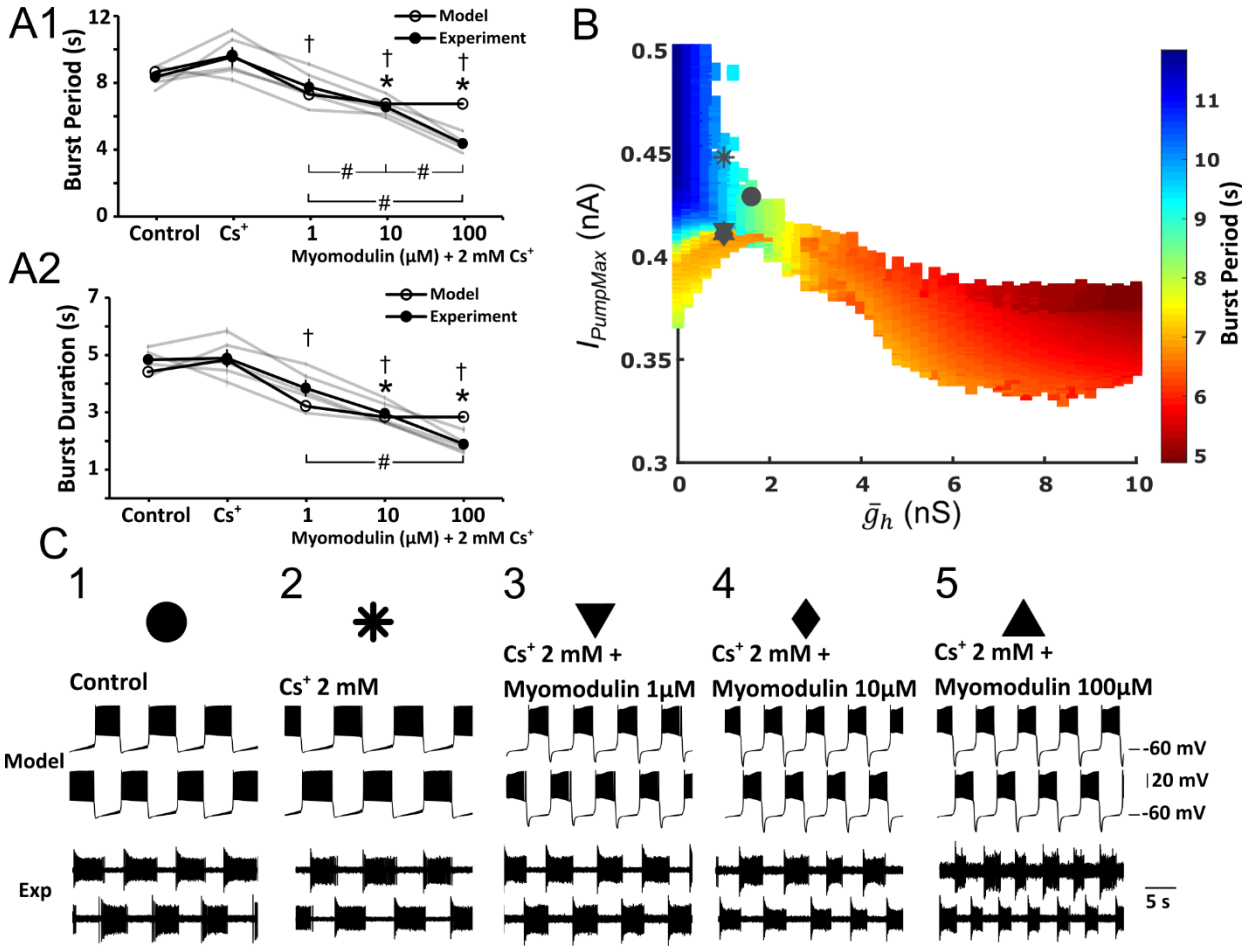

Figure 3.7 Model Reproduces Results from Cesium Experiments

The model matches results from experiments with 2 mM Cs^+ (blocks h-current) and myomodulin. (A) Statistical comparisons of Cs^+ with myomodulin dose-response of experimentally measured burst period (A1) and burst duration (A2) are provided. In addition, burst period and burst duration means of individual animals (n=5) are included in gray. Significant differences in sample means of burst duration and burst period were found between Cs^+-only conditions and all Cs^+ with myomodulin conditions († $p<0.05$) and also between control conditions and the Cs^+ with 1μM myomodulin and Cs^+ with 100μM myomodulin (* $p<0.05$) conditions. Significant differences in burst period and burst duration between Cs^+ with myomodulin conditions are labeled (# $p<0.05$). Error bars on the experimental series represent the standard error of the mean. Model means for burst period and burst duration for best representative cases of each experimental condition are included for comparison. In experiments, asymmetry measures (Table 3.8), coefficient of variation of burst period (Table 3.10), and coefficient of variation of burst duration (Table 3.12) were low. Each experimental condition is mapped (B) to a single point in the map according to burst period and burst duration associated with control and application of Cs^+ with a particular dose of myomodulin: control (circle), Cs^+ (star), Cs^+ with 1 μM myomodulin (inverted triangle), Cs^+ with 10 μM myomodulin (diamond), Cs^+ with 100 μM myomodulin (upright triangle). The 10μM myomodulin and 100μM myomodulin conditions mapped to the same location. (C) Model voltage traces are compared to extracellular recordings of contralateral HN cells from corresponding conditions. HN(R) is the top and HN(L) the bottom trace for both the model and the living neurons.

HN HCOs do not typically burst in asymmetric fashion (Kueh et al. 2016, Wenning et al. 2018). When we analyzed asymmetry in the experimental data set, we saw that across the 5

subjects in the myomodulin experiments and also across the 5 subjects in the combined myomodulin with Cs^+ experiments, average levels of asymmetry, computed in the same manner as the model data, were all less than 0.2, our selected cutoff for model asymmetry. The largest average level of asymmetry was observed in the Cs^+ alone condition with an average asymmetry measure of 0.11 and a standard error of 0.04 across 5 subjects.

The variability in the burst period and burst duration in experiments was relatively small. Means and standard errors for individual leeches are shown alongside grand means and model comparisons in Figures 3.6A & 3.7A. Coefficients of variation of burst period averaged across animals in both the Cs^+ plus myomodulin experiments and the myomodulin only experiments did not exceed 0.1. One subject under control conditions had a coefficient of variation of burst period of 0.12. Across the 5 subjects in the Cs^+ plus myomodulin experiments, variability in the coefficient of variation of burst period between treatment conditions was significant ($p<0.05$), but coefficients of variation were <0.1 in all cases. Coefficients of variation of burst duration averaged across animals in both the Cs^+ plus myomodulin experiments and the myomodulin only experiments were slightly higher but did not exceed 0.13. The highest coefficient of variation of burst duration observed in any one preparation was 0.24 in the 100 μM myomodulin with Cs^+ condition. The effect of the treatment could not account for the variation in the mean coefficient of variation of burst duration ($p>0.05$). For a full analysis of the burst characteristics of the HN CPG from an extensive data set see Wenning et al. (2018).

Table 3.1 Table of Mapped Parameter Values for Experimental Conditions

Points in parameter space selected to represent experimental conditions with burst period and burst duration at those points in parameter space.

Condition	**Model $\bar{g}_h$**	**Model $I_{PumpMax}$**	**Model Burst Period**	**Model Burst Duration**
Control	1.6	0.429	8.69	4.44
Cesium	1.0	0.448	9.68	4.83
1μM Myo	3.4	0.406	6.72	3.52
10μM Myo	5.4	0.385	5.86	2.99
100μM Myo	10	0.382	4.89	2.48
1μM Myo + 2mM Cs	1.0	0.413	7.35	3.2
10μM Myo +2 mM Cs	1.0	0.411	6.78	2.82
100μM Myo + 2mM Cs	1.0	0.411	6.78	2.82

Table 3.2 Maximal Changes in Parameter and Burst Statistics within Functional Regime

Maximal continuous parameter and burst statistic shifts along each axis compared to maximal parameter and burst statistic shifts along a curve fitted to the midline of the functional regime in model parameter space (Figure 3.5A) and along a curve fitted to the experimental (myomodulin) points (Figure 3.6A). Largest shifts in parameter, burst duration, and burst period are searched independently to ensure good agreement. The line of comodulation allows for a larger possible shift in temporal burst characteristics than modulation of either current alone, anywhere in the tested functional regimes on the two-parameter map.

Maximal Change in Parameter Values Within Functional Regime					
Search Axis	**Ipumpmax (nA)**	**gh (nS)**	Burst Duration (s)	Burst Period (s)	Interburst Interval (s)
gh modulated		**6.8**	1.01	2.15	1.14
Ipumpmax modulated	**0.132**		2.06	3.56	1.5
Comodulation(mid line)	**0.092**	**10**	2.77	6.19	3.41
Comodulation (experimental)	**0.111**	**9.6**	3.12	6.81	3.7
Maximal Change in Burst Duration Within Functional Regime					
Search Axis	Ipumpmax (nA)	gh (nS)	**Burst Duration (s)**	Burst Period (s)	Interburst Interval (s)
gh modulated		0.4	**1.42**	2.40	0.98
Ipumpmax modulated	0.09		**2.8**	4.70	1.90
Comodulation (midline)	0.091	9.8	**2.86**	6.20	3.34
Comodulation (experimental)	0.11	8.8	**3.2**	6.68	3.49
Maximal Change in Burst Period Within Functional Regime					
Search Axis	Ipumpmax (nA)	gh (nS)	Burst Duration (s)	**Burst Period (s)**	Interburst Interval (s)
gh modulated		2.2	1.13	**3.16**	2.03
Ipumpmax modulated	0.046		2.78	**4.83**	2.05

Comodulation (midline)	0.091	9.8	2.86	**6.20**	3.34
Comodulation (experimental)	0.111	9.6	3.12	**6.81**	3.7

Table 3.3 Repeated Measures ANOVA - Myomodulin Experiments

Repeated measures ANOVA for myomodulin experiments. Difference between drug conditions were statistically significant ($p<0.05$).

Burst Period

Source	DF	SS	MS	F	Fcrit	*p*
Total	19	76.82	4.04			
Subject	4	6.03	1.51	2.39	3.26	0.1091
Drug	3	63.21	21.07	33.35	3.49	<0.0001
Error	12	7.58	0.63			

Burst Duration

Source	DF	SS	MS	F	Fcrit	*p*
Total	19	25.48	1.34			
Subject	4	2.03	0.51	2.11	3.26	0.2826
Drug	3	20.57	6.86	28.59	3.49	<0.0001
Error	12	2.88	0.24			

Table 3.4 Repeated Measures ANOVA - Cesium Experiments

Repeated measures ANOVA for cesium + myomodulin experiments. Difference between drug and subject conditions were statistically significant ($p<0.05$).

Burst Period						
Source	DF	SS	MS	F	Fcrit	*p*
Total	24	92.55	3.856			
Subject	4	7.47	1.87	3.98	3.01	0.0189
Drug	4	77.58	19.4	41.38	3.01	<0.0001
Error	16	7.5	0.469			
Burst Duration						
Source	DF	SS	MS	F	Fcrit	*p*
Total	24	38.62	1.61			
Subject	4	2.95	0.74	4.69	3.01	0.0107
Drug	4	33.16	8.29	52.71	3.01	<0.0001
Error	16	2.52	0.16			

Table 3.5 Post-hoc Pairwise Comparisons – Myomodulin Experiments

Post-hoc pairwise comparisons computed using Tukey's HSD for myomodulin experiments. Significant differences in burst duration and burst period were found between control and all conditions as well as between 1μM myomodulin and 100μM myomodulin conditions.

Tukey's HSD

Burst Period

Comparison						
Condition (B)	Condition (A)	$\lvert X_B - X_A \rvert$	q	q_{crit}	$p<0.05$	Symbol
Control	1μM myomodulin	2.61	7.34	4.199	Yes	*
	10 μM myomodulin	3.48	9.8	4.199	Yes	*
	100 μM myomodulin	4.88	13.72	4.199	Yes	*
1μM myomodulin	10 μM myomodulin	0.87	2.46	4.199	No	NA
	100 μM myomodulin	2.27	6.37	4.199	Yes	#
10 μM myomodulin	100 μM myomodulin	1.39	3.92	4.199	No	NA

Burst Duration

Comparison						
Condition (B)	Condition (A)	$\lvert X_B - X_A \rvert$	q	q_{crit}	$p<0.05$	Symbol
Control	1μM myomodulin	1.47	6.69	4.199	Yes	*
	10 μM myomodulin	2.01	9.18	4.199	Yes	*
	100 μM myomodulin	2.77	12.66	4.199	Yes	*
1μM myomodulin	10 μM myomodulin	0.55	2.49	4.199	No	NA
	100 μM myomodulin	1.31	5.97	4.199	Yes	#
10 μM myomodulin	100 μM myomodulin	0.76	3.48	4.199	No	NA

Table 3.6 Post-hoc Pairwise Comparisons - Cesium Experiments

Post-hoc pairwise comparisons computed using Tukey's HSD for cesium experiments.

Tukey's HSD

Burst Period

Comparison						
Condition (B)	Condition (A)	$\lvert X_B - X_A \rvert$	q	q_{crit}	$p<0.05$	Symbol
Control	Cs 2mM	1.16	3.8	4.33	No	NA
	Cs + 1 µM myomodulin	0.622	2.49	4.33	No	NA
	Cs + 10 µM myomodulin	1.85	6.03	4.33	Yes	*
	Cs + 100 µM myomodulin	4.0	13.05	4.33	Yes	*
Cs 2mm	Cs + 1 µM myomodulin	1.79	5.83	4.33	Yes	†
	Cs + 10 µM myomodulin	3.01	9.83	4.33	Yes	†
	Cs + 100 µM myomodulin	5.16	16.86	4.33	Yes	†
Cs + 1 µM myomodulin	Cs + 10 µM myomodulin	3.38	13.51	4.33	Yes	#
	Cs + 100 µM myomodulin	1.22	4.9	4.33	Yes	#
Cs + 10 µM myomodulin	Cs + 100 µM myomodulin	2.15	8.61	4.33	Yes	#

Burst Duration

Comparison						
Condition (B)	Condition (A)	$\lvert X_B - X_A \rvert$	q	q_{crit}	$p<0.05$	Symbol
Control	Cs 2mM	0.06	0.31	4.33	No	NA
	Cs + 1 µM myomodulin	1	4	4.33	No	NA
	Cs + 10 µM myomodulin	1.89	10.64	4.33	Yes	*
	Cs + 100 µM myomodulin	2.96	16.71	4.33	Yes	*
Cs 2mm	Cs + 1 µM myomodulin	1.06	5.95	4.33	Yes	†
	Cs + 10 µM myomodulin	1.94	10.96	4.33	Yes	†
	Cs + 100 µM myomodulin	3.02	17.03	4.33	Yes	†
Cs + 1 µM myomodulin	Cs + 10 µM myomodulin	0.89	3.55	4.33	No	NA
	Cs + 100 µM myomodulin	1.96	7.85	4.33	Yes	#
Cs + 10 µM myomodulin	Cs + 100 µM myomodulin	1.08	4.31	4.33	No	NA

3.6 Discussion

Neuromodulation allows neuronal networks to flexibly adapt to changing behavioral goals and variable environments. An important question posed by experiments with CPGs is why neuromodulators target more than one membrane current. Also intriguing -- why is Na^+/K^+ pump current among targeted currents? The leech heartbeat CPG is an ideal system for exploring these questions, offering well-described cellular and circuit dynamics and a biophysical model rooted in experimental data. We investigated activities of a biophysical model of the leech heartbeat half-center oscillator (HN HCO) under parameter variation of the maximal conductance of the h-current ($\bar{g}_h$) and the maximal pump current ($I_{PumpMax}$). This model of comodulation in leech HNs revealed a mechanism which allows an HCO to regulate its period in a range which is unattainable through modulation of a single current. The two-parameter map of activities revealed a stripe of parameters supporting functional bursting. It is located between large areas of two dysfunctional patterns, asymmetric bursting and plateau-containing seizure-like activity. Within the functional range, we found points which readily matched results from myomodulin dose-dependence experiments. The curve of modulation fitted to these experimental data tracks very close to the border of the asymmetric regime, and far from the more pathological plateau-containing regime. The mechanism of comodulation of the pump and h- currents, identified as their reciprocal relation, expands the functional ranges of $\bar{g}_h$ and $I_{PumpMax}$ by navigating between the areas producing dysfunctional patterns. The comodulation offers more than simple synergistic augmentation of the cycle period range, it expands the range of functional bursting periods by 42% compared to modulation of $I_{PumpMax}$ alone or 119% compared to modulation of $\bar{g}_h$ alone. Thus, investigating the modulatory space of models can reveal complex interactions

which are difficult to isolate in experiments. This comodulation mechanism allows the HCO circuit to produce functional bursting, while regulating its temporal properties in a wide range.

3.6.1 Pump Current Contributes Directly to the Dynamics of Rhythm Generation

The role of the Na^+/K^+ pump in the dynamics of rhythm generating circuits is not well understood. By executing a vital housekeeping function of maintaining Na^+ and K^+ gradients across the membrane, it generates an outward current which must be accounted for in the checks-and-balances of oscillatory pattern generating dynamics. Multiple studies, computational and experimental, have shown how its electrogenic nature is fundamental to the excitability of neurons (Forrest et al. 2012, Krishnan 2015, Kueh et al. 2016, Picton et al 2017). Here, we show that the pump's contribution is critical for robust yet flexible control of bursting. Significantly, in this HN HCO circuit, modifications to I_{Pump} have immediate consequences to the bursting rhythm. Blockage or large reductions in pump activity affect Na^+ and K^+ ionic gradients with consequent effects on bursting rhythms over the time scale of several bursts. For example, blocking the pump with strophanthidin gradually disrupts the HN HCO's rhythm as the cells reach a depolarization block and are unable to fire action potentials (Kueh et al 2016). Furthermore, in HN HCOs, I_{Pump} is a large, active component contributing to bursting dynamics through interaction with Na^+ and other currents, and its down-modulation can be used as an effective mechanism to regulate temporal burst characteristics. The pump current interacts with h-current during the interburst interval both activating it by causing hyperpolarization and opposing it by being an outward current. Imbalance between these currents leads to plateau-containing, highly variable activity or asymmetric activity which would be maladaptive for the animal. I_{Pump} is thus an active contributor to the dynamics of rhythm generation on both long and

short timescales. The ability of I_{Pump} to act on short timescales supports its potential role in information processing as well (Forrest 2014).

3.6.2 Relation to Homeostatic Mechanisms

With the exception of the asymmetric cases, the duty cycle of the model is very close to 50%, while experimental traces typically display a duty cycle of around 60% in control and myomodulin alone. This has been a consistent discrepancy with the HN HCO model since its inception (Hill et al. 2001). The onset of spiking in the model is abrupt at the end of inhibition owing to the single compartment nature of the model; a choice that enhances dynamical analysis but sacrifices the nuances of spiking activity. Despite this issue, these HN HCO models have had predictive value and reproduced the core properties of burst generation in a variety of pharmacological, dynamic clamp, and hybrid-system experiments (Hill et al. 2001, Cymbalyuk et al. 2002, Sorensen et al. 2004, Olypher et al. 2006, García et al. 2008, Weaver et al. 2010, Kueh et al. 2016). We note that in our experiments, the mean duty cycle across animals decreased to 50% in Cs^+ and as low as 40% in Cs^+ with 100 μM myomodulin.

We found higher levels of animal-to-animal variability in the myomodulin and Cs^+ experiments, suggesting that the modulatory effects on the pump alone may vary between individual animals. We propose that Na^+/K^+ pump expression levels may be variable between animals, but that at least some other channel expressions, including the h-current, may be coregulated with pump to preserve the described mechanism of comodulation. It is well established that ion channel expression is homeostatically coregulated to bound the types of produced activity (Khorkhova & Golowasch 2007, Marder 2011, O'Leary et al. 2013, Golowasch 2019, Goaillard & Marder 2021). Such homeostatic mechanisms prevent significant deviations from a functional pattern through compensation – a negative feedback loop. While the

mechanisms which regulate the proportion of ion channels in the membrane may be in place to bound activity, comodulation of the currents which are already present is a separate problem. We emphasize with this system that comodulation is an active measure which controls the activity in a wide range while simultaneously avoiding catastrophic dysfunction. From a modeling perspective, the methodology for investigating comodulation and coregulation is similar, but these processes serve different biological functions. While coregulation *preserves* the activity produced in the face of perturbation and long-term changes, comodulation *changes or scales* the activity, in this case the period.

3.6.3 Proximity to Less Dangerous Boundary Increases Robustness

Model investigation of the modulation mechanisms should consider the multiparameter space of modulatory action (Goldman et al. 2001). Here, by covarying two currents implicated in comodulation by myomodulin, we found that the experimentally verified comodulation curve tracks very closely to the edge of our defined functional regime (Figure 3.6B) which borders the asymmetric regimes. The transition at this edge from functional activity to asymmetric activity is a smooth one, not a catastrophic transition like the border between functional and plateau activity and this positioning may contribute robustness to the HCO. Robust functional bursting in this circuit is critical for the animal's survival, as outputs of HN neurons drive the motor neurons which control the tubular leech hearts. Plateauing seizure-like activity of these cells alone would be deleterious for heart function and could also disrupt ionic gradients, so avoidance of the plateau-containing regime would be critical. This regime is reminiscent of seizure-like plateau activity induced in leech neurons including HNs by substitution of Ca^{2+} with Co^{2+} or by application of K^+ channel blockers (Angstadt & Friesen 1991, Opdyke & Calabrese 1994). Small variations in symmetry of the activity, however, would have little to no consequences for the

animal's welfare. Since two asymmetric regimes coexist, in the living animal, biological noise would likely switch the HCO back and forth between them, resulting in nearly symmetric bursting patterns with burst durations equal on average.

3.6.4 Multiple Targets of Neuromodulation

In some circuits, neuromodulators that produce multiple effects and target different currents in opposite directions may create a mechanism protecting circuits against overmodulation which would lead a circuit into a dysfunctional regime (Harris-Warrick & Johnson 2010). Modulators with apparently opposing effects can also underlie complex transient responses because they act on different timescales. Studies on the *Aplysia* radular neuromuscular system demonstrate that two different classes of modulators are co-released with acetylcholine (Brezina et al. 2003), myomodulins (MM) and small cardiac peptides (SCP). These modulators have apparently opposing effects on the muscle and occur on different timescales. Experimentally, MMs decrease muscle contractile responses to acetylcholine, while SCPs increase the contractile response of the muscle. The long timescale effects of these modulators on the enhancement of calcium current and muscle relaxation rate allow the system to have a "memory" of the previous behavioral state (activity pattern) when changes occur and increase efficient muscle performance throughout multiple cycles. The fast effects on enhancement of potassium current in the muscle allow the system to adapt when the motor pattern changes with minimal losses in performance. These modulatory systems also allow the muscle contractions to be robust in the face of irregular firing patterns often seen in the behaving animal (Brezina et al. 2005) and to navigate through the parameter space to regions unreachable in the steady state to optimize muscle response throughout different motor patterns. From a neuronal circuit's perspective, use of multiple modulators with multiple cellular targets is functionally similar to

our case, where a single modulator affects multiple targets within the cell. We found that even in the steady state, the effect of modulating multiple ionic currents has tangible benefits for navigating the complex control space of the motor rhythm output. Furthermore, while overmodulation implies that the magnitude of modulation can exceed a functional range and lead a circuit into a dysfunctional regime, in the leech heartbeat HCO (comodulation with similar effects) and in the *Aplysia* radular neuromuscular system (comodulation with opposing effects), control is not achieved by mitigation of an effect, but rather by the complex combination of effects. These findings enforce that studies on neuromodulation should be utilizing specific, system-relevant combinations of neuromodulator-targeted factors rather than single factors, one at a time. Computational modeling helps bridge this gap by reproducing the emergent properties of a neuronal circuit when physiological studies become less feasible. With their ability to capture these emergent properties from the combination of more basic mechanisms, models can be studied as a dynamical system which then can be evaluated with simpler, targeted multi-factor physiological experiments.

Supplemental Tables

Table 3.7 Asymmetry measures from myomodulin only experiments

Asymmetry (Experimental Set 1)

Preparation	Control	Myomodulin 1μM	Myomodulin 10 μM	Myomodulin 100 μM
Prep 1	0.024	0.039	0.071	0.126
Prep 2	0.024	0.043	0.04	0.007
Prep 3	0.103	0.027	0.022	0.051
Prep 4	0.075	0.071	0.089	0.07
Prep 5	0.032	0.052	0.102	0.067
Mean	0.052	0.046	0.065	0.064
n	5	5	5	5
SEM	0.016	0.007	0.015	0.019

Table 3.8 Asymmetry measures from combined treatment experiments

Asymmetry (Experimental Set 2)

Preparation	Control	Cs^+ 2mM	Cs^+ 2mM + Myomodulin 1μM	Cs^+ 2mM + Myomodulin 10 μM	Cs^+ 2mM + Myomodulin 100 μM
Prep 6	0.077	0.033	0.043	0.021	0.025
Prep 7	0.117	0.207	0.091	0.069	0.094
Prep 8	0.023	0.119	0.061	0.126	0.171
Prep 9	0.079	0.109	0.004	0.042	0.02
Prep 10	0.135	0.057	0.023	0.099	0.03
Mean	0.086	0.105	0.044	0.071	0.068
n	5	5	5	5	5
SEM	0.019	0.03	0.015	0.019	0.029

Table 3.9 Coefficient of variation of burst period from myomodulin only experiments

Coefficient of Variation of Burst Period (Experimental Set 1)

Preparation	Control	Myomodulin 1μM	Myomodulin 10 μM	Myomodulin 100 μM
Prep 1	0.03	0.028	0.034	0.029
Prep 2	0.128	0.069	0.021	0.034
Prep 3	0.031	0.043	0.062	0.022
Prep 4	0.044	0.032	0.025	0.028
Prep 5	0.047	0.043	0.072	0.042
Mean	0.056	0.043	0.043	0.031
n	5	5	5	5
SEM	0.018	0.007	0.01	0.003

Table 3.10 Coefficient of variation of burst period from combined treatment experiments

Coefficient of Variation of Burst Period (Experimental Set 2)

Preparation	Control	Cs^+ 2mM	Cs^+ 2mM + Myomodulin 1μM	Cs^+ 2mM + Myomodulin 10 μM	Cs^+ 2mM + Myomodulin 100 μM
Prep 6	0.02	0.057	0.06	0.045	0.067
Prep 7	0.041	0.095	0.058	0.057	0.045
Prep 8	0.037	0.063	0.06	0.076	0.084
Prep 9	0.041	0.119	0.059	0.057	0.038
Prep 10	0.031	0.054	0.068	0.084	0.031
Mean	0.034	0.078	0.061	0.064	0.053
n	5	5	5	5	5
SEM	0.004	0.013	0.002	0.007	0.01

Table 3.11 Coefficient of variation of burst duration from myomodulin only experiments

Coefficient of Variation of Burst Duration (Experimental Set 1)

Preparation	Control	Myomodulin 1μM	Myomodulin 10 μM	Myomodulin 100 μM
Prep 1	0.057	0.053	0.073	0.101
Prep 2	0.154	0.127	0.055	0.086
Prep 3	0.082	0.068	0.072	0.051
Prep 4	0.071	0.053	0.067	0.058
Prep 5	0.122	0.119	0.141	0.113
Mean	0.097	0.084	0.082	0.082
n	5	5	5	5
SEM	0.018	0.016	0.015	0.012

Table 3.12 Coefficient of variation of burst duration from combined treatment experiments

Coefficient of Variation of Burst Duration (Experimental Set 2)

Preparation	Control	Cs^+ 2mM	Cs^+ 2mM + Myomodulin 1μM	Cs^+ 2mM + Myomodulin 10 μM	Cs^+ 2mM + Myomodulin 100 μM
Prep 6	0.06	0.073	0.086	0.137	0.155
Prep 7	0.086	0.199	0.115	0.086	0.097
Prep 8	0.076	0.101	0.105	0.161	0.24
Prep 9	0.07	0.160	0.069	0.054	0.086
Prep 10	0.084	0.091	0.153	0.178	0.067
Mean	0.075	0.125	0.106	0.123	0.129
n	5	5	5	5	5
SEM	0.005	0.024	0.014	0.023	0.031

4 SYNAPTIC INHIBITION COUNTERACTS THE EFFECTS OF A DOWN-MODULATED NA^+/K^+ PUMP CURRENT TO AVOID DYSFUNCTIONAL RHYTHMS

4.1 Abstract

Specialized oscillatory neural circuits, central pattern generators (CPGs), control rhythmic movements like breathing, locomotion, and heartbeat in invertebrates. Their rhythmic patterns of activity are adjusted by neuromodulation to meet environmental challenges.

Neuromodulation of the leech heart interneuron half-center oscillator (HN HCO) navigates the CPG between dysfunctional regimes by reducing Na^+/K^+ pump current and increasing hyperpolarization activated (h-) current in a coordinated inverted fashion. We revealed that this comodulation path traverses a domain of parameters where a disconnected single cell exhibits severely dysfunctional plateau-containing seizure-like activity.

We also discovered that in this domain of the HCO model, there are two bursting patterns, and both meet the criteria of functional bursting activity of this circuit. While cycle period and burst duration of the patterns are roughly the same, one of these regimes has two-times higher intra-burst spike frequency. This finding suggests that neuromodulation could introduce additional functional regimes with higher spike frequency, and thus “stronger” synaptic transmission to motor neurons which might reflect a “second gear” of a rhythmic motor pattern.

Deficiency of inhibition is often cited as a cause of seizures and other dysfunctional neural activities. Due to the electrogenic nature of the Na+/K+ pump, it provides an important source of negative feedback to bursting cells and contributes to transitions between phases of bursting activity. Activation of the Na+/K+ pump current does not depend on the cell’s

membrane potential and it is active throughout the bursting cycle period. Along with the cell's depolarization, intracellular Na+ concentration grows and activates the outward pump current which contributes to burst termination. We demonstrate that counterintuitively, modulation which decreases the maximal pump current, can actually increase the pump current throughout the bursting cycle. Here we demonstrate in a model of a central pattern generator that small down-modulation of the pump current can result in a rhythm with double spike frequency. The high excitability of the single cells can be harnessed by mutually inhibitory synaptic interactions of the HCO into functional bursting pattern.

4.2 Introduction

The half-center oscillator (HCO) is a ubiquitous rhythm generating neural network motif. HCOs consist of pairs of cells or paired networks of cells, which mutually inhibit one another and have current and synaptic dynamics which produce alternating patterns of activity. HCOs can drive central pattern generator (CPG) networks to produce rhythmic activity for behaviors such as locomotion. Processes which modulate or coregulate membrane currents can push electrically excitable cells near the limits of the dynamical characteristics which allow them to produce functional activity. Modulation must be carefully managed (Harris-Warrick & Johnson 2010). Even small changes to the biophysical properties of a cell can result in dynamical states such as silence or multistability (Barnett et al. 2013, Malashchenko et al. 2011, Marin et al. 2013, Ellingson et al. 2019). Multistability is a phenomenon in which a dynamical system is capable of producing distinctly different patterns of activity given the same parameters due the presence of multiple attractors, and it has been identified in a variety of neuronal systems (Marin et al. 2013, Barnes et al. 1997, Newman 2010). While some multistable regimes are functional, others lurk below the surface in the dynamics and represent pathological states if they are realized. The

network structure of HCOs can help to protect against pathological cellular dynamics including coexistence of functional and dysfunctional regimes (Cymbalyuk et al 2002, Marin et al. 2013). The synaptic inhibition can mitigate extreme dynamics present in the single neurons which make them up.

In the previous chapter, we reported on how myomodulin in a leech heartbeat central pattern generator half-center oscillator (HCO) comodulates the h-current and the Na^+/K^+ pump current to control the period of activity in a wide range while avoiding dysfunctional regimes (Ellingson et al. 2021, Ch. 3). The Na^+/K^+ pump has been implicated in the transition to seizure-like plateau containing activity (Krishnan et al. 2015). We hypothesized that given the prevalence of plateaus at low values of maximal pump current, $I_{PumpMax}$, in our leech heart interneuron (HN) HCO model, that the half-center structure may protect the system from succumbing to underlying pathological single cell dynamics.

Here we present the discovery of a multistable functional regimes in the HCO model under modulated conditions and investigate the parameter space of modulation in a single cell HN model. We describe several regimes and present a connection for future investigation.

4.3 Methods

4.3.1 Model and Parameter Sweeps

HN HCO Model is as presented in Ellingson et al. 2021. The single cell model uses the same set of equations without synapses or equations for a second cell. Parameter sweeps for the single cell model are conducted in the same manner as well.

Simulation along the line of comodulation was accomplished by first setting parameter values ($\bar{g}_h$, $I_{PumpMax}$) = (0,0.548) and initializing with the standard set of initial conditions (S2).

Then, after simulation, $\bar{g}_h$ is increased by 0.1 nS, and $I_{PumpMax}$ is decreased in accordance with the comodulation equation derived from our previous work:

$$I_{PumpMax}(\bar{g}_h) = 0.36 + \frac{0.16}{(\bar{g}_h + 0.85)}$$

After each simulation, the values of all state variables were then used as initial conditions in the next simulation. This allowed us to smoothly simulate the action of myomodulin.

4.3.2 Spike Averaging and Phasewise Analysis of Currents

For each spike, state variables, currents, and fluxes were averaged over its duration to assess their contributions through a bursting cycle. Once spike times were identified using previously described methods, spike floors were identified as the minimum value of membrane potential between spikes. These points were then used to set spike duration and to smooth time series of state variables, currents, and Na+ fluxes. Between spike floors, all values for a trace were set to the average value between spike floors. To compute average current and flux contributions over a cycle, clean depolarized and hyperpolarized phases were sliced out of a cycle, and traces were separately integrated using the trapezoidal Riemann sum method (trapz() in MATLAB) and normalized to the duration of the phase.

4.4 Results

4.4.1 Multistability of High and Low Spike Frequency Bursting Regimes in the HCO Model

We used a model of a leech heart interneuron half-center oscillator (HN HCO) for which we identified a mechanism for robust control of period (Ellingson et al., 2021, Ch. 3). We had also identified pairs of model parameter values for $I_{PumpMax}$ and $\bar{g}_h$ which correspond to

experimentally recorded activity from a myomodulin dose response. We described the effect of myomodulin by a simple comodulation path.

Based on our modeling analysis, we demonstrated that by following this myomodulin comodulation path, the HN HCO avoids a dysfunctional asymmetric regime at higher levels of $I_{PumpMax}$ and $\bar{g}_h$ as well as a dysfunctional seizure-like plateau-containing regime at lower levels of $I_{PumpMax}$ and in doing so achieves a larger range of burst duration and bursting cycle period.

A two-parameter map of spike frequency indicated the existence of a high-spike frequency regime within the boundaries of the functional regime in our HCO model (Figure 4.1A). Typical mean spike frequencies for the low frequency regime were on the order of 12 Hz, while this high spike frequency regime exhibited a mean intra-burst spike frequency on the order of 24 Hz. Given the intermittent appearance of this regime with the low frequency regime, we hypothesized that the two regimes may coexist along the experimentally derived myomodulin comodulation curve. Experimental results (Tobin & Calabrese 2005) had shown that spike frequency increases under application of myomodulin by 10-30%, and we hypothesized this may be related to the coexistence or transition between these two regimes identified in the model.

At ($\bar{g}_h$, $I_{PumpMax}$) = (5.4,0.385), which corresponded to application of 10uM myomodulin, the HCO can produce the high spike frequency or the low spike frequency regime (Figure 4.1B) depending on the set of initial conditions. We compare this to the monostable point at parameter pair ($\bar{g}_h$, $I_{PumpMax}$) = (1.6, 0.429) which represented activity in control experiments. To test for multistability along the curve of comodulation, we performed continuous simulation along the line of comodulation (Methods). We noticed a shift into the high spike frequency at ($\bar{g}_h$, $I_{PumpMax}$) = (2.6,0.408). It remained in this high spike frequency regime until ($\bar{g}_h$, $I_{PumpMax}$)

= (5.6, 0.391), after which it switched back to the low frequency regime. We then spot checked 5 points in a range of parameter values along the comodulation line in which the cell had switched to the high spike frequency regime and simulated with those parameter pairs and initial conditions for the low spike frequency regime. All of these spot-checked simulations were able to maintain the low-frequency regime as well as the high frequency regime for at least 1600 seconds. In both regimes, we see a decrease in burst period and burst duration at very similar values as comodulation proceeds to higher $\bar{g}_h$ and lower, $I_{PumpMax}$ (Figure 4.1C & 4.1D). However, the high spike frequency regime decreases in spike frequency as comodulation proceeds, while the low spike frequency regime increases in spike frequency throughout the bistable region (Figure 4.1E). Along the curve of comodulation, there is a region of multistability between these points and in which the typical low spike frequency regime coexists with a high spike frequency regime.

While we expected continuity of regimes under continuous simulation along the line of comodulation, we did notice this switch instead at ($\bar{g}_h$, $I_{PumpMax}$) = (2.6,0.408). It is possible that the parameter step is too large to smoothly maintain the low spike frequency regime or that our equations are stiff enough that our integration fails to trace this regime. But, since both regimes are capable of stably bursting after nearly half an hour of simulated time (far longer than the system time constants), it is likely that we are in the steady state and that these regimes are in fact bistable.

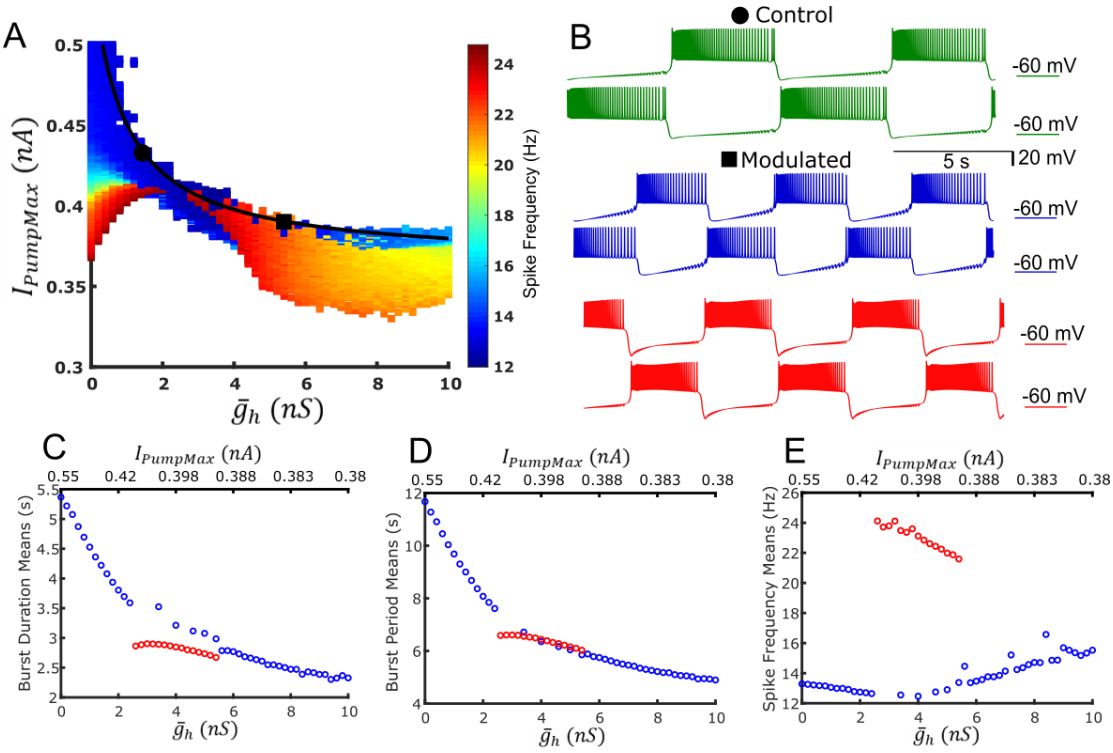

Figure 4.1. Model displays bistability of lower and higher spike frequency bursting regimes under comodulation.

(A) Map of intraburst spike frequency in the functional regime overlaid with the experimentally derived path of comodulation in black. (B) Previously identified canonical parameter pair for control bursting activity (black circle, green trace) was at a ($\bar{g}_h$, $I_{PumpMax}$) = (1.6,0.429). Two functional bursting regimes co-exist at the parameter coordinates ($\bar{g}_h$, $I_{PumpMax}$) = (5.4,0.385) corresponding to experimental point Myomodulin 10uM and could be observed when a numerical experiment is started with low spike frequency initial conditions (black square, blue trace) and high spike frequency initial conditions (black square, red trace). Burst duration (C), burst period (D), and spike frequency (E) from a continuous simulation along the path of comodulation. Red points represent the high spike frequency regime, and blue points represent the low spike frequency regime. Select points were simulated again using low spike frequency initial conditions and plotted in blue to confirm bistability.

4.4.2 Single Cell HN Model Under Modulation

Based on the prevalence of plateau potentials at low values of $I_{PumpMax}$, we hypothesized that mutually inhibitory interactions of the HCO may be preventing a depolarization block in at least some of the parameter regions of the functional HN HCO bursting regime. To test this idea, we performed a two-dimensional sweep of $I_{PumpMax}$ and $\bar{g}_h$ on the single cell HN model, investigating the same parameter domains as in our HCO experiment.

The most obvious difference between the HCO and the single cell models under this parameter variation was in the control of period. In the HCO system, the gradient of period was most closely associated with changes in $\bar{g}_h$. In the single cell, however, $I_{PumpMax}$ plays a much bigger role in regulation of the period (Figure 4.2A). At high levels of $I_{PumpMax}$, cycle period is around 8 seconds, and drops as low as 5 seconds as $I_{PumpMax}$ is reduced. At middling values of $I_{PumpMax}$ this trend abruptly reverses. Cycle period jumps to nearly 10 seconds, and increases to as much as 13.5 seconds as $I_{PumpMax}$ continues to be reduced. The parameter $\bar{g}_h$ appears to play a role in determining the level of $I_{PumpMax}$ which induce this switch. Using our previous methods for identifying plateau potentials in membrane activity (Ellingson et al. 2021, Ch. 3), we found that below this border at which the period trend reverses, 100% of membrane potential oscillations contain plateau potentials. Directly on this border, there is a small domain in which activity contains some plateau potentials, but also functional bursts (Figure 4.2B). At lower values of $\bar{g}_h$ there is a triangular region in which the depolarized phase duration drops as low as 5 seconds (Figure 4.2C), and spike frequency is elevated (Figure 4.2D).

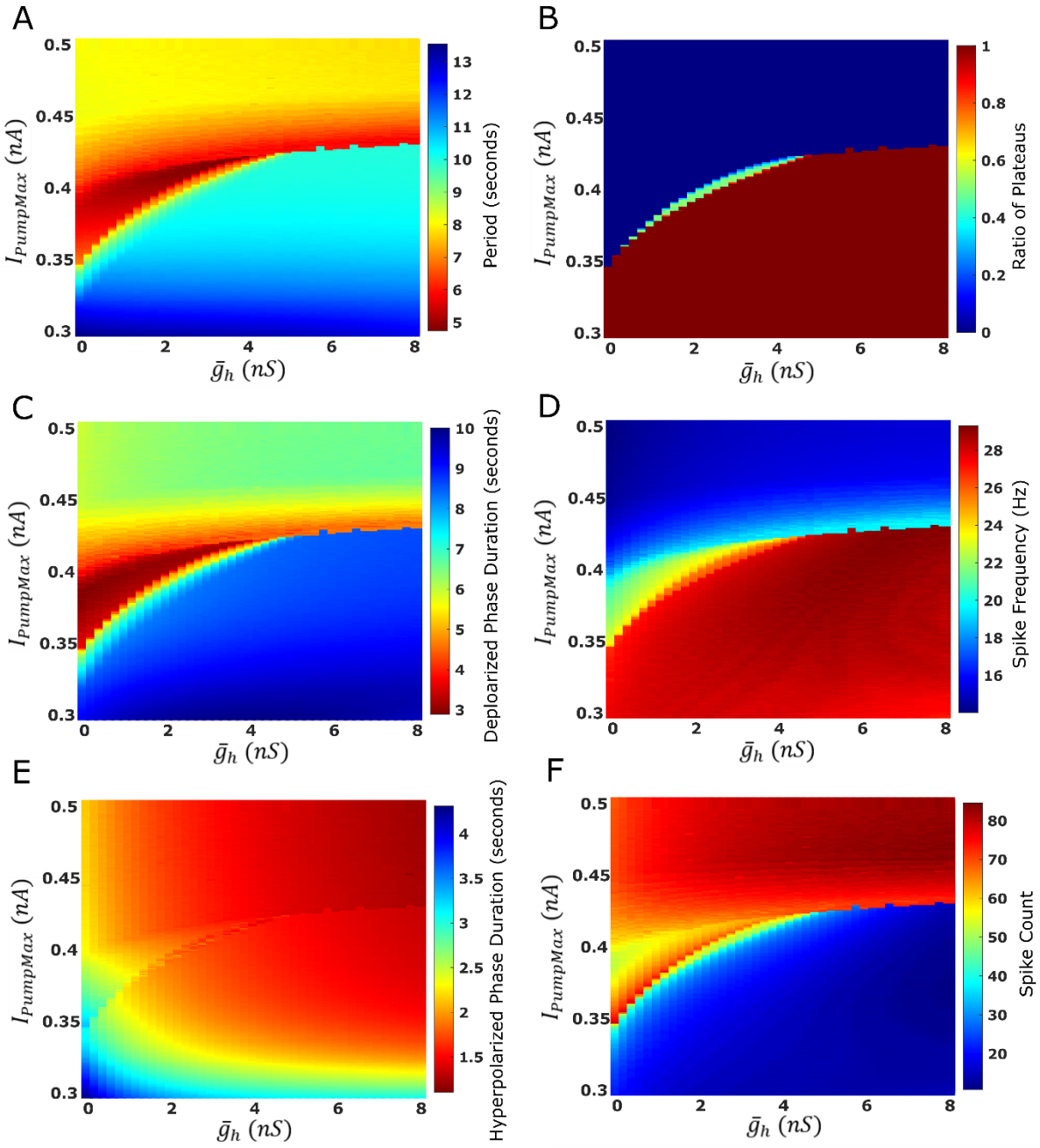

Figure 4.2 Maps of Temporal Characteristics of Single Cell Model Activity

(A) Average cycle period of single cell activity. Warmer colors indicate a lower period. Parameter $I_{PumpMax}$ has a much larger effect on period than $\bar{g}_h$. (B) Ratio of the total number of plateau phases to total number of all depolarized phases. There is a small region in which plateau-like oscillations and bursting activity mix. (C) Average duration of the depolarized phase of bursting. (D) Average spike frequency within the depolarized phase. (E) Average duration of the hyperpolarized phase of bursting. (F) Average number of spikes detected within the depolarized phase of bursting. Note that a low number of spikes at very high frequency is indicative of plateaus here.

4.4.3 Single Cell Displays several Regimes of activity

Based on the above bursting characteristics, we were able to categorize single cell activity into three types of regimes: low frequency bursting, high frequency bursting, and seizure-like plateau-containing activity (Figure 4.3). Between the regions of high frequency bursting and plateaus, we also identified a small domain of hybrid regimes consisting of high frequency bursting and plateaus. The high spike frequency regime is qualitatively very similar to the high spike frequency regime identified in the HCO model, in the same way that the low spike frequency regime is qualitatively similar to the low spike frequency regime in the HCO model.

By mapping the experimentally derived HN HCO comodulation path onto the corresponding parameter space of a single cell HN activities, we noticed that the transition from bursting to plateau-like oscillations occurs at ($\bar{g}_h$, $I_{PumpMax}$) = (2.6,0.408). Mutual synaptic inhibition, at middling to high level of $\bar{g}_h$ is sufficient to prevent this depolarization block, allowing for HCO functional activity in parameter spaces which would not be functional without the synaptic inhibition. The point at which the single cell transitions to seizure-like plateau-containing activity coincides with the beginning of the multistable domain in the HCO map. At the same level of modulation which transitions the single cell into plateaus, the HCO still maintains functional activity, and then also coexists with the high spike frequency regime. When $I_{PumpMax}$ is decreased in the single HN, the cell transitions to the high spike frequency bursting regime at low levels of $\bar{g}_h$. This regime is like a buffer between the low spike frequency and the dysfunctional regime, and it may serve the same purpose in the HCO.

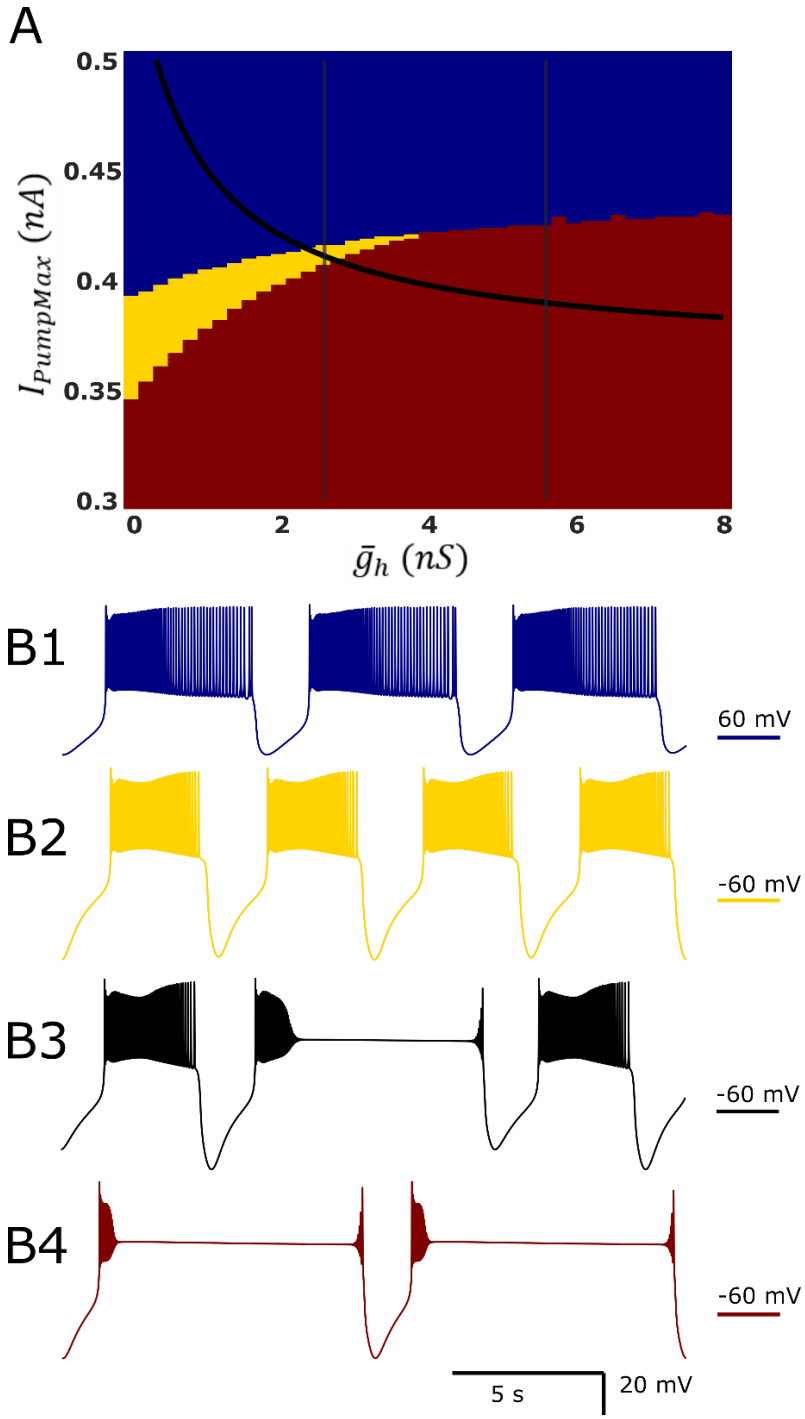

Figure 4.3 Regimes of Single Cell Activity

Map of activity regimes where red, blue, and yellow indicate plateau-containing oscillations, low-frequency bursting, and high-frequency bursting activities, respectively. Superimposed in black is the comodulation curve representing experimental data, and vertical black lines denote the bounds of the multistability domain identified in the HCO model along the comodulation curve. At control conditions, ($\bar{g}_h$, $I_{PumpMax}$) = (1.6,0.429), the model displays low frequency spiking (B1). Reduction in $I_{PumpMax}$ to ($\bar{g}_h$, $I_{PumpMax}$) = (1.6,0.4) results in high freqeuncy bursting (B2). There is a small region where high spike frequency and plateau regimes mix (B4) ($\bar{g}_h$, $I_{PumpMax}$) = (2.6,0.405). Entry into bistability in HCO coincides with entry into plateau-containing oscillations (B4) in the single cell ($\bar{g}_h$, $I_{PumpMax}$) = (5.4,0.385).

4.4.1 Description of Regimes

To investigate the roles of different currents in the underlying dynamics of large oscillations of the membrane potential which include bursts and plateaus, we applied a spike averaging algorithm to the depolarized phase of model voltage traces and currents (Figure 4.4). In this section, we compare trajectories and current contributions for these regimes of interest: HCO control, high spike frequency bursting of modulated HCO, and low spike frequency bursting of modulated HCO, Single cell control, plateau containing modulated Single cell, and high spike frequency depressed pump single cell.

A major difference in the behavior of low frequency regimes and the high frequency and plateau-containing regimes is that the Na^+ excursion is much higher in the high frequency and plateau-containing regimes. It is nearly twice as high in the high spike frequency regimes than low spike frequency regimes. This results in a higher pump current throughout the burst as well (Figure 4.4 & Figure 4.5). In low spike frequency regimes, the pump current rises and falls during the burst (Figure 4.4). In high spike frequency and plateau-containing regimes, the pump current rises through the depolarized phase and remains high until the minimum membrane potential is reached in the hyperpolarized phase. This suggests that pump current plays important role in the dynamics of burst termination in these regimes.

Since Na^+ has a major influence on the pump current, and is in turn affected by the pump current, we looked at the average contribution of currents and Na^+ flux during the depolarized and hyperpolarized phases of activity for all regimes of interest (Figure 4.5). Analysis of individual currents shows that I_{NaF} and I_P are the major drivers of depolarization and intracellular Na^+ concentration in all regimes of activity. The higher spike frequency in the high spike frequency regime, brings in much more Na^+ through I_{NaF} in the depolarized phase. Higher levels

of intracellular Na^+ increase pump current activation, so the pump is more active and contributes more heavily to the removal of Na^+. Another intriguing point here is that despite appearing at a lower $I_{PumpMax}$ value than the HCO control low frequency regime, the HCO high spike frequency regime in the bistable domain has a higher average pump current throughout the burst. A reduction in $I_{PumpMax}$ of 10% leads to an 8% increase in average pump current over the burst when the regime switches into the high spike frequency regime.

In the HCO high frequency regime, the majority of currents have a higher average current during both the depolarized and hyperpolarized phases. There are several major exceptions however. Persistent Na^+ current, I_P, contributes less charge during the hyperpolarized phase of the high-frequency regime than the low frequency regime. Leak current is an inward current on average during the hyperpolarized phase of the high-frequency regime, largely due to the massive afterhyperpolarization associated with this regime. Synaptic current, for the same reasons, appears to be smaller on average during the hyperpolarized phase of the high frequency regime. In the high frequency regime, the afterhyperpolarization is great enough to cross the reversal potentials for the leak and synaptic currents and is sufficient to reverse their contributions to the current balance on average.

In all regimes the pump current is the sole contributor to outward Na^+ flux. The major inward contributors of Na^+ during the depolarized phase are I_{NaF} and I_P, while the major inward drivers during the hyperpolarized phase are I_P, I_h, and I_{Leak}. What accounts for the major difference in Na^+ excursion between low and high spike frequency regimes is principally the I_{NaF} Na^+ entry driven by the higher spike frequency.

The low spike frequency regime is the only bursting regime observed at the HCO model value for control experiment ($\bar{g}_h$, $I_{PumpMax}$) =(1.6,0.429), and is a good reference point for

comparison with the two bistable regimes. The burst duration and bursting cycle period are much longer at control values, and so average current during the hyperpolarized and depolarized phases of activity are compared (Figure 4.5). It is clear that the average current and Na^+ contribution of all currents for control at a given point during the cycle is very similar to the low frequency regime. The high frequency regime is a “high-powered” version of the low frequency regime. It spikes much faster, and all currents have higher contributions.

The single cell under the same modulation, at which the bistability was recorded, produces the seizure-like plateau-containing oscillations. After some very fast initial I_{NaF} mediated spiking, I_{NaF} partially inactivates and the plateau is maintained by I_P and I_{CaS}. I_{CaS} slowly inactivates through the burst as I_{NaF} partially deinactivates and fires several spikes before the burst is terminated. Like in the high spike frequency regimes, pump current is highly active due to Na^+ influx mostly produced by I_{NaF} and I_P.

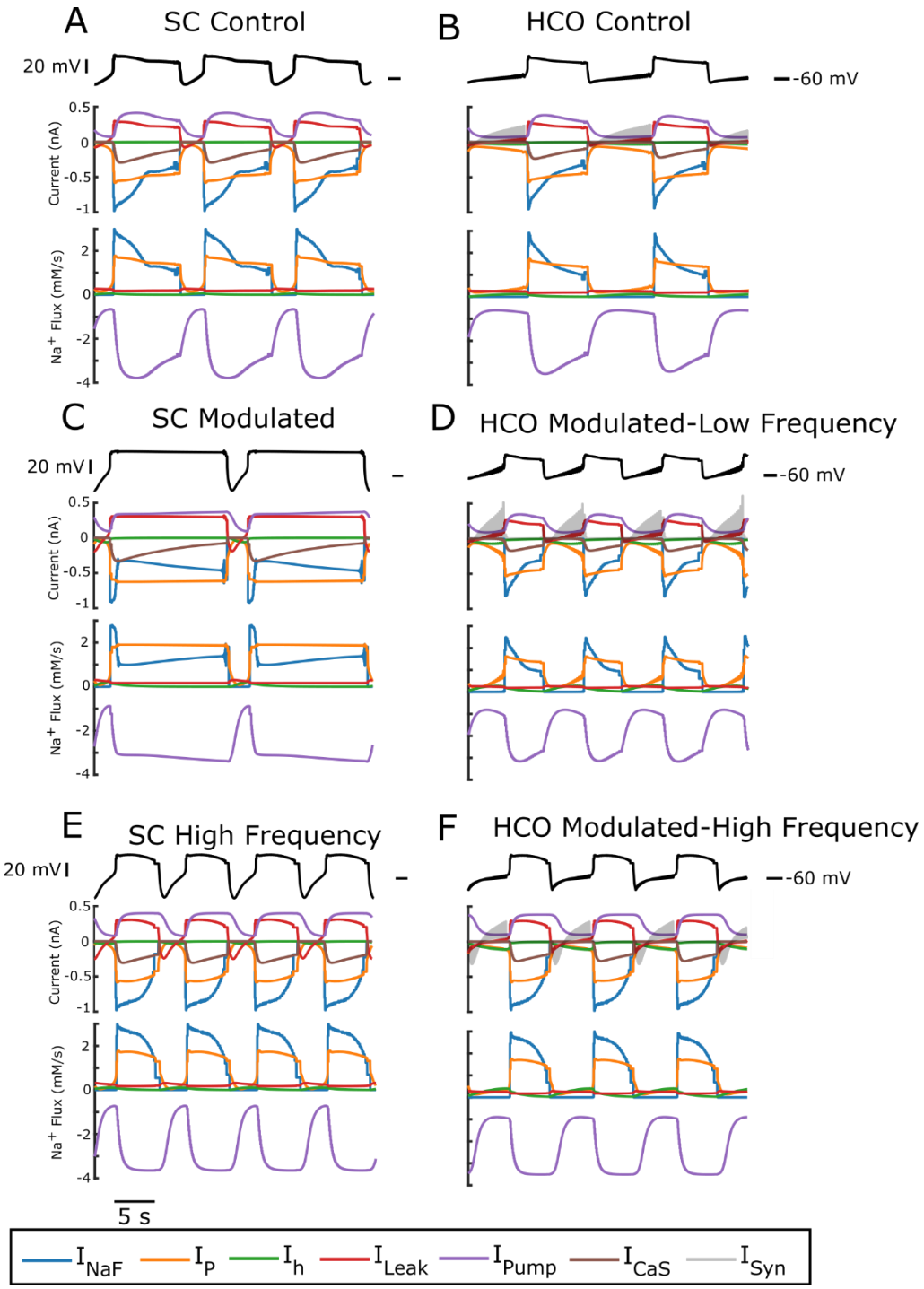

Figure 4.4 Spike-Averaged Current and Flux of Regimes of Interest

Current and flux time series of regimes of interest. All traces have been smoothed over spikes to provide a look at the oscillatory dynamics. Current and Na^+ Flux under control parameters ($\bar{g}_h$, $I_{PumpMax}$) = (1.6,0.429) for single cell (A) and HCO (B), both of which are low frequency bursting regimes. Current and Na^+ Flux under modulated parameters ($\bar{g}_h$, $I_{PumpMax}$) = (5.4,0.385) for single cell (C) which is a plateauing regime and HCO, which is bistable – capable of producing either a low spike frequency (D) regime or a high spike frequency regime (F). A reduction in $I_{PumpMax}$ from control values to 0.4 nA places the single cell in a high frequency regime (E) with qualitatively similar behavior to the HCO high spike frequency regime.

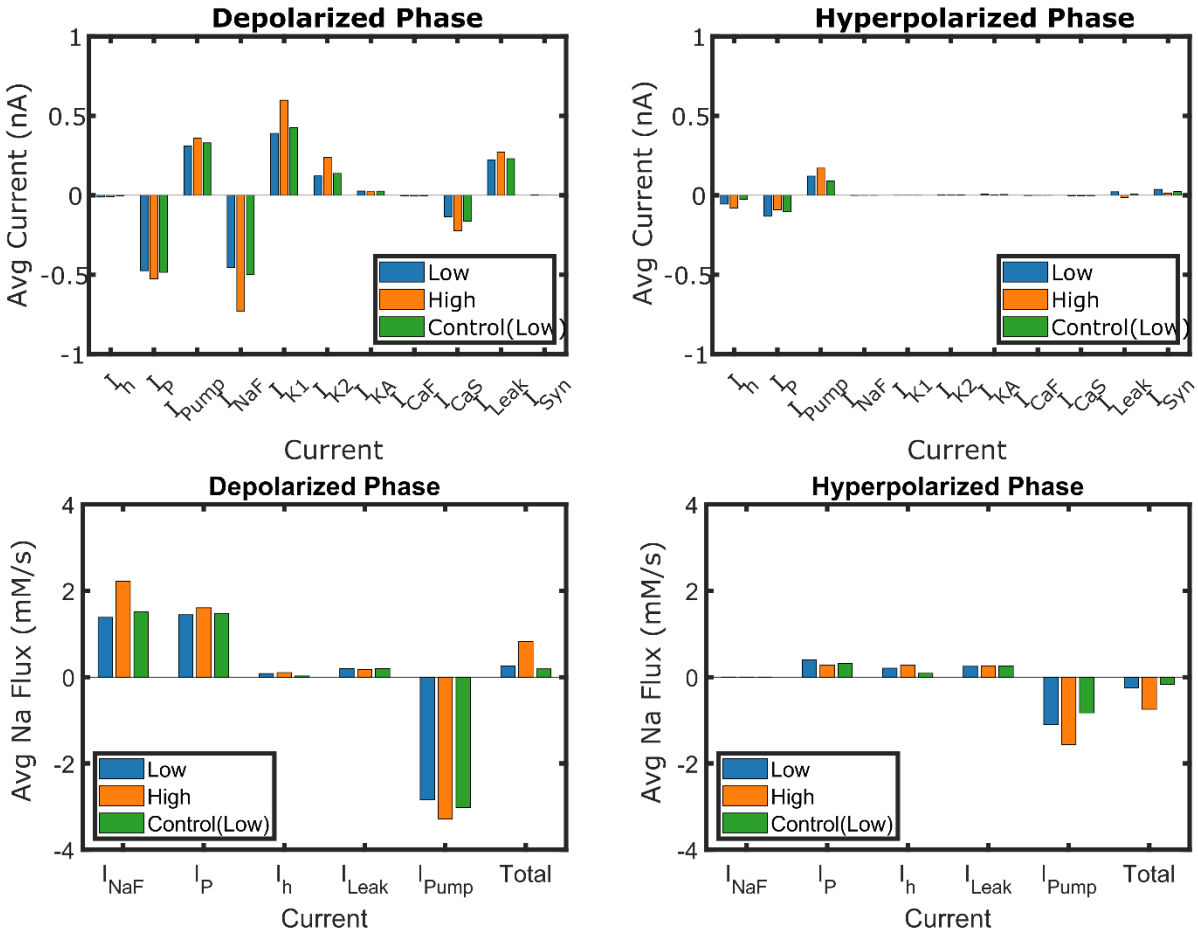

Figure 4.5 Current and Na^+ Contributions Over the Phases of Bursting Activity
Contributions of currents to bursting phases normalized to phase duration in select regimes in the HCO model. Average current for the monostable control (green) regime at ($\bar{g}_h$, $I_{PumpMax}$) = (1.6, 0.429), and the high (orange) and low (blue) spike frequency regimes at bistable point ($\bar{g}_h$, $I_{PumpMax}$) = (5.4,0.385) during the depolarized (A) and hyperpolarized phase (B). Average Na^+ flux for each Na^+ carrying current for the control (green) regime at ($\bar{g}_h$, $I_{PumpMax}$) = (1.6, 0.429), high (orange) and low (blue) spike frequency regimes at bistable point ($\bar{g}_h$, $I_{PumpMax}$) = (5.4,0.385) during the depolarized (C) and hyperpolarized phase (D).

4.5 Discussion

4.5.1 HCO Model Display Bistability of Low and High Frequency Regimes

In experiments with 1µM myomodulin, spike frequency increases between 10-30% (Tobin & Calabrese 2005). While the difference in the bistable regimes in the modulated HCO model is closer to 100%, the mere existence of these two regimes is interesting. They burst on the same time scale, but spike very differently.

4.5.2 Neuroprotective Effects of Synaptic Inhibition

A general lack of network inhibition is often implicated in seizure activity. The causes of this lack of inhibition are varied. Here we demonstrate a mechanism involving the inhibition of the Na^+/K^+ pump which can lead to seizure-like activity. Modulation of the single cell leads to this dysfunctional activity; modulation of the HCO leads to functional activity. Inhibition of the pump current ultimately leads to a depolarization block, but this can be compensated through the synaptic inhibition. Cells which always function with some level of inhibition are tuned to be accustomed to it, and this is one mechanism, among many, which can explain aberrant activity when inhibition is removed. Where one cell is incapable of bursting in a biological parameter range, a network of cells can robustly produce proper activity.

4.5.3 Downregulation of a Current can Counterintuitively Result in a Larger Current

Another point from this computational study comes from the realization that a cell with a lower maximal pump current displayed a larger overall pump current. This means that using an incomplete pharmacological inhibitor does not guarantee any reduction in the current. It entirely depends on the dynamics of the other channels involved, which is often unknown in pharmacological experiments on neural circuits. We should therefore be cautious in our interpretations. This understanding should be applied to any other system in which the pump is modified. Downregulation or partial blocking of the pump does not guarantee that there will be less pump current. In fact, under certain conditions, it can increase the average pump current.

5 THE PLASMA MEMBRANE CALCIUM ATPASE PUMP IN THE REGULATION OF INTESTINAL MOTOR PATTERNS (PAPER)

5.1 Abstract

Gastrointestinal motility is based on the rhythmic activity of interstitial cells of Cajal (ICCs). The ICC rhythm generation relies upon characteristic Ca^{2+}-handling mechanisms that involve voltage-gated Ca^{2+} channels, pumps and exchangers located in the plasma membrane, endoplasmic reticulum (ER), and mitochondria. Mutations, overexpression, and genetic knockdowns of the plasma membrane calcium ATPase (PMCA) pumps have been shown to disrupt calcium signaling and to cause disorders in other cell systems. Using an ICC biophysical model, we investigated the effects of PMCA pump upregulation in ICC rhythm generation. We found that, depending on the PMCA maximum pumping rate, the ICC model generates voltage and Ca^{2+} oscillations with different characteristics or becomes silent. The model predicts the coexistence of activity regimes near a canonical set of the parameters. One of these regimes is a silent regime that would indicate gastric dysmotility.

5.2 Introduction

Interstitial cells of Cajal (ICCs) in the gastrointestinal (GI) tract generate rhythms that underlie normal GI motility patterns, including the peristaltic motor pattern (Huizinga & Lammers 2009, van Helden et al. 2010, Sanders et al. 2014). The ICC rhythmic activity incorporates intrinsic spontaneous oscillations in the plasma membrane potential (V_m) and cytosolic Ca^{2+} concentration ($[Ca^{2+}]_i$). This rhythm requires robust intracellular calcium handling mechanisms, including Ca^{2+} extrusion by the ATPase pumps and exchangers (Ward et al. 2000, Blair et al. 2014). The key subsystem driving spontaneous $[Ca^{2+}]_i$ oscillations is incorporated by Corrias and Buist (Corrias & Buist 2008) as an intracellular pacemaker unit

comprising of three intracellular compartments: (i) endoplasmic reticulum, ER, (ii) mitochondria, and (iii) the nanodomain of the pacemaker unit (PU) which is the intracellular space between the above compartments and plasmalemma. The state of the pacemaker unit is described by the corresponding intra-compartmental calcium concentrations $[Ca^{2+}]_{ER}$, $[Ca^{2+}]_m$, and $[Ca^{2+}]_{PU}$, respectively. Diffusion between the PU and the intracellular bulk space causes changes in the Ca^{2+} concentration in the latter, $[Ca^{2+}]_i$. Under normal canonical conditions [6], the pacemaker unit generates oscillations of the intracompartmental Ca^{2+} concentrations, which lead to oscillations with an about 20-sec period in the bulk $[Ca^{2+}]_i$ and V_m. The plasma membrane Ca^{2+}-ATPase (PMCA) is critical for the regulation of cellular homeostasis and for maintaining rhythmic activity. The PMCA pumps extrude Ca^{2+} out of the cell against its concentration gradient to keep the intracellular Ca^{2+} concentration low and to bring $[Ca^{2+}]_i$ back to the baseline level after signaling events (Strehler & Treiman 2004). This regulation is necessary for normal cell functioning, as a reduced PMCA activity can lead to cytotoxic calcium overload and cell death (Bruce 2018). It has been shown that mutations related to particular PMCA isoforms result in pathological states and even mortality (Strehler 2013). Also, the PMCA pump plays a special role in the ICC rhythm generation, since it interconnects the electrical and calcium dynamics. However, the effect of PMCA upregulation on the ICC slow-wave activity is unknown. To investigate the effects of the PMCA pump on the activity of ICCs, we used the Corrias-Buist model (Corrias & Buist 2008) describing oscillations in the membrane potential and intracellular calcium in these cells.

5.3 Methods

5.3.1 Model

There are several models of ICCs currently in the literature (Corrias & Buist 2008, Youm et al. 2006, Faville et al. 2008, Lees-Green et al. 2014), each uniquely suited for answering certain particular questions about cellular functioning and rhythm generation (Lees-Green et al. 2011). We selected the murine gastric ICC model developed by Corrias and Buist as the foundation for our investigation due to the detailed representation of the metabolic calcium dynamics and compartmental calcium handling in this model. Such ICC model is a biophysical one, including the Hodgkin–Huxley style representation of the membrane currents and intracellular calcium dynamics (Magnus & Keizer 1997, Fall & Keizer 2001). This has been provided by the authors in the form of the MATLAB code at www.bioeng.nus.edu.sg/compbiolab/. A graphical representation of the model compartments and membrane currents is presented in Fig. 5.1.

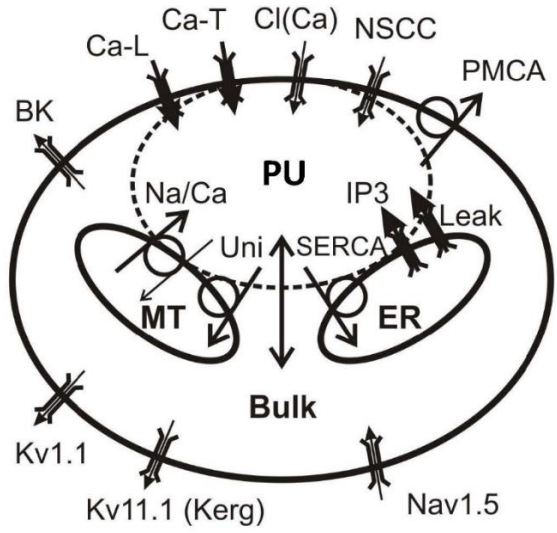

Figure 5.1. Model ICC Schematic
Diagram describing the calcium and electrical dynamics of the model interstitial cell of Cajal (ICC). Pictured are subcellular calcium compartments, including the bulk cytosolic compartment (Bulk), endoplasmic reticulum (ER), mitochondria (MT), and the nanodomain of the pacemaker unit (PU). Ca^{2+} fluxes are represented by large thick arrows, while smaller arrows represent other ion fluxes. Membrane ion channels are labeled by symbol "][." Calcium handling pumps are represented by circles.

Membrane channels include L-type Ca^{2+} channels, T-type Ca^{2+} channels, TTX resistant Na^{+} channels of the Nav1.5 type, voltage dependent K^{+} channels of the Kv1.1 and ether-ago-go (ERG) types, Ca^{2+}- and voltage-dependent K^{+} channels of the BK type, Ca^{2+}-gated Cl– channels, nonselective cation current channels (NSCCs), leak K^{+} channels, and PMCA pumps. Calcium concentrations are computed over four intracellular compartments, including the bulk cytoplasm, mitochondria, ER, and a nanodomain between the mitochondria and ER. Oscillations of the calcium concentration occur naturally between these three compartments in isolation from the rest of the cell systems. Calcium fluxes between the ER and the nanodomain are due to the SERCA pump, IP3- gated calcium release, and calcium leak channels on the ER. Fluxes between the mitochondria and the nanodomain are carried by the Na^{+}/Ca^{2+} exchanger and the Ca^{2+} uniporter. The nanodomain provides a diffusive flux path to the bulk cytoplasm, and T-type and L-type calcium channels also contribute to calcium levels in the bulk cytoplasm. While most Ca^{2+}-gated membrane channels are gated by bulk cytoplasmic calcium, the NSCCs are gated by the nanodomain calcium level. We made one change in the published model; the environmental variables Environment_RToF and Environment_FoRT were computed using Environment_T_exp instead of Environment_T, so that time constants of calcium, sodium, and potassium current activations would be calculated at the apparent (experimental) model temperature instead of the reference temperature.

5.3.2 Parameter Sweeps

In order to investigate the effects of an overexpressed or hyperactive PMCA pump, we swept values of the parameter $J_{PMCAMax}$ in small steps within the range from its canonical value of 0.088464 to 0.15924 mM/sec (180% of its canonical value). Simulations of the model activity

were carried out with the backward differentiation formula method using a variable step, the variable order solver (function ode15s in the MATLAB software from MathWorks). Absolute and relative tolerances were 10–9 and 10–8, respectively. The initial and maximum time steps were 0.01 and 0.5 sec, respectively. Initial conditions for the model with the canonical value of $J_{PMCAMax}$ were taken from Corrias & Buist (2008), and initial conditions within a parameter sweep for other values of $J_{PMCAMax}$ were taken from the endpoint of the preceding simulation. Each simulation was integrated over 85,000 sec to ensure the system had reached its steady state before we conducted data analysis. The canonical slow-wave regime was traced to identify the critical value of $J_{PMCAMax}$ at which this regime is destabilizes. Once this destabilization point was found, the silent regime was traced along both increasing and decreasing $J_{PMCAMax}$ values, to establish its range of stability, the range of coexistence of the oscillatory and silent regimes, and the presence of hysteresis.

5.3.3 Perturbations

We explored the coexistence of the oscillatory and silent ICC activity regimes by testing whether some simple perturbation would switch the activity of the system from one regime to the other. To investigate the switch from silence to oscillations, the model was integrated for 200 sec in the resting state. The endpoint of the obtained trajectory was used as the initial point for the following perturbation experiments; one by one, a single-state variable was perturbed instantaneously from its resting value to its respective maximal value for the oscillatory state. This procedure was applied to each state variable. To investigate the switch from oscillations to silence, the phase of oscillations was defined to keep the stimulation consistent. Phases of 0 or 1 corresponded to the trough of voltage oscillations. After integrating for 200 sec in the oscillatory state, a single-state variable was perturbed instantaneously at the time corresponding to the

lowest point in voltage oscillations (phase = 0) to its respective resting value for the silent state. This procedure was applied to each state variable.

5.3.4 Analysis

Analysis of the model trajectories was performed by custom MATLAB scripts that detect peaks and troughs and compute the period and amplitude of oscillations for all state variables. The analysis was performed on the last 25,000 sec of the simulations, to exclude transient effects induced by the change in $J_{PMCAMax}$ between the latter. Peaks and troughs were defined by peak prominence. Only extrema that were at least half as large as the full oscillation were considered, thus eliminating local extrema. The plateau length of oscillatory activity was determined by the full width at a half-maximum value, defined as the time interval in a single period where oscillations spent above half of the maximum value of the trace. The duty cycle of oscillations was computed as the ratio of the full width at half maximum with respect to the period. When the coefficient of variation of individual state variables over an entire simulation was less than 0.001, the traces were examined manually and confirmed to be silent.

5.4 Results

We varied the parameter $J_{PMCAMax}$ upwards from its canonical value of 0.088464 mM/sec and report examples of oscillatory activity (Fig. 5.2 C1 and C2a) and silent activity (Fig. 5.2 C2b and C3). We first reproduced the activity under normal conditions (Fig. 5.2 C1), as reported by Corrias and Buist; at a $J_{PMCAMax}$ value of 0.088464 mM/sec, the simulated gastric ICC displays oscillations in the membrane potential V_m, cytosolic calcium concentration $[Ca^{2+}]_i$, PU subspace calcium concentration $[Ca^{2+}]_{PU}$, ER calcium concentration $[Ca^{2+}]_{ER}$, and mitochondrial calcium concentration $[Ca^{2+}]_m$. These gastric electrical slow waves, as they are referred to in the GI literature, are characterized by a sharp increase in the membrane potential from the basal level

near –60 mV to roughly –25 mV. This rapid depolarization is followed by a plateau depolarization phase of roughly 10.4 sec, and, finally, by a return to the basal level. Imaging studies (Torihashi et al. 2002) also showed that intracellular calcium levels oscillate with the membrane potential in a synchronized fashion, which we also observe in the simulated ICC model. Under physiological conditions, the normal period of oscillations for murine gastric ICCs is roughly 20 sec (Hirst & Edwards 2001), and the model indeed reproduces this activity.

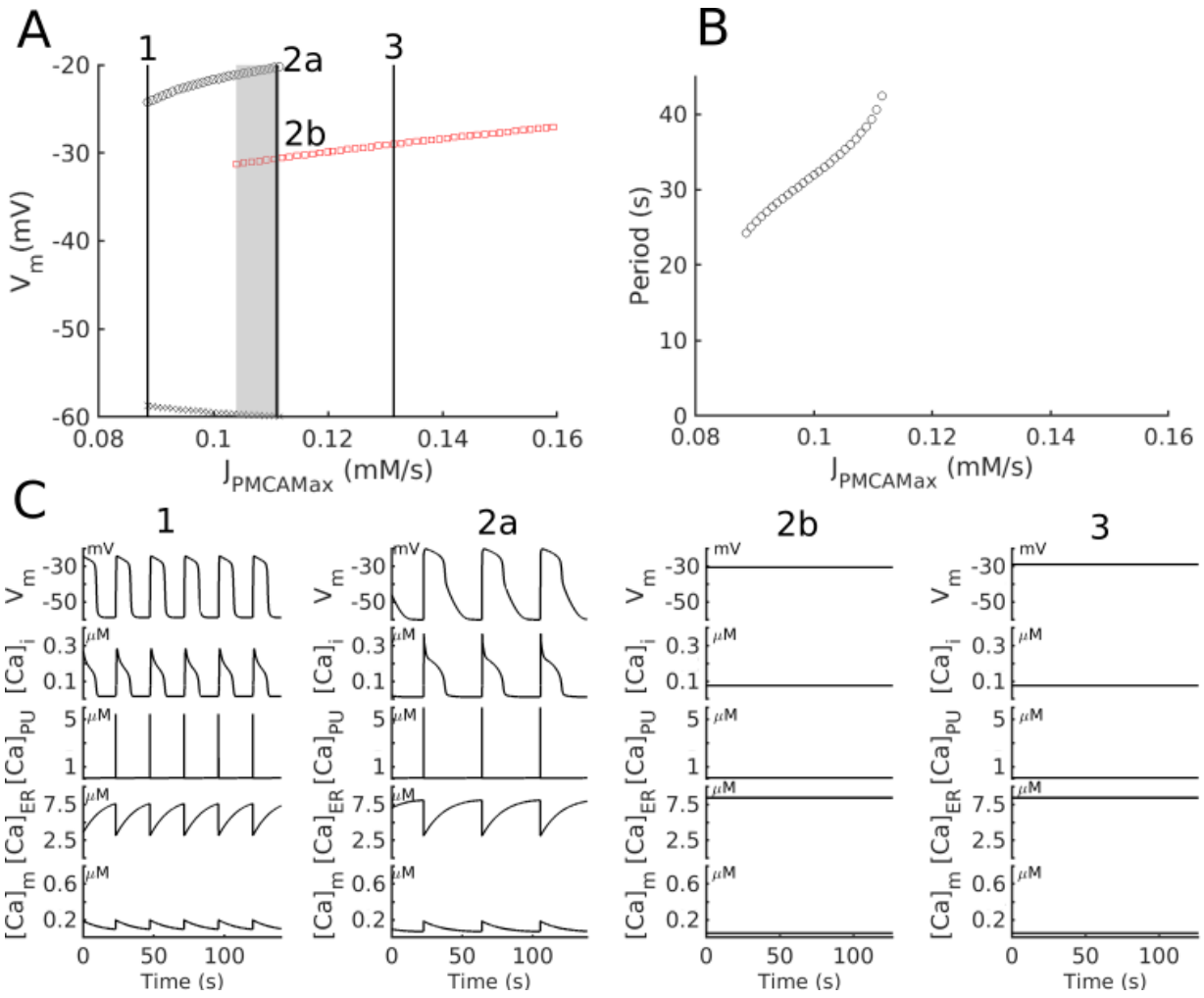

Figure 5.2. Regimes of ICC activity under variation of $J_{PMCAMax}$

Diagram of the observed regimes of ICC activity under variation of $J_{PMCAMax}$ with the respective examples. A) Minima and maxima ('x' and 'o' markers, respectively) of the model cell membrane potential Vm in the slow-wave oscillatory and silent regimes are shown in black and red, respectively. Note the presence of two stable regimes (one oscillatory and one silent) between $J_{PMCAMax}$ values of 0.10395 and 0.11146 mM/sec. This indicates a multistable regime, which is shaded gray. Marked on this diagram along the vertical lines, are values of $J_{PMCAMax}$ for which examples of model cell activity are shown in C. B) Period of the oscillatory regime increases monotonically as

$J_{PMCAMax}$ increases. C) Examples of activity regimes represented by the membrane potential V_m, cytosolic calcium concentration $[Ca^{2+}]_i$, PU calcium concentration $[Ca^{2+}]_{PU}$, ER calcium concentration $[Ca^{2+}]_{ER}$, and mitochondrial calcium concentration $[Ca^{2+}]_m$ during regimes of interest taken at the parameter values 1, 2, and 3 in A. During canonical slow-wave activity (C 1) at $J_{PMCAMax}$ = 0.088464 mM/sec, all oscillatory subunits are functioning, as reported by Corrias and Buist. Initial conditions for this oscillatory state are similar to those reported by Corrias and Buist. Under conditions with a hyperactive or overexpressed PMCA pump (C 2) at $J_{PMCAMax}$ = 0.11102 mM/sec, the plateau phase of the oscillations and the period of oscillations are roughly 150% longer. There is a region of multistability between $J_{PMCAMax}$ = 0.10395 and 0.11146 mM/sec, in which the system can either exhibit slow-wave oscillations (C 2a) or stay silent at a stationary state (C2b). Initial conditions for the oscillatory state (C2a) are: $[Ca^{2+}]_i$ = 0.0000129875409 mM, V_m = –59.6651372402174 mV, $[ADP]_i$ = 0.0097670595318 mM, $[ADP]_m$ = 3.1260344843214 mM, $[Ca^{2+}]_{ER}$ = 0.0079609300970 mM, $[Ca^{2+}]_{PU}$ = 0.0000834617367 mM, $[Ca^{2+}]_m$ = 0.0000735791887 mM, $[NADH]_m$ = 0.1723644531127 mM, $\Delta\Psi$ = 156.723427551462 mV, h_{IP3} = 0.9440537811959, act_{CaCl} = 0.0007980061937, d_{ERG} = 0.2000000002153, d_{CaL} = 0.0000490771360, d_{NSCC} = 0.0000783670067, d_{Nav15} = 0.0667086138234, d_{VDDR} = 0.0036454956259, d_{Kv11} = 0.0109667137286, f_{CaL} = 0.8664424404802, f_{Nav15} = 0.0679044155244, f_{VDDR} = 0.2577845709159, f_{CaCaL} = 0.9999999998951, and f_{Kv11} = 0.9835090903364. Initial conditions for the rest state (C2b) are: $[Ca^{2+}]_i$ = 0.0000762752373 mM, V_m = –30.6371763049647 mV, $[ADP]_i$ = 0.0113983213327 mM, $[ADP]_m$ = 3.4350418943225 mM, $[Ca^{2+}]_{ER}$ = 0.0084319806602 mM, $[Ca^{2+}]_{PU}$ = 0.0000762752352 mM, $[Ca^{2+}]_m$ = 0.0000504414376 mM, $[NADH]_m$ = 0.1337679766097 mM, $\Delta\Psi$ = 155.7138137416999 mV, h_{IP3} = 0.9483326460056, act_{CaCl} = 0.1392081718700, d_{ERG} = 0.2021648684174, d_{CaL} = 0.0402548861996, d_{NSCC} = 0.1190265393462, d_{Nav15} = 0.9679821969815, d_{VDDR} = 0.3158601685749, d_{Kv11} = 0.3247338865928, f_{CaL} = 0.1995544603291, f_{Nav15} = 0.0011508330972, f_{VDDR} = 0.0027488940047, f_{CaCaL} = 0.9999999868511, and f_{Kv11} = 0.5192317355598. At a much higher value of $J_{PMCAMax}$ = 0.13137 mM/sec (C3), all oscillatory subunits are silent.

5.4.1 PMCA Regulation

First, we varied a single parameter $J_{PMCAMax}$ to investigate how characteristics of the slow-wave rhythm depend on the level of PMCA activity. An increase in $J_{PMCAMax}$ from the canonical value slows down the period of oscillations (Fig. 5.2 B) from 20.0 to 42.4 sec at a $J_{PMCAMax}$ of 0.11146 mM/sec. As $J_{PMCAMax}$ is increased, the plateau phases of oscillations become markedly longer, changing from 10.4 sec at the canonical value $J_{PMCAMax}$ up to 16.5 sec, and the amplitudes of both membrane potential and calcium concentration oscillations grow. The duty cycle undergoes minor changes as $J_{PMCAMax}$ increases: it decreases from 0.43 to 0.37 as $J_{PMCAMax}$ grows from 0.088464 to 0.1 mM/sec, and then it grows to 0.39 as $J_{PMCAMax}$ reaches 0.11146 mM/sec. These changes demonstrate how upregulation of PMCA pumps can control characteristics of the rhythm generation in ICCs. Examples of cell activity at several values of $J_{PMCAMax}$ are presented in Fig. 5.2C. At the critical value of $J_{PMCAMax}$ 0.11146 mM/sec (an increase by 25% over the canonical value), the slow wave oscillations are destabilized, and the

system transitions to the silent stationary state (shown in red in Figs. 5.2 and 5.3). In this regime, the cell activity was stable and unchanging in a depolarized state with low levels of bulk cytosolic calcium, but high levels of calcium were sequestered in the ER. Increasing $J_{PMCAMax}$ in the silent regime exerted no apparent effect on the resting calcium levels in the four compartments, but the resting membrane potential increased slightly, from –30.5 mV at a $J_{PMCAMax}$ of 0.1119 mM/sec to –27 mV at a $J_{PMCAMax}$ of 0.15924 mM/sec. Constant depletion of cytosolic calcium through the upregulated or hyperactive PMCA pumps disrupts the diffusive force driving calcium flux between the cytosol and the PU, destabilizing the subcellular oscillator. Physiologically, this silent regime represents a contracted state, which would cause delayed gastric motility or blockage. Notably, in the case of the silent regime at high levels of $J_{PMCAMax}$, the system takes a very long time to attain the resting state (>200,000 sec). After an initial integration time of 60,000 sec, all state variables are monotonic, and the coefficient of variation over the next 25,000 sec is less than 0.0001%, indicating that the system reached its resting state.

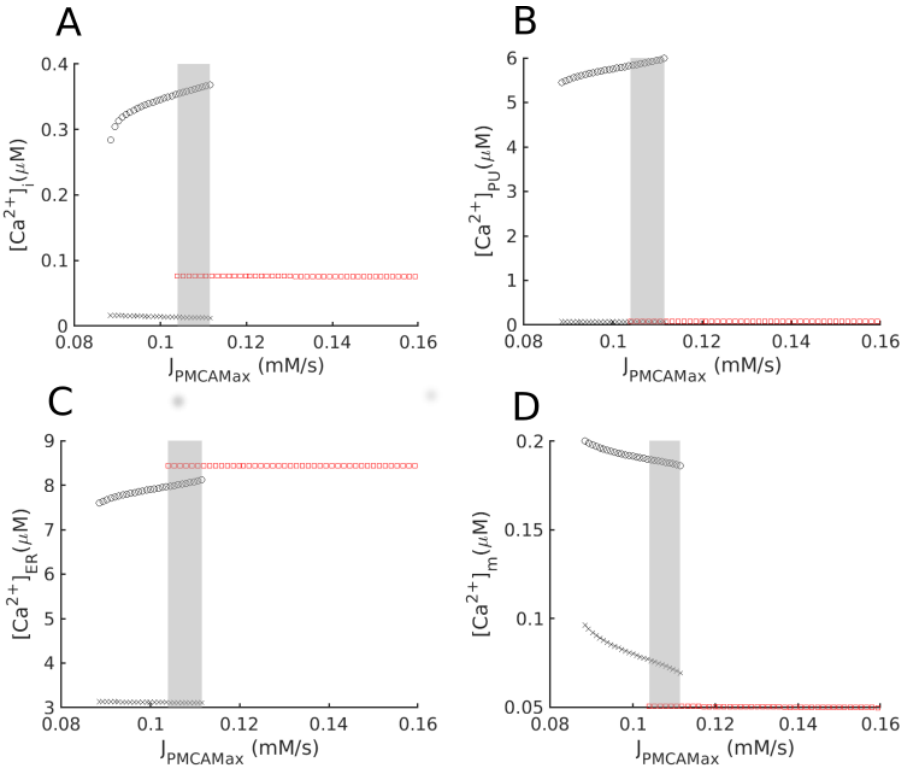

Figure 5.3. Cellular Ca^{2+} under variation of $J_{PMCAMax}$
Diagrams of the observed regimes of activity of calcium subcompartments under $J_{PMCAMax}$ variation. Minima and maxima ('x' and 'o' markers, respectively) of oscillations of the cytosolic calcium concentration $[Ca^{2+}]_i$, PU calcium concentration $[Ca^{2+}]_{PU}$, ER calcium concentration $[Ca^{2+}]_{ER}$, and mitochondrial calcium concentration $[Ca^{2+}]_m$ are shown. The silent regime is plotted in red, the oscillatory regime is plotted in black, and the domain of co-existence of these regimes is shaded gray.

5.4.2 Multistability

After tracing the silent regime along increasing values of $J_{PMCAMax}$, we traced it back along decreasing values of $J_{PMCAMax}$ to determine whether there were hysteresis effects. We found that this silent regime destabilized at the critical value of $J_{PMCAMax}$ of 0.10395 mM/sec. Thus, the system exhibits multistability of canonical slow waves and resting state for values of $J_{PMCAMax}$ between 0.10395 and 0.11146 mM/sec (shown in gray on Figs. 5.2 and 5.3). This range of coexistence covers 32.6% of the considered range of the stable oscillatory regime. An increase in the total PMCA activity level by only 17% of the canonical value places the cell in this bistable state. This result suggests that ICCs could operate in a multistable regime under normal physiological conditions. Figure 5.2 shows examples of cell activity at several values of

$J_{PMCAMax}$, including examples of the oscillatory (Fig. 5.2 C2a) and the silent regime (Fig. 5.2 C2b), which coexist at $J_{PMCAMax}$ of 0.11102 mM/s. To verify the coexistence of these regimes of activity, we attempted to perturb both regimes, to determine if it was possible to provide a transition between them, and, if so, which state variables could induce such a switch. We found that the system could be switched either from a silent regime to oscillations or vice versa (Fig. 5.4) by perturbing the mitochondrial calcium concentration as described in Methods. Perturbations of this type applied to any other state variable were not capable of switching between regimes, suggesting a particularly important role of the mitochondria in the rhythm generation by ICCs.

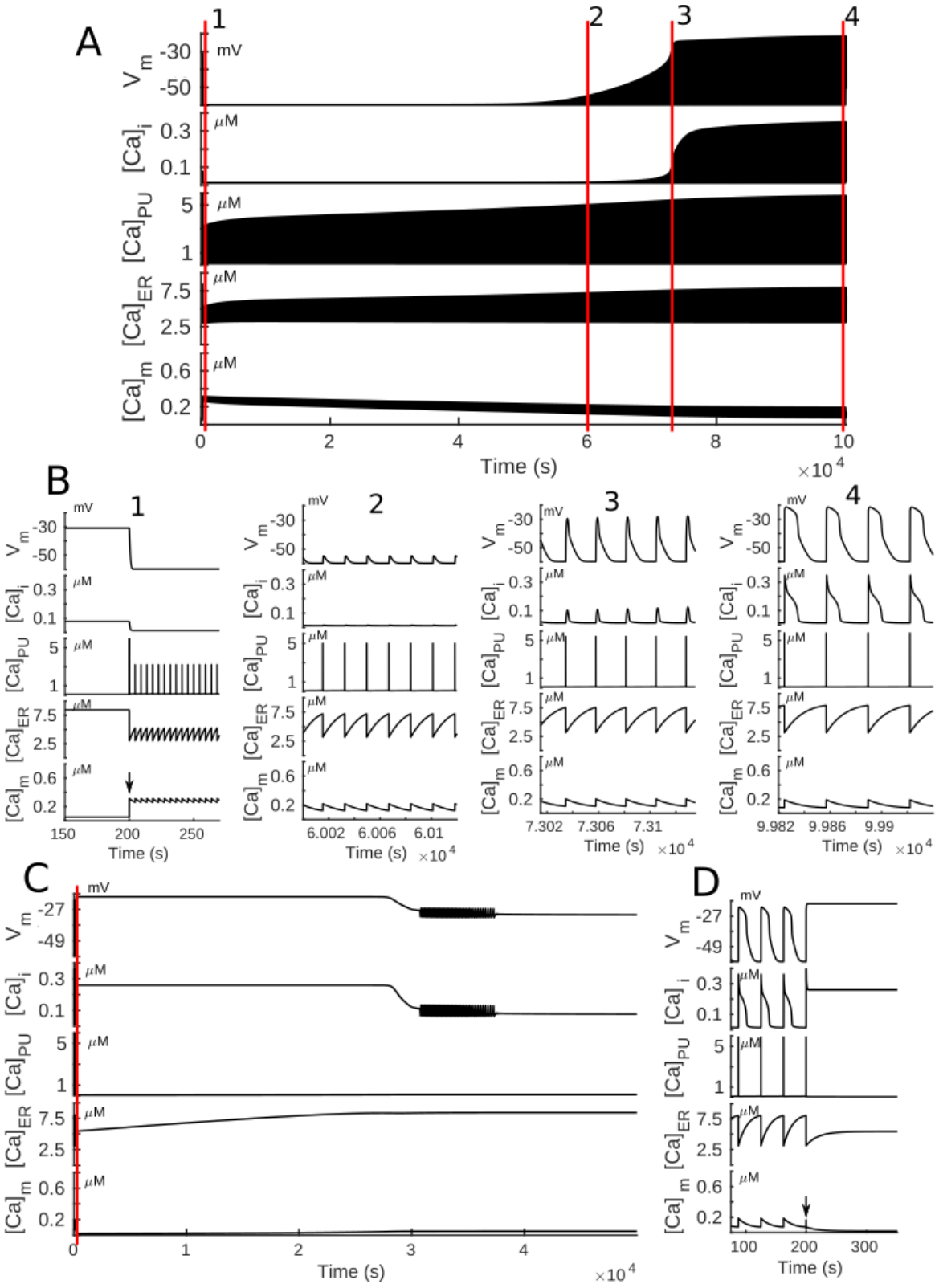

Figure 5.4. Perturbations in mitochondrial Ca^{2+} can switch the regime of activity
Perturbations in the calcium concentration $[Ca^{2+}]_m$ can switch the cell activity between the silent regime and the regime of slow wave oscillations, while the model is in the domain of multistability. Here, at $J_{PMCAMax}$ = 0.10793

mM/sec, perturbations of the mitochondrial calcium concentration $[Ca^{2+}]_m$ induced a transition of the cell activity from silence to oscillations (A, B) and also from oscillations to silence (C, D). A) An example of a switch from the silent regime to the oscillatory regime: membrane potential V_m, cytosolic calcium concentration $[Ca^{2+}]_i$, PU subspace calcium concentration $[Ca^{2+}]_{PU}$, ER calcium concentration $[Ca^{2+}]_{ER}$, and mitochondrial calcium concentration $[Ca^{2+}]_m$ are shown after a perturbation of the mitochondrial calcium concentration $[Ca^{2+}]$m, while the cell was in the silent state. Red lines 1 to 4 correspond to plots in B, which demonstrate activity on a smaller time scale starting at the points indicated in the main trace (A). B1) At 200 sec, the mitochondrial calcium concentration $[Ca^{2+}]_m$ is perturbed from its resting state to its maximal value of steady oscillatory activity (perturbation marked with an arrow). At this point, the PU calcium concentration $[Ca^{2+}]_{PU}$ starts oscillating along with the mitochondrial and ER calcium concentrations. B2) Subcellular calcium oscillations continue to grow until PU calcium concentration ($[Ca^{2+}]_{PU}$) oscillations are large enough to activate the nonselective cation current, which begins driving oscillations of the membrane potential. B3) Oscillations of the membrane potential V_m and PU calcium concentration $[Ca^{2+}]_{PU}$ contribute to the bulk cytosolic calcium concentration $[Ca^{2+}]_i$ through the voltage-gated calcium channels and diffusion, respectively. Bulk cytosolic calcium concentration $[Ca^{2+}]_i$ continues to grow, until in (B4) the system reaches the steady oscillatory state. The oscillation period is not completely stabilized until 100,000 sec. C) An example of a switch from the oscillatory regime to the silent regime: Mitochondrial calcium concentration $[Ca^{2+}]_m$ is perturbed at the moment of time when the membrane potential is at the lowest point of the oscillations (phase = 0) and set to its value ($[Ca^{2+}]_{m\_Rest}$) in the silent state. Membrane potential V_m and bulk cytosolic calcium concentration $[Ca^{2+}]_i$ then drop through an oscillatory transient activity before reaching their expected resting state values. D) On a smaller time scale, after the perturbation is applied at 200 sec (marked with an arrow), oscillations immediately stop, while the ER continues to sequester calcium monotonically until $[Ca^{2+}]_{ER}$ reaches its expected resting state value.

5.5 Discussion

We have used a biophysical model of an ICC to demonstrate that PMCA pump upregulation or overactivity under physiological or pathological conditions could disrupt the normal rhythm-generating mechanisms of ICCs, leading to a stable depolarized state, which represents halted gastric motility. We have shown that the PMCA pump can be used as a control target for modulating the temporal characteristics of ICCs, and that changes in the PMCA pump can lead to the development of multistability of the activity regimes. We have also demonstrated that acute changes in the mitochondrial calcium concentrations could switch the cell between two stable regimes. The PMCA pumps are crucial for cellular maintenance and also support signaling in a variety of cellular systems (Strehler & Treiman 2004). Different PMCA isoforms vary in their functions depending on the tissue and cell specificity. Mutations of PMCA2 cause deafness in both humans and mice, and mutations of PMCA3 cause cerebellar ataxia (Brini et al. 2013). In mice, homozygous PMCA1 isoform knockout is embryonic-lethal, suggesting a large housekeeping role; heterozygous PMCA1 knockouts have indicated a major role in bladder

contractility (Strehler 2013). In arterial smooth muscles in mice, overexpression of PMCA4 contributes to increased vascular tone and blood pressure (Gros et al. 2003). The PMCAs have been identified in all classes of ICCs (Cho & Daniel 2005). Given its importance in other calcium signaling systems, it is likely that the PMCAs play an important role in the calcium-dependent rhythm generation by ICCs as well. The PMCAs may also regulate the period of the slow-wave oscillations in individual ICCs. Along the small intestine, there is a frequency gradient for the slow-wave oscillations; the period of oscillations becomes longer as one measures it aborally, which favors a transit from the oral to the aboral direction (Diamant & Bortoff). While other subcellular or neural components could also modulate the period, we have shown here that activity levels of the PMCA pump effectively control the intrinsic oscillation period in ICCs. We suggest that differential PMCA pump expression or modulation levels in the small intestinal syncytium could be a critical factor in maintaining this frequency gradient. It has been proposed (Strehler 2013) that the PMCA pump could be a potential therapeutic target, given its described roles in several pathological conditions in the transgenic animal models. This study provides evidence that the PMCA pump could be targeted to address disorders of the GI rhythmicity. Given that the PMCA pump is ubiquitously expressed in eukaryotic cells (Strehler 2013), its activity may be crucial for the rhythm generation in other cells such as neurons of the central pattern generators. Biophysical modeling can be used to explore the role that the PMCA pump plays in the specific dynamics of calcium signaling and rhythm generation in other body systems. A novelty of our simulation study is the demonstration that the ICC oscillatory activity may stop when the PMCA maximum pumping rate exceeds a certain level (Fig. 5.2 C2b and C3). Depending on the rate increase, the non-oscillatory regime either coexisted with an oscillatory one (multistability) or became unique. This is a noteworthy extension of our earlier

work, where it was shown that ICC pacemaker activity is suppressed by a critical reduction of the PMCA maximum rate, presumably because of hypoxic depression of ATP production and PMCA deprivation of ATP-stored energy (Korogod et al. 2018). The hypoxic-ischemic condition in the GI tissue and ICCs residing therein may develop with reduction of splanchnic blood circulation and, consequently, impaired delivery of the oxygen required for the ATP production. The present study suggests that upregulation of the PMCA or increase in the maximum pump rate can also suppress ICC pacemaker activity. The PMCA pump can be dynamically modulated in vivo, e.g., by fatty acids; this increases ATP hydrolysis by the PMCA at low concentrations but decreases this activity at high concentrations (Oliveira et al. 2008). The PMCA activity is also affected by the dynamic structure and composition of the surrounding membrane phospholipids; neutral phospholipids support basal PMCA activity, while acidic phospholipids increase both the Ca^{2+} affinity and maximum pumping rate of the PMCA (Pignataro et al. 2015). It should be noted that: (i) the observed activity regimes were revealed by variation of the model parameters within a wide range; (ii) the nonoscillatory regimes occurred due to either decrease (earlier study (Korogod et al. 2018)) or increase (this study) in the PMCA rate relative to the reference value that corresponded to a preceding oscillatory regime, and (iii) for biological prototype ICCs, these reference values are not available. Therefore, we need to specify (patho)physiological conditions that may cause an increase in the PMCA activity and are also associated with impairment of ICCs and/or GI motility. In view of the above-mentioned relation between tissue oxygenation and energy supply of PMCA pumping, we suggest that one possible pathophysiological condition may result from postischemic reperfusion following laparoscopic GI surgery. In this case, the reference low (but sufficient for providing pacemaker oscillations) level of ICC PMCA activity is associated with reduced oxygen supply because of ischemic

reduction of blood perfusion. The latter occurs in addition to the systemic hemodynamic effect due to compression of the viscera by a gas insufflated into the abdominal cavity in order to enlarge the working area for laparoscopic surgery (Sammour et al. 2009, Hatipoglu et al. 2014). Correspondingly, deflation of the abdomen leads to reperfusion, which is known to produce a special kind of "reperfusion injury" (Sammour et al. 2009, Guan et al. 2009). In the previously ischemized tissues explored after the reperfusion and re-oxygenation, damages to GI cells, including ICCs, have been found (Guan et al. 2009, Shimojima et al. 2006). Another aspect of the ischemia reperfusion injury was associated with impairment of the GI motility (Shimojima et al. 2006, Bielefeldt & Conklin 1997). Such impairments were attributed mostly to an imbalance between oxidants (reactive oxygen species, ROSs), and antioxidants, i.e., the state qualified as oxidative stress (Sammour et al. 2009, Yilmaz et al. 2004). Our results highlight a potential contributor to ischemia-reperfusion injury, which was not earlier considered. This is impairment of the calcium handling mechanisms underlying the ICC pacemaker oscillatory activity, which could change its normal oscillatory regime for an abnormal silent regime with a re-oxygenation-related putative increase in the ICC PMCA activity. It is especially menacing if such silencing is associated with a long-lasting elevated intracellular Ca^{2+} concentration that, due to its cytotoxicity, can kill the ICCs and, thus, disrupt the driver of GI motility.

6 CONCLUSIONS

Central pattern generators (CPGs) are networks of neurons which drive rhythmic behaviors like locomotion, heartbeat (in invertebrates), and breathing. At the heart of some CPGs are networks of cells which have endogenous electrical oscillations for pacing the rest of the pattern organizing circuit. CPGs must continually adjust their patterns of activity to a accommodate a highly variable environment and the dynamic behavioral goals of an animal. Neuromodulation adjusts these patterns by orchestrating changes in multiple ionic currents. Under neuromodulation, the roles of different currents in the bursting process change. Neuromodulation can push a dynamical system to the edges of its ability to produce functional rhythms, and at these edges lurk dangers such as silent states or multistability of pathological states. It is at these edges where robust mechanisms for regulation are found, simply because these are the conditions in which they are necessary for survival. Those places where complex control systems are pushed to their limit without breaking down give an evolutionary edge to organisms which can manage them. Neuromodulation can be an effective tool for changing and scaling the activity of CPGs and other rhythmic systems, and the use of multiple modulators with multiple targets increases the complexity of what could be designed to be a simple system. These complexities, however, also allow the systems to have a much greater range of situational control options.

The role that ATPase pumps can play in the regulation of rhythmic activity is poorly understood. To contribute to this active field of research, I have taken a biophysical modeling approach to investigate a mechanism for regulating rhythmic behavior in ICCs and a mechanism of comodulation in the leech heartbeat central pattern generator. Both mechanisms are heavily dependent on the behavior and kinetics of an ATPase pump, which can be modulation targets.

In the leech heartbeat HCO, the electrogenic Na^+/K^+ pump and the hyperpolarization activated current are comodulated in a dose-dependent manner by the endogenous neuromodulator myomodulin to be capable to producing a wider range of periodic activity than modulation of either current alone. The range of functional burst periods is increased by 75% under comodulation compared to the modulation of Na^+/K^+ pump current alone, and nearly 90% compared to the modulation of h-current alone. Decreasing $I_{PumpMax}$ and increasing $\bar{g}_h$ in our model also allows the system to avoid asymmetric and seizure-like plateau containing regimes. Our experimental recordings from Leech HN HCOs confirm that this model of comodulation is able to reproduce the temporal characteristics of the rhythm seen in experiments. The matching experimental cases are located along the border of an asymmetric regime in the model, further away from the border with more dangerous seizure-like activity. This likely affords some level of protection from perturbations which could switch into the more dangerous regime. We described the comodulation mechanism with an inverse relation between the pump and h-currents and found that it comprises a general mechanism for the robust and flexible control of oscillatory neuronal networks.

The network structure with synaptic inhibition is a critical part of the mechanism. The same comodulation in the single cell model leads to seizure-like plateau-containing oscillations which could be harmful to the animal. Neuromodulation moves the single cell outside of its functional dynamical regime by lowering the pump current enough to cause a depolarization block during bursting. A half-center oscillator comprised of these single cells, however, maintains functional activity under modulated conditions. A lack of network inhibition is often cited as a cause of seizures and other dysfunctional neural activity. The electrogenic Na^+/K^+ pump provides a source of self-inhibition to bursting cells. During the depolarized spiking phase,

Na^+ enters the cell which activates the outward pump which contributes to burst termination. We also found that in this modulated parameter domain of the HCO model, two bursting patterns coexist which both meet the criteria of functional bursting activity of this circuit. Cycle period and burst duration of the patterns are very similar, but one of these regimes has twice the intra-burst spike frequency. This "high gear" mode of bursting would provide more synaptic input to motor neurons with the same pacing envelope as the lower spike frequency regime. By comparing these HCO regimes to single cell regimes under similar modulated conditions, we also demonstrate that modulation which decreases the maximal pump current can counterintuitively increase the average pump current throughout the bursting cycle. An incomplete block of the pump does not guarantee less pump current in this system.

In ICCs in the mammalian intestinal syncytium, intracellular Ca^{2+} oscillations play a major role in the generation of the electrical slow waves which pace intestinal motor patterns. The PMCA pump has an impact on these Ca^{2+} oscillations. Decreasing the activity of the PMCA pump can ultimately lead to extremely high levels of intracellular Ca^{2+}, which disrupts ionic gradients driving the intracellular calcium exchange, and results in a depolarization block. Disruptions to mitochondrial calcium signaling pathways can switch the cell between functional electrical slow wave production to silence. High levels of calcium can also be toxic to cells. We show that increased activity of the PMCA pump also can lead to dysfunctional silence, meaning its expression in these cells must be tightly regulated. The model predicts the influence of PMCA pump strength on the period of slow wave production and also the coexistence of silent (dysfunctional) and periodic activity regimes near the canonical set of parameters.

Biophysical modeling methods provide powerful tools for studying neurons and networks under modulated conditions. Many systems have many modulators and many membrane

currents, and their interactive effects are non-trivial. Utilizing single factor electrophysiological experiments is an important step in determining the physical properties which underlie modulatory processes, but to understand the major interactive effects, models allow an experimenter to develop hypotheses about these interactive effects at a significantly lower cost than direct experiments with expensive reagents and animals. Major findings can then be evaluated in the living systems in an iterative loop which drives better model development and produces better predictions about the behavior of neural circuits.

REFERENCES

Angstadt JD, Friesen WO (1991) Synchronized oscillatory activity in leech neurons induced by calcium channel blockers. Journal of Neurophysiology. 66(6): p. 1858-73.

Aoyama M, Yamada A, Wang J, Ohya S, Furuzono S, Goto T, Hotta S, Ito Y, Matsubara T, Shimokata K, Chen SRW, Imaizumi Y, Nakayama S (2004) Requirement of ryanodine receptors for pacemaker Ca2+ activity in ICC and HEK293 cells. Journal of Cell Science. 117:2813-2825.

Arganda S, Guantes R, de Polavieja GG (2007) Sodium pumps adapt spike bursting to stimulus statistics. Nature Neuroscience 10(11): 1467-1473.

Barnes CA, Suster MS, Shen J, McNaughton BL (1997) Multistability of cognitive maps in the hippocampus of old rats. Nature 388:272–275.

Barnett W, O'Brien G, Cymbalyuk G (2013) Bistability of silence and seizure-like bursting. J Neurosci Methods 220:179–189.

Barreto E, Cressman JR (2011) Ion concentration dynamics as a mechanism for neuronal bursting. J Biol Phys 37(3): 361-373.

Bertorello A, Aperia A (1990) Short-term regulation of Na(+),K(+)-ATPase activity by dopamine. Am J Hypertens 3(6 Pt 2): 51S-54S.

Bertorello AM, Hopfield JF, Aperia A, Greengard P (1990) Inhibition by dopamine of (Na(+)+K+)ATPase activity in neostriatal neurons through D1 and D2 dopamine receptor synergism. Nature 347(6291): 386-388.

Bielefeldt K, Conklin JL (1997) Intestinal motility during hypoxia and reoxygenation in vitro. Dig. Dis. Sci., 42, No. 5, 878–884

Blair PJ, Rhee PL, Sanders KM, and Ward SM (2014) The significance of interstitial cells in neurogastroenterology. J. Neurogastroenterol. Motil., 20, No. 3, 294–317

Brezina V, Horn CC, Weiss KR (2005) Modeling neuromuscular modulation in Aplysia. III. Interaction of central motor commands and peripheral modulatory state for optimal behavior. Journal of Neurophysiology 93(3): 1523–1556.

Brezina V, Orekhova IV, Weiss KR (2003) Neuromuscular modulation in Aplysia. I. Dynamic model. Journal of Neurophysiology 90(4): 2592–2612.

Brini M, Cali T, Ottolini D, and Carafoli E (2013) The plasma membrane calcium pump in health and disease. FEBS J., 280, No. 21, 5385–5397

Bruce JIE (2018) Metabolic regulation of the PMCA: Role in cell death and survival. Cell Calcium, 69, 28–36

Calabrese, RL (1998) Cellular, synaptic, network, and modulatory mechanisms involved in rhythm generation. Current Opinion in Neurobiology 8(6): 710-717.

Catarsi S, Brunelli M (1991) Serotonin depresses the after-hyperpolarization through the inhibition of the Na+/K+ electrogenic pump in T sensory neurones of the leech. The Journal of Experimental Biology 155: 261-273.

Cho WJ, Daniel EE (2005) Proteins of interstitial cells of Cajal and intestinal smooth muscle, colocalized with caveolin-1. Am. J. Physiol. Gastrointest. Liver Physiol., 288, No. 3, G571–585

Corrias A, Buist ML (2008) Quantitative cellular description of gastric slow wave activity. Am. J. Physiol. Gastrointest. Liver Physiol., 294, No. 4, G989– 995

Cymbalyuk GS, Gaudry Q, Masino MA, Calabrese RL (2002) Bursting in Leech Heart Interneurons: Cell-Autonomous and Network-Based Mechanisms. J Neurosci 22:10580–10592.

Cymbalyuk GS, Gaudry Q, Masino MA, Calabrese RL (2002) Bursting in Leech Heart Interneurons: Cell-Autonomous and Network-Based Mechanisms. J Neurosci 22:10580–10592.

Dashevskiy T, Cymbalyuk G (2018) Propensity for bistability of bursting and silence in the leech heart interneuron. Front Comput Neurosci 12: 5.

Der-Silaphet T, Malysz J, Hagel S, Arsenaulth AL, Huizinga JD (1998) Interstitial cells of Cajal direct normal propulsive contractile activity in the mouse small intestine. Gastroenterology. 114(4): 724-736.

Diamant NE, Bortoff A (1969) Nature of the intestinal slow-wave frequency gradient. Am. J. Physiol., 216, No. 2, 301–307

Doi A, Ramirez JM (2008) Neuromodulation and the orchestration of the respiratory rhythm. Respiratory Physiology & Neurobiology 164(1-2): 96-104.

Ellingson PJ, Korogod SM, Kahl TM, Kulagina IB, Makedonsky IA, Cymbalyuk GS (2019) Role of the Plasma Membrane Ca2+-ATPase Pump in the Regulation of Rhythm Generation by an Interstitial Cell of Cajal: A Computational Study. Neurophysiology **51**, 312-321.

Fall CP, Keizer JE (2001) Mitochondrial modulation of intracellular Ca(2+) signaling. J. Theor. Biol., 210, No. 2, 151–165

Faville RA, Pullan RJ, Sanders KM, and Smith NP (2008) A biophysically based mathematical model of unitary potential activity in interstitial cells of Cajal. Biophys. J., 95, No. 1, 88–104

Forrest MD (2014) The sodium-potassium pump is an information processing element in brain computation. Front Physiol 5.

Forrest MD, Wall MJ, Press DA, Feng J (2012) The sodium-potassium pump controls the intrinsic firing of the cerebellar Purkinje neuron. PLoS One 7.

Frohlich F, Bazhenov M, Timofeev I, Steriade M, Sejnowski TJ (2006) Slow state transitions of sustained neural oscillations by activity-dependent modulation of intrinsic excitability. J Neurosci 26(23): 6153-6162.

García PS, Wright TM, Cunningham IR, Calabrese RL (2008) Using a model to assess the role of the spatiotemporal pattern of inhibitory input and intrasegmental electrical coupling in the intersegmental and side-to-side coordination of motor neurons by the leech heartbeat central pattern generator. J Neurophysiol 100:1354–1371.

Goaillard J-M, Marder E (2021) Ion Channel Degeneracy, Variability, and Covariation in Neuron and Circuit Resilience. Annual Review of Neuroscience 44:null.

Goldman MS, Golowasch J, Marder E, Abbott LF (2001) Global Structure, Robustness, and Modulation of Neuronal Models. J Neurosci 21(14):5229–5238.

Golowasch J (2019) Neuronal Homeostasis: Voltage Brings It All Together. Current Biology 29:R641–R644.

Grashow R, Brookings T, Marder E (2009) Reliable neuromodulation from circuits with variable underlying structure. Proc Natl Acad Sci USA 106(28): 11742-11746.

Grashow R, Brookings T, Marder E (2010). Compensation for variable intrinsic neuronal excitability by circuit-synaptic interactions. J Neurosci 30(27): 9145-9156.

Gros R, Afroze T, You XM, Kabir G, Van Wert R, Kalair W, Hoque AE, Mungrue IN, Husain M (2003) Plasma membrane calcium ATPase overexpression in arterial smooth muscle increases vasomotor responsiveness and blood pressure. Circ. Res., 93, No. 7, 614–621

Guan Y, Worrell RT, Pritts TA, and Montrose MH (2009) Intestinal ischemia-reperfusion injury: reversible and irreversible damage imaged in vivo. Am. J. Physiol. Gastrointest. Liver Physiol., 297, No. 1, G187–196

Harris-Warrick RM (2011) Neuromodulation and flexibility in Central Pattern Generator networks. Curr Opin Neurobiol 21(5): 685-692.

Harris-Warrick RM, Johnson BR (2010) Checks and balances in neuromodulation. Frontiers in Behavioral Neuroscience 4.

Harris-Warrick RM, Johnson BR, Peck JH, Kloppenburg P, Ayali A, Skarbinski J (1998) Distributed Effects of Dopamine Modulation in the Crustacean Pyloric Networka. Annals of the New York Academy of Sciences 860:155–167.

Hatipoglu S, Akbulut S, Hatipoglu F, and R. Abdullayev (2014) Effect of laparoscopic abdominal surgery on splanchnic circulation: historical developments. World J. Gastroenterol., 20, No. 48, 18165–18176. Ca 321 2+-ATPase Pump in the Regulation of Spiking by Interstitial Cells of Cajal

Hazelwood LA, Free RB, Cabrera DM, Skinbjerg M, Sibley DR (2008) Reciprocal modulation of function between the D1 and D2 dopamine receptors and the Na+,K+-ATPase. J Biol Chem 283(52): 36441-36453.

Hennig GW, Hirst GD, Park KJ, Smith CB, Sanders KM, Ward SM, Smith TK (2004) Propagation of pacemaker activity in the guinea-pig antrum. J. Physiology. 556(Pt 2): 585-599.

Hill AA, Lu J, Masino MA, Olsen OH, Calabrese RL (2001) A model of a segmental oscillator in the leech heartbeat neuronal network. J Comput Neurosci 10:281–302.

Hirst GD, Edwards FR (2001) Generation of slow waves in the antral region of guinea-pig stomach – a stochastic process. J. Physiol., 535, Pt 1, 165–180

Hodgkin AL, Huxley AF (1952) A quantitative description of membrane current and its application to conduction and excitation in nerve. J Physiol 117:500–544.

Huizinga JD, Lammers WJ (2009) Gut peristalsis is governed by a multitude of cooperating mechanisms. Am. J. Physiol. Gastrointest. Liver Physiol., 296, No. 1, G1–8

Jasinski PE, Molkov YI, Shevtsova NA, Smith JC, Rybak IA (2013) Sodium and Calcium mechanisms of rhythmic bursting in excitatory neural networks of the pre-Botzinger complex: a computational modelling study. Eur J Neurosci 37(2): 212-230.

Khorkova O, Golowasch J (2007) Neuromodulators, Not Activity, Control Coordinated Expression of Ionic Currents. Journal of Neuroscience 27:8709–8718.

Kito Y, Suzuki H (2003) Properties of pacemaker potentials recorded from myenteric interstitial cells of Cajal distributed in the mouse small intestine. J. Physiology. 552:803-818.

Korogod SM, Cymbalyuk GS, Makedonsky IA, and Kulagina IB (2018) Hypoxic depression of pacemaker activity of interstitial cells of Cajal: A threat of gastrointestinal dysmotility and necrosis. A simulation study. Neurophysiology, 50, No. 2, 76–82

Krishnan GP, Bazhenov M (2011) Ionic dynamics mediate spontaneous termination of seizures and postictal depression state. J Neurosci 31(24): 8870-8882.

Krishnan GP, Filatov G, Shilnikov A, Bazhenov M (2015) Electrogenic properties of the Na+/K+ ATPase control transitions between normal and pathological brain states. J Neurophysiol 113:3356–3374.

Krishnan GP, Filatov G, Shilnikov A, Bazhenov M (2015) Electrogenic properties of the Na+/K+ ATPase control transitions between normal and pathological brain states. Journal of Neurophysiology 113:3356–3374.

Kueh D, Barnett WH, Cymbalyuk GS, Calabrese RL (2016) Na+/K+ pump interacts with the h-current to control bursting activity in central pattern generator neurons of leeches. eLife 5:e19322.

Lees-Green R, Du P, O'Grady G, Beyder A, Farrugia G, Pullan A (2011) Biophysically based modeling of the interstitial cells of Cajal: current status and future perspectives. Front. Physiol., 2, No. 29

Lees-Green R, Gibbons SJ, Farrugia G, Sneyd J, Cheng LK (2014) Computational modeling of anoctamin 1 calcium activated chloride channels as pacemaker channels in interstitial cells of Cajal. Am. J. Physiol. Gastrointest. Liver Physiol., 306, No. 8, G711–727

Li YX, Bertram R, Rinzel J (1996) Modeling N-methyl-D-aspartate-induced bursting in dopamine neurons. Neuroscience 71(2): 397-410.

Magnus G, Keizer J (1997) Minimal model of beta-cell mitochondrial Ca2+ handling. Am. J. Physiol., 273, No. 2, Pt. 1, C717–733

Malashchenko T, Shilnikov A, Cymbalyuk G (2011) Six Types of Multistability in a Neuronal Model Based on Slow Calcium Current. PLOS ONE 6:e21782.

Malysz J, Gibbons S, Saravanaperumal S, Du P, Eisenman S, Cao C, Oh U, Saur D, Klein S, Ordog T, Farrugia G (2017) Conditional genetic deletion of Ano1 in interstitial cells of

Cajal impairs Ca2+ transients and slow waves in adult mouse small intestine. American Journal of Physiology-Gastrointestinal and Liver Physiology. 312(3):G228-G245.

Marder E (2011) Variability, compensation, and modulation in neurons and circuits. PNAS 108:15542–15548.

Marder E (2012) Neuromodulation of Neuronal Circuits: Back to the Future. Neuron 76(1): 1-11.

Marder E, Calabrese RL (1996). Principles of rhythmic motor pattern generation. Physiol Rev 76(3): 687-717.

Marder E, Goeritz ML, Otopalik AG (2015) Robust circuit rhythms in small circuits arise from variable circuit components and mechanisms. Curr Opin Neurobiol 31: 156-163.

Marder E, O'Leary T, Shruti S (2014) Neuromodulation of Circuits with Variable Parameters: Single Neurons and Small Circuits Reveal Principles of State-Dependent and Robust Neuromodulation. Ann Rev Neurosci 37:329–346.

Marin B, Barnett WH, Doloc-Mihu A, Calabrese RL, Cymbalyuk GS (2013) High Prevalence of Multistability of Rest States and Bursting in a Database of a Model Neuron. PLoS Comput Biol 9:e1002930.

Nadim F, Olsen OH, De Schutter E, Calabrese RL (1995) Modeling the leech heartbeat elemental oscillator. I. Interactions of intrinsic and synaptic currents. J Comput Neurosci 2:215–235.

Newman JP, Butera RJ (2010) Mechanism, dynamics, and biological existence of multistability in a large class of bursting neurons. Chaos 20:023118.

O'Leary T, Williams AH, Caplan JS, Marder E (2013) Correlations in ion channel expression emerge from homeostatic tuning rules. PNAS 110:E2645–E2654.

Oliveira VH, Nascimento KS, Freire MM, Moreira OC, Scofano HM, Barrabin H, Mignaco JA (2008) Mechanism of modulation of the plasma membrane Ca(2+)-ATPase by arachidonic acid. Prostaglandins Other Lipid Mediat., 87, Nos. 1–4, 47–53

Olypher A, Cymbalyuk G, Calabrese RL (2006) Hybrid systems analysis of the control of burst duration by low-voltage-activated calcium current in leech heart interneurons. J Neurophysiol 96:2857–2867.

Opdyke CA, Calabrese RL (1994) A persistent sodium current contributes to oscillatory activity in heart interneurons of the medicinal leech. J Comp Physiol A 175: 781-789.

Parker JR, Bondy B, Prilutsky BI, Cymbalyuk GS (2018) Control of Transitions between Locomotor-like and Paw-Shake-like Rhythms in a Model of a Multistable Central Pattern Generator. J Neurophysiol 120(3):1074-1089.

Picton LD, Zhang H, Sillar KT (2017) Sodium pump regulation of locomotor control circuits. J Neurophysiol 118(2): 1070-1081.

Pignataro MF, Dodes-Traian MM, Gonzalez-Flecha FL, Sica M, Mangialavori IC, Rossi JP (2015) Modulation of plasma membrane Ca2+- ATPase by neutral phospholipids: effect of the micelle-vesicle transition and the bilayer thickness. J. Biol. Chem., 290, No. 10, 6179–6190

Sammour T, Mittal A, Loveday BP, Kahokehr A, Phillips AR, Windsor JA, Hill AG (2009) Systematic review of oxidative stress associated with pneumoperitoneum. Br. J. Surg., 96, No. 8, 836–850

Sanders KM, Koh SD, Ward SM (2006) Interstitial cells of Cajal as pacemakers in the gastrointestinal tract. Annual Review of Physiology. 68: 307-343.

Sanders KM, Ward SM, and Koh SD (2014) Interstitial cells: regulators of smooth muscle function. Physiol. Rev., 94, No. 3, 859–907

Scuri R, Lombardo P, Cataldo E, Ristori C, Brunelli M (2007) Inhibition of Na+/K+ ATPase potentiates synaptic transmission in tactile sensory neurons of the leech. Eur J Neurosci 25(1): 159-167.

Seamans JK, Gorelova N, Durstewitz D, Yang CR (2001) Bidirectional dopamine modulation of GABAergic inhibition in prefrontal cortical pyramidal neurons. J Neurosci 21: 3628-3638.

Sharples SA, Whelan PJ (2017) Modulation of Rhythmic Activity in Mammalian Spinal Networks Is Dependent on Excitability State. eNeuro 4(1).

Shimojima N, Nakaki T, Morikawa Y, Hoshino K, Ozaki H, Hori M, Kitajima M (2006) Interstitial cells of Cajal in dysmotility in intestinal ischemia and reperfusion injury in rats J. Surg. Res., 135, No. 2, 255–261

Sorensen M, DeWeerth S, Cymbalyuk G, Calabrese RL (2004) Using a Hybrid Neural System to Reveal Regulation of Neuronal Network Activity by an Intrinsic Current. J Neurosci 24:5427–5438.

Spitzer N, Cymbalyuk G, Zhang H, Edwards DH, Baro DJ (2008) Serotonin Transduction Cascades Mediate Variable Changes in Pyloric Network Cycle Frequency in Response to the Same Modulatory Challenge. Journal of Neurophysiology 99:2844–2863.

Strehler EE (2013) Plasma membrane calcium ATPases as novel candidates for therapeutic agent development. J. Pharm. Pharm. Sci., 16, No. 2, 190–206

Strehler EE, Treiman M (2004) Calcium pumps of plasma membrane and cell interior. Curr. Mol. Med., 4, No. 3, 323–335

Tang LS, Taylor AL, Rinberg A, Marder E (2012) Robustness of a rhythmic circuit to short- and long-term temperature changes. J Neurosci 32(29): 10075-10085.

Teshiba T, Shamsian A, Yashar B, Yeh S-R, Edwards DH, Krasne FB (2001) Dual and Opposing Modulatory Effects of Serotonin on Crayfish Lateral Giant Escape Command Neurons. J Neurosci 21:4523–4529.

Tobin A-E, Calabrese RL (2005) Myomodulin Increases Ih and Inhibits the Na/K Pump to Modulate Bursting in Leech Heart Interneurons. J Neurophysiol 94:3938–3950.

Torihashi S, Fujimoto T, Trost C, Nakayama S (2002) Calcium oscillation linked to pacemaking of interstitial cells of Cajal: requirement of calcium influx and localization of TRP4 in caveolae. J. Biol. Chem., 277, No. 21, 19191–19197

van Helden DF, Laver DR, Holdsworth J, and Imtiaz MS (2010) Generation and propagation of gastric slow waves. Clin. Exp. Pharmacol. Physiol., 37, No. 4, 516–524

Ward SM, Baker S, Faoite A, Sanders KM (2003) Propagation of slow waves requires IP3 receptors and mitochondrial Ca2+ uptake in canine colonic muscles. J. Physiology. 549(1): 207-218.

Ward SM, Ordog T, Koh SD, Abu Baker S, Jun JY, Amberg G, Monaghan K, Sanders KM (2000) Pacemaking in interstitial cells of Cajal depends upon calcium handling by endoplasmic reticulum and mitochondria. J. Physiol., 525, Pt. 2, 355–361

Weaver AL, Roffman RC, Norris BJ, Calabrese RL (2010) A Role for Compromise: Synaptic Inhibition and Electrical Coupling Interact to Control Phasing in the Leech Heartbeat CPG. Front Behav Neurosci 4

Wenning A, Norris BJ, Günay C, Kueh D, Calabrese RL (2018) Output variability across animals and levels in a motor system Ramirez J-M, ed. eLife 7:e31123.

Yilmaz S, Polat C, Kahraman A, Koken T, Arikan Y, Dilek ON, Gökçe O (2004) The comparison of the oxidative stress effects of different gases and intra-abdominal pressures in an experimental rat model. J Laparoendosc. Adv. Surg. Tech. A, 14, No. 3, 165–168

Youm JB, Kim N, Han J, Kim E, Joo H, Leem CH, Goto G, Noma A, Earm YE (2006) A mathematical model of pacemaker activity recorded from mouse small intestine. Philos. Trans. A Math Phys. Eng. Sci., 364, No. 1842, 1135–1154

Yu N, Morris CE, Joos B, Longtin A (2012) Spontaneous excitation patterns computed for axons with injury-like impairments of sodium channels and Na/K pumps. PLoS Comput Biol 8(9): e1002664.

Zhang HY, Picton L, Li WC, Sillar KT (2015) Mechanisms underlying the activity-dependent regulation of locomotor network performance by the Na+ pump. Sci Rep 5: 16188.

Zhang HY, Sillar KT (2012) Short-term memory of motor network performance via activity-dependent potentiation of Na+/K+ pump function. Curr Biol 22(6): 526-531.

Zhang LN, Li JX, Hao L, Sun YJ, Xie YH, Wu SM, Liu L, Chen XL, Gao ZB (2013) Crosstalk between dopamine receptors and the Na(+)/K(+)-ATPase (review). Mol Med Rep 8(5): 1291-1299.

Zhang LN, Su SW, Guo F, Guo HC, Shi XL, Li WY, Liu X, Wang YL (2012) Serotonin-mediated modulation of Na+/K+ pump current in rat hippocampal CA1 pyramidal neurons. BMC Neurosci 13: 10.

Zhang Y, Bucher D, Nadim F (2017) Ionic mechanisms underlying history-dependence of conduction delay in an unmyelinated axon. eLife 6:e25382

Zhu MH, Sung TS, Kurahashi M, O'Kane LE, O'Driscoll K, Koh SD, Sanders KM (2016) Na+-K+-Cl- cotransporter (NKCC) maintains the chloride gradient to sustain pacemaker activity in interstitial cells of Cajal. American Journal of Physiology-Gastrointestinal and Liver Physiology. 311(6):G1037-G1046